

Subaru Weak Lensing survey – II: Multi-object Spectroscopy and Cluster Masses

Takashi HAMANA¹, Satoshi MIYAZAKI¹, Nobunari KASHIKAWA¹, Richard S. Ellis², Richard J. Massey³,
Alexandre Refregier⁴, James E. Taylor⁵

¹*National Astronomical Observatory of Japan, Mitaka, Tokyo 181-8588, Japan*

²*California Institute of Technology, 105-24 Astronomy, Pasadena CA 91125, USA*

³*Institute for Astronomy, Royal Observatory, Blackford Hill, Edinburgh EH9 3HJ, UK*

⁴*Service d'Astrophysique CEA Saclay, Bat. 709 F-91191 Gif sur Yvette, France*

⁵*University of Waterloo, Department of Physics & Astronomy, Waterloo, Ontario N2L 3G1, Canada*

(Received 2008 August 28; accepted 2001 January 1)

Abstract

We present the first results of a multi-object spectroscopic (MOS) campaign to follow up cluster candidates located via weak lensing. Our main goals are to search for spatial concentrations of galaxies that are plausible optical counterparts of the weak lensing signals, and to determine the cluster redshifts from those of member galaxies. Around each of 36 targeted cluster candidates, we obtain 15–32 galaxy redshifts. For 28 of these targets, we confirm a secure cluster identification, with more than five spectroscopic galaxies within a velocity of ± 3000 km/s. This includes three cases where two clusters at different redshifts are projected along the same line-of-sight. In 6 of the 8 unconfirmed targets, we find multiple small galaxy concentrations at different redshifts, each containing at least three spectroscopic galaxies. The weak lensing signal around those systems is thus probably created by the projection of groups or small clusters along the same line-of-sight. In both the remaining two targets, a single small galaxy concentration is found.

We evaluate the weak lensing mass of confirmed clusters via two methods: aperture densitometry and by fitting to an NFW model. In most cases, these two mass estimates agree well. In some candidate super-cluster systems, we find additional evidence of filaments connecting the main density peak to additional nearby structure. For a subsample of our most cleanly measured clusters, we investigate the statistical relation between their weak lensing mass ($M_{\text{NFW}}, \sigma_{\text{sis}}$) and the velocity dispersion of their member galaxies (σ_v), comparing our sample with optically and X-ray selected samples from the literature. Our lensing-selected clusters are consistent with $\sigma_v = \sigma_{\text{sis}}$, with a similar scatter to the optically and X-ray selected clusters. We thus find no evidence of selection bias compared to these other techniques. We also derive an empirical relation between the cluster mass and the galaxy velocity dispersion, $M_{200} = 9.6 \times 10^{14} \times (\sigma_v/1000 \text{ km/s})^{2.7} / E(z) h^{-1} M_{\odot}$, which is in reasonable agreement with the prediction of N -body simulations in the Λ CDM cosmology.

Key words: galaxies: clusters — cosmology: observations — dark matter — large-scale structure of universe

1. Introduction

The development of weak lensing techniques, coupled with deep panoramic imaging surveys, has enabled us to locate clusters of galaxies via the gravitational distortion of background galaxies' shapes. Since the first, spectroscopically confirmed discovery of a shear-selected cluster by Wittman et al. (2001), there has been rapid progress toward a large, weak-lensing selected cluster catalogue. Miyazaki et al. (2003) first reported the detection of several significant shear-selected cluster candidates in an untargeted 2.1 deg^2 field. Hettterscheidt et al. (2005) found 5 cluster candidates in 50 randomly selected VLT FORS1 fields (0.64 deg^2 in total), all of which are associated with an overdensity of galaxies. Wittman et al. (2006) reported 8 candidates in the 8.6 deg^2 Deep Lens Survey. Gavazzi & Soucail (2007) found 14 cluster candidates in the 4 deg^2 CFHT Legacy Survey (Deep), of which nine have optical

or X-ray counterparts and are thus secure clusters.

The first sizable sample of weak lensing shear-selected cluster candidates was presented by Miyazaki et al. (2007; hereafter P1). Their sample was obtained solely via peak finding in weak lensing density maps, and includes 100 significant peaks in a 16.7 deg^2 survey area.

Before such a sample is used for statistical cosmological or astronomical analyses, two additional follow-up observations are required. Firstly, each cluster candidate should be confirmed by independent observations, since a fraction of lensing peaks could be false positives from e.g. the chance tangential alignment of galaxies' intrinsic ellipticities (White, van Waerbeke & Mackey 2002; Hamana, Takada & Yoshida, 2004; Hennawi & Spergel 2005). Secondly, the redshifts of confirmed clusters need to be determined in order to derive their physical quantities, including mass.

We have conducted a multi-object spectroscopic (MOS)

campaign that accomplishes both goals. We have measured the redshifts of a few tens of galaxies within an expected cluster scale radius (or core radius, typically a few arcmins), and searched for spatial concentrations that are plausible optical counterparts of the weak lensing signals. Once a galaxy overdensity is found, it is easy to determine the cluster redshift from the redshifts of member galaxies. It is important to note that cluster confirmation based on prominent galaxy concentrations would not be very effective for very high mass-to-light ratio (M/L), galaxy-poor systems. Although our methodology can *confirm* normal or galaxy-rich clusters, the absence of a galaxy concentration in our fairly sparsely-sampled data therefore does not necessarily prove that a weak lensing signal is false.

In addition to our primary goals, multi-object spectroscopic observations provide several useful by-products. If redshifts can be obtained for sufficient galaxies in a cluster, their line-of-sight velocity dispersion provides an estimate of the cluster’s dynamical mass. MOS observations can also detect multiple structures along the same line of sight. Because of the relatively broad redshift window function of gravitational lensing, physically unrelated structures in the same line of sight may contribute to a single peak in a weak lensing density map, resulting in an overestimation of the cluster mass (White et al. 2002). It will therefore be important to quantify and properly account for such projections when computing statistics of cluster masses from weak lensing observations.

In this paper, we present results of cluster confirmations and cluster redshifts. We discuss the detailed weak lensing properties of each system and, for a clean subset of our clusters, examine statistical relations between the weak lensing masses and dynamical masses. A statistical analysis of the *entire* sample, taking into account additional selection effects, will be presented in Green et al. (in preparation).

This paper is organized as follows. In §2, we discuss our selection of cluster candidates. In §3, we describe our new observations, data reduction and measurements of galaxy redshifts. In §4, we identify optical counterparts to cluster candidates, and measure their velocity dispersions and dynamical masses. In §5, we analyze the weak lensing signal of confirmed clusters. In §6, we investigate cluster scaling relations within our sample. In §7, we summarize our results. In Appendix 1, we calculate the gravitational lensing shear profile of a truncated NFW model. Detailed discussions of each system, including comparisons of the dynamic and lensing masses, follow in Appendices 2 (for clusters we have observed) and 3 (for observations taken from the literature).

Throughout this paper, we adopt a flat Λ CDM cosmology with the matter density $\Omega_m = 0.3$, the cosmological constant $\Omega_\Lambda = 0.7$, the Hubble constant $H_0 = 100h$ km s⁻¹ Mpc⁻¹ with $h = 0.7$.

2. Cluster candidates

Targets for our spectroscopic follow-up campaign were selected from amongst the Subaru weak lensing survey’s

shear-selected cluster candidates. We refer the reader to P1 for details of the Subaru weak lensing survey, including the image acquisition and analysis, the creation of weak lensing density maps, and the selection of cluster candidates. Briefly, R_C -band imaging data were obtained in thirteen fields (except for the COSMOS field where i' -band data was used). Each survey area is 1.07 – 2.8 degree² and the total area is 21.82 degree². Weak lensing density maps were computed with a pixel size of 15×15 arcsec, using the Kaiser & Squires (1993) inversion algorithm, with a Gaussian smoothing filter of $\theta_G = 1$ arcmin. Noise maps were also created using the same algorithm, but from the root-mean-square (RMS) of 100 realizations in which the orientations of the measured shears were randomized. Maps of the signal-to-noise ratio (S/N) were created by dividing the density map by the noise RMS map. Positive peaks were searched for in the S/N maps, and peaks with S/N greater than a threshold value were defined as candidates of massive halos. P1 took a threshold value of $S/N = 3.69$. After carefully avoiding areas close to bright stars or field boundaries, where the weak lensing density map could be affected by a lack of background lensed galaxies, 100 significant detections remained in a 16.7 deg² area (see Table 2 of P1 for their weak lensing and optical properties).

We have carried out multi-object spectroscopic follow-up observations of 36 cluster candidates (see Table 1 for our targets’ optical and weak lensing properties, galaxy number densities, peak κ values, and the amplitudes of their radial shear profiles, γ_{sis} , which is defined in §5.4.2). Our target selection differs slightly from that of P1 because, in the planning stages of this follow-up program, we were still evaluating the optimal criteria for reliable cluster selection. The current selection was based on both the peak κ values and a visual inspection of the optical images. The peak κ value was evaluated with two filter scales (1 and 2 arcmin). Since the Gaussian filter acts as a matched filter, large nearby systems can be detected with a higher S/N in the 2’ filter. Due to the visual inspection, our target could be biased toward optically rich clusters. Of our 36 targets, 24 are listed in the P1 catalog. The remaining 12 targets are either below the P1 S/N threshold with a single filter scale, or in discarded survey areas (close to bright stars or field boundaries).

3. Spectroscopic observations and data reduction

3.1. Spectroscopic observations

We used the Subaru telescope’s Faint Object Camera and Spectrograph (FOCAS; Kashikawa et al. 2002) in Multi-Object Spectroscopy (MOS) mode. Each cluster candidate was observed with one 6’ diameter slit mask, on which we placed 25 – 38 slits. We used the 150/mm grating and the SY47 order sorting filter, resulting in a wavelength coverage between 4700 and 9400Å, with a pixel resolution of 2.8Å pixel⁻¹. The slit width was 0.8 arcsec for all cases, which corresponds to a spectral resolution power of $R \sim 250$, or $\Delta\lambda \sim 30\text{Å}$ at 8000Å.

We conducted FOCAS Observations in 2004 May

Table 1. Summary of spectroscopic observations. (a) Cluster name in the IAU convention. (b) Field and catalogue number given in P1 (if listed). (c) The peak κ value. (d) The number density of galaxies with $18 < mag < 23$ (Vega mag) within 1 arcmin of the κ peak, and the mean value over the same Suprime-Cam FOV in parentheses. Here the luminosity is defined by the *SExtractor* MAG_AUTO in the R_C -band, except for the COSMOS field where i' -band data is used. (e) Exposure time. (f) The date of the observation. (g) The number of galaxies for which a spectroscopic redshift was obtained. (h) The number of clusters identified (see §4 for our cluster identification criteria) and, when no clusters were identified, the number of small galaxy concentrations in parentheses.

Name ^(a)	Field-No. ^(b)	κ_{peak} ^(c)	n_g ^(d) [arcmin ⁻²]	t_{exp} ^(e) [sec]	obs date ^(f)	N_{spec} ^(g)	N_c ^(h)
SL J0217.3–0524	SXDS	0.041	12(7.2)	$2 \times 1200 + 900$	2005/12/23	24	1
SL J0217.6–0530	SXDS	0.041	11(7.2)	3×900	2005/12/23	19	0(1)
SL J0217.9–0452	SXDS	0.061	12(6.2)	$2 \times 1200 + 900$	2005/12/9	21	0(1)
SL J0218.0–0444	SXDS	0.047	13(6.6)	3×1200	2005/12/9	19	0(2)
SL J0219.6–0453	SXDS	0.060	12(6.9)	$2 \times 1200 + 900$	2005/12/23	25	1
SL J0222.8–0416	XMM-LSS-23	0.060	12(6.7)	$2 \times 1500 + 1200$	2005/12/24	27	1
SL J0224.4–0449	XMM-LSS-02	0.065	14(6.0)	$2 \times 1200 + 900$	2005/12/23	25	1
SL J0224.5–0414	XMM-LSS-12	0.047	15(6.7)	3×900	2004/12/9	25	1
SL J0225.3–0441	XMM-LSS-15	0.086	7.1(6.0)	3×1200	2005/12/24	26	1
SL J0225.4–0414	XMM-LSS-22	0.083	14(6.9)	3×1200	2004/12/9	20	1
SL J0225.7–0312	XMM-LSS-01	0.114	8.1(7.1)	3×1200	2005/12/24	25	1
SL J0228.1–0450	XMM-LSS-16	0.082	13(6.1)	3×1200	2005/12/24	25	1
SL J0850.5+4512	Lynx-08	0.099	11(6.2)	3×900	2005/12/17	26	1
SL J1000.7+0137	COSMOS-00	0.092	14(7.0)	3×900	2004/12/9	32	1
SL J1001.2+0135	COSMOS	0.081	13(8.8)	2×900	2004/12/9	32	2
SL J1002.9+0131	COSMOS	0.047	18(8.8)	2×1800	2004/5/16	21	0(2)
SL J1047.3+5700	Lockman Hole-05	0.101	18(6.9)	3×1200	2005/12/23	27	2
SL J1048.1+5730	Lockman Hole-15	0.077	10(7.8)	3×1200	2005/12/23	27	1
SL J1049.4+5655	Lockman Hole-06	0.087	14(6.9)	3×1200	2005/12/23	26	1
SL J1051.5+5646	Lockman Hole-03	0.082	8.4(8.6)	$2 \times 1200 + 600$	2005/6/2	15	0(2)
SL J1052.0+5659	Lockman Hole	0.085	7.1(8.6)	2×1200	2005/6/2	24	0(2)
SL J1052.5+5731	Lockman Hole	0.075	11(8.6)	$2 \times 1200 + 600$	2005/6/2	17	0(2)
SL J1057.5+5759	Lockman Hole-00	0.091	23(6.3)	3×1200	2004/12/9	32	1
SL J1135.6+3009	GD140-00	0.117	10(6.7)	2×900	2004/12/17	17	1
SL J1201.7–0331	PG1159-035-05	0.070	16(6.6)	2×1800	2004/5/16	18	1
SL J1204.4–0351	PG1159-035	0.079	14(6.4)	3×900	2004/12/17	20	1
SL J1334.3+3728	13hr field-00	0.097	24(7.1)	$2 \times 1800 + 420$	2004/5/16	31	1
SL J1335.7+3731	13hr field-01	0.074	16(7.1)	3×900	2005/6/1	23	1
SL J1337.7+3800	13hr field-04	0.082	14(7.3)	3×1200	2005/6/1	27	1
SL J1601.6+4245	GTO 2deg ²	0.107	14(6.2)	3×1200	2005/7/31	29	2
SL J1602.8+4335	GTO 2deg ² -00	0.099	22(7.0)	3×900	2005/6/1	22	1
SL J1605.4+4244	GTO 2deg ² -09	0.067	11(7.8)	3×1200	2005/7/31	20	1
SL J1607.9+4338	GTO 2deg ²	0.079	11(6.5)	3×1200	2005/8/1	21	1
SL J1634.1+5639	CM DRA-06	0.104	5.1(6.3)	3×900	2005/6/1	16	1
SL J1639.9+5708	CM DRA-04	0.044	12(7.3)	3×1200	2005/8/1	24	0(2)
SL J1647.7+3455	DEEP16-00	0.070	9.7(5.0)	3×1200	2004/12/9	32	1

16, December 9, 17, 2005 June 1-2, July 31-August 1, December 9 and 23-24. Observing conditions were not always good: some targets were observed under a cloudy/cirrus sky. We took two or three exposures per mask. The total exposure times are listed in Table 1 and are 30–70 minutes depending on the apparent magnitude of targeted galaxies and the observing conditions.

Within each field, target galaxies were selected by their apparent R_C magnitude (with higher priorities for brighter galaxies) and color information when it was available. To obtain multicolor imaging, we searched the Subaru archive or took pre-imaging data for the MOS mask design with the I_C -band filter. When color information was available, we gave a higher priority to galaxies of a color consistent with any early type red-sequences evident in the color-magnitude diagram. To avoid possible selection effects, we set the color range for this increased priority relatively broad (± 0.5 mag in color from a possible red-sequence). Finally, we visually inspected the selected galaxies to avoid obviously nearby galaxies.

3.2. Data reduction

The data were reduced with the standard FOCAS data reduction package *FOCASRED*¹, which operates in IDL and IRAF. After bias subtraction and flat-fielding, each slit-let spectrum was extracted, then wavelength- and flux-calibrated. Night sky lines within the spectra themselves were used to define the wavelength scale. We then carried out skysubtraction using a 2nd order Chebyshev function. Individual spectra of 420–1800 sec exposure time were combined using the *imcombine* IRAF task. The final wavelength determination accuracy was a few angstroms.

3.3. Redshift measurement

Redshifts were determined by centroiding multiple emission and/or absorption lines. The statistical error of the redshift measurement is less than 2×10^{-4} . In our samples, there are 18 galaxies whose redshifts were also obtained by SDSS. The differences between SDSS and our measurements are less than 4×10^{-3} . Thus we conclude that any systematic errors in our redshift measurement are very small.

We adopted a simple spectral classification of galaxies, following Cohen et al. (1999), and refer the reader to their paper for details. Briefly, “E” (emission) denotes a galaxy in which emission lines dominate the spectrum; “A” (absorption) denotes a galaxy where no emission lines are detected; and “C” (composite) is an intermediate case where both emission and absorption (usually [OII] $\lambda 3727$ and H + K) are seen. Note that the [OII] $\lambda 3727$ emission line is blueward of our wavelength coverage for galaxies at $z \lesssim 0.2$, so the discrimination between C and A was somewhat ambiguous for such nearby galaxies.

We successfully obtained the redshifts of 15–32 galaxies near each cluster candidate. All the results² (the spatial

and redshift distributions) are presented in Figures 8–43.

4. Dynamical masses

We next searched for galaxy concentrations in the redshift data. With only information on the line-of-sight velocity and the sky coordinates of relatively sparse samples, it was often difficult to judge whether galaxies that appear clustered were really gravitationally bound. We adopted a quantitative criterion for galaxy cluster identification that there be *more than five galaxies within ± 3000 km/s*. As shown in Table 2, 31 galaxy concentrations satisfied this condition. Three cluster candidates (SL J1001.2+0135, SL J1047.3+5700 and SL J1601.6+4245) contained two galaxy concentrations. The velocity distribution of galaxies within or near each concentration are presented in Figure 1. Note that there may be additional galaxy clusters that remain unconfirmed by our MOS observation because of our relatively sparse sampling.

We then computed the velocity dispersion of galaxies within the 31 detected clusters. To do this, we used the *ROSTAT* routine, an implementation of the robust bi-weight algorithm by Beers, Flynn & Gebhardt (1990). We recorded the bi-weight estimators for the cluster redshift (z_c) and velocity dispersion (σ_v), computing their errors by a bootstrap technique. The results are summarized in Table 2.

The virial mass of a well relaxed cluster can be estimated from its measured velocity dispersion (see, e.g., Cohen & Kneib 2002) via

$$M_{dyn} = \frac{6\sigma_v^2 R_h}{G}, \quad (1)$$

where R_h is the harmonic radius, related to the virial radius by $r_{vir} = \pi R_h / 2$ (Limber & Mathews 1960), but computed from angular positions of the member galaxies (see e.g., Saslow 1985; Nolthenius & White 1987),

$$R_h = D_A(z_c) \frac{\pi N_m(N_m - 1)}{2} (\sum_i \sum_{j>i} \theta_{ij}^{-1})^{-1}, \quad (2)$$

where θ_{ij} is the angular distance between galaxies i and j , N_m is the number of cluster members, and D_A is the angular diameter distance. We estimated the error on R_h by a bootstrap technique.

The values of M_{dyn} and R_h that we measured for the 31 clusters are summarized in Table 2. Note that in deriving eq. (2), it was assumed that member galaxies are homogeneously sampled. In our case, the selection of target galaxies was restricted by the constraints of MOS mask design. Accordingly, our sampling fraction (the ratio of targeted to member galaxies) could be smaller in the densely populated cores of clusters than in their outer parts. It is thus possible that our estimates of R_h were slightly overestimated. We did not have enough information to propagate the potential systematic bias caused by this inhomogeneous sampling. Therefore, our estimates of dynamical masses should be regarded with some caution.

¹ The Subaru data reduction manual is available from <http://www.naoj.org/Observing/DataReduction/>

² Machine-readable tables are available from

<http://th.nao.ac.jp/~hamanatk/SLmosz.dat>

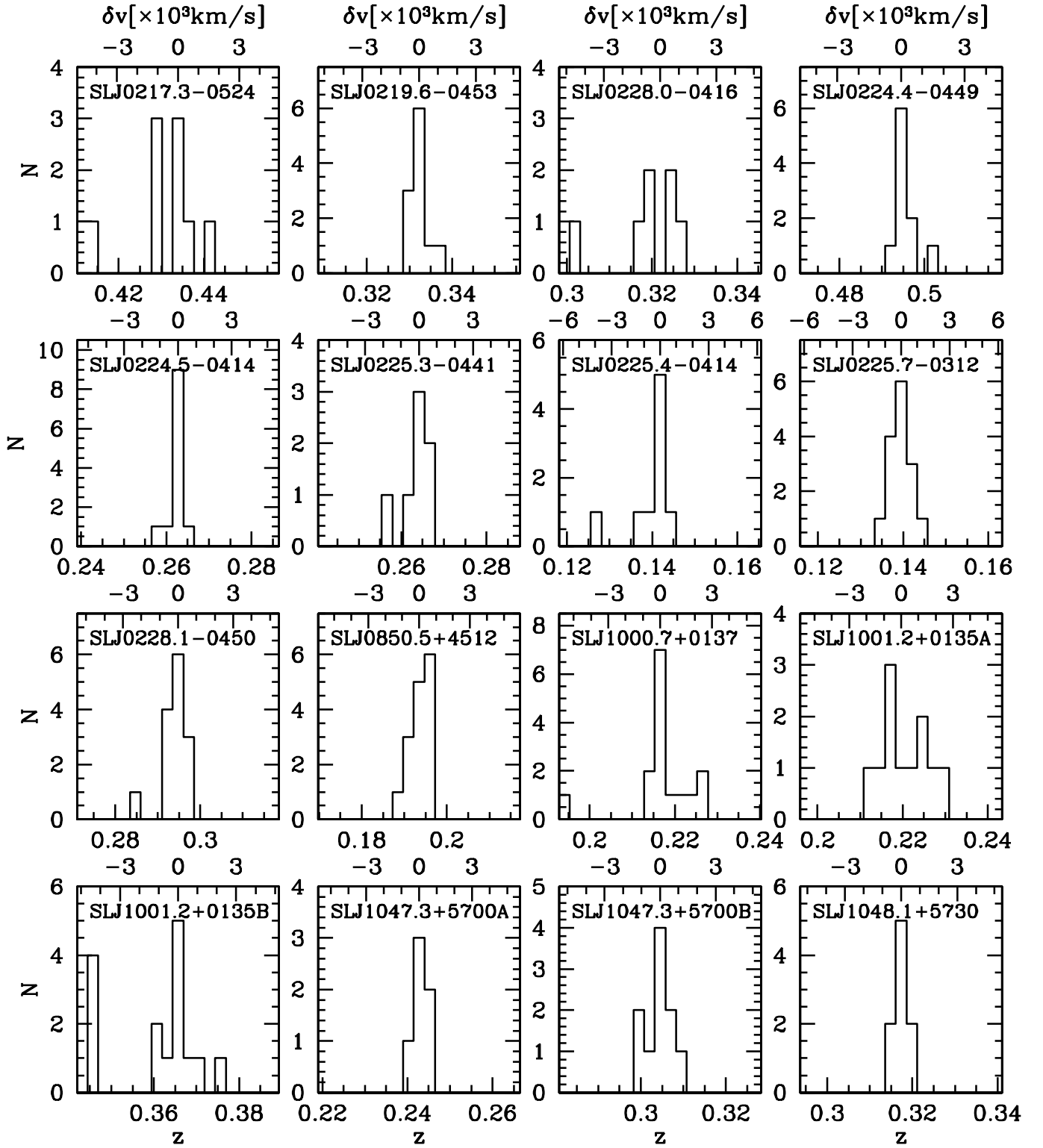


Fig. 1. The distribution of spectroscopically confirmed member galaxies (located within ± 3000 km/s), in redshift (lower scale) and velocity (upper scale) space.

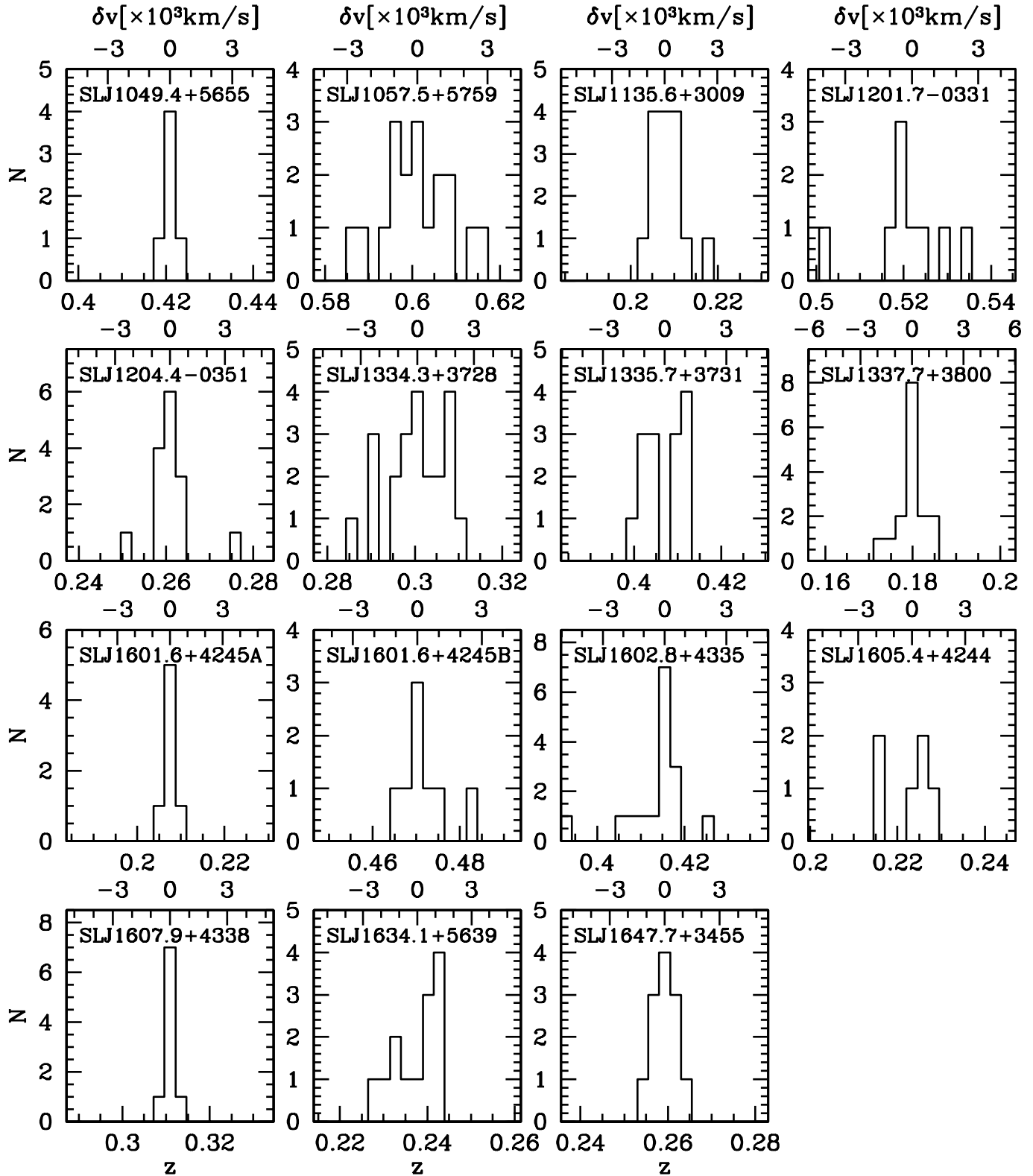


Fig. 1. Continued from previous page.

Table 2. Summary of dynamical analysis of galaxy groups/clusters. (a) Number of spectroscopic galaxies within a velocity space of ± 3000 km/s. (b) The cluster redshift. (c) The velocity dispersion. (d) The angular harmonic radius. (e) The harmonic radius estimated by eq (2). (f) The dynamical mass estimated by eq (1). (g) Note: PS indicates poor statistics in the estimation of velocity dispersion ($N < 12$), NS the existence of a neighbor system, FB proximity (< 3 arcmin) to the Suprime-Cam field boundary, and CS membership of the clean sample (see §6).

Name	$N^{(a)}$	$z_c^{(b)}$	$\sigma_v^{(c)}$ [km/s]	$\theta_h^{(d)}$ [arcmin]	$R_h^{(e)}$ [h^{-1} Mpc]	$M_{dyn}^{(f)}$ [$\times 10^{14} h^{-1} M_\odot$]	Note ^(g)
SL J0217.3–0524	8	$0.4339^{+0.0010}_{-0.0041}$	958^{+350}_{-224}	2.06 ± 0.78	0.487 ± 0.217	$6.25^{+5.89}_{-3.51}$	PS
SL J0219.6–0453	11	$0.3322^{+0.0008}_{-0.0005}$	404^{+203}_{-78}	2.08 ± 0.58	0.416 ± 0.160	$0.95^{+1.22}_{-0.42}$	PS
SL J0222.8–0416	6	$0.3219^{+0.0036}_{-0.0035}$	970^{+164}_{-9}	2.89 ± 1.62	0.566 ± 0.328	$7.43^{+4.99}_{-4.18}$	PS
SL J0224.4–0449	10	$0.4945^{+0.0006}_{-0.0002}$	271^{+355}_{-202}	1.52 ± 0.26	0.388 ± 0.101	$0.40^{+1.73}_{-0.38}$	PS
SL J0224.5–0414	12	$0.2627^{+0.0003}_{-0.0004}$	268^{+223}_{-51}	1.87 ± 0.36	0.319 ± 0.089	$0.32^{+0.76}_{-0.13}$	FB
SL J0225.3–0441	7	$0.2642^{+0.0013}_{-0.0006}$	530^{+622}_{-148}	2.22 ± 0.84	0.379 ± 0.226	$1.48^{+5.55}_{-0.91}$	PS
SL J0225.4–0414	8	$0.1419^{+0.0003}_{-0.0007}$	400^{+411}_{-113}	1.43 ± 0.79	0.150 ± 0.257	$0.34^{+1.06}_{-0.25}$	PS
SL J0225.7–0312	15	$0.1395^{+0.0006}_{-0.0010}$	739^{+150}_{-86}	1.91 ± 0.31	0.197 ± 0.068	$1.50^{+0.71}_{-0.41}$	CS
SL J0228.1–0450	13	$0.2948^{+0.0006}_{-0.0006}$	447^{+82}_{-52}	2.42 ± 0.33	0.447 ± 0.049	$1.25^{+0.53}_{-0.32}$	NS
SL J0850.5+4512	15	$0.1935^{+0.0007}_{-0.0009}$	650^{+115}_{-53}	2.57 ± 0.37	0.346 ± 0.069	$2.05^{+0.84}_{-0.43}$	CS
SL J1000.7+0137	14	$0.2166^{+0.0002}_{-0.0006}$	729^{+526}_{-439}	2.39 ± 0.50	0.352 ± 0.096	$2.61^{+3.17}_{-2.27}$	CS
SL J1001.2+0135A	11	$0.2205^{+0.0024}_{-0.0026}$	1382^{+337}_{-160}	2.15 ± 0.60	0.322 ± 0.156	$8.58^{+5.25}_{-3.02}$	PS
SL J1001.2+0135B	11	$0.3657^{+0.0012}_{-0.0013}$	931^{+315}_{-170}	2.16 ± 0.46	0.460 ± 0.110	$5.57^{+4.57}_{-2.20}$	PS
SL J1047.3+5700A	6	$0.2427^{+0.0013}_{-0.0002}$	412^{+205}_{-133}	2.54 ± 0.67	0.408 ± 0.081	$0.97^{+1.23}_{-0.58}$	PS
SL J1047.3+5700B	10	$0.3045^{+0.0007}_{-0.0016}$	691^{+143}_{-95}	2.88 ± 0.53	0.544 ± 0.088	$3.62^{+1.78}_{-1.15}$	PS
SL J1048.1+5730	9	$0.3173^{+0.0008}_{-0.0008}$	448^{+138}_{-59}	1.69 ± 0.36	0.328 ± 0.071	$0.92^{+0.68}_{-0.30}$	PS
SL J1049.4+5655	6	$0.4210^{+0.0004}_{-0.0004}$	276^{+112}_{-71}	2.23 ± 1.05	0.520 ± 0.282	$0.55^{+0.60}_{-0.36}$	PS
SL J1057.5+5759	18	$0.6011^{+0.0021}_{-0.0021}$	1552^{+320}_{-204}	2.52 ± 0.44	0.709 ± 0.087	$23.83^{+11.62}_{-7.20}$	FB
SL J1135.6+3009	15	$0.2078^{+0.0008}_{-0.0012}$	893^{+365}_{-145}	2.30 ± 0.63	0.329 ± 0.168	$3.65^{+3.73}_{-1.48}$	CS
SL J1201.7–0331	8	$0.5218^{+0.0042}_{-0.0019}$	1221^{+425}_{-279}	1.38 ± 0.65	0.361 ± 0.269	$7.51^{+7.08}_{-4.66}$	PS
SL J1204.4–0351	14	$0.2609^{+0.0008}_{-0.0005}$	568^{+374}_{-94}	2.70 ± 0.54	0.457 ± 0.083	$2.06^{+3.63}_{-0.75}$	CS
SL J1334.3+3728	21	$0.3012^{+0.0015}_{-0.0017}$	1443^{+199}_{-164}	2.42 ± 0.21	0.454 ± 0.024	$13.20^{+4.04}_{-3.04}$	NS
SL J1335.7+3731	14	$0.4070^{+0.0040}_{-0.0017}$	1064^{+166}_{-88}	2.22 ± 0.38	0.506 ± 0.087	$8.00^{+3.02}_{-1.86}$	CS
SL J1337.7+3800	16	$0.1798^{+0.0009}_{-0.0004}$	783^{+285}_{-248}	3.04 ± 0.34	0.387 ± 0.045	$3.31^{+2.87}_{-1.80}$	CS
SL J1601.6+4245A	7	$0.2075^{+0.0004}_{-0.0007}$	285^{+97}_{-36}	3.07 ± 0.68	0.437 ± 0.086	$0.50^{+0.41}_{-0.16}$	PS
SL J1601.6+4245B	8	$0.4702^{+0.0015}_{-0.0014}$	965^{+694}_{-285}	3.12 ± 0.54	0.774 ± 0.086	$10.05^{+19.73}_{-5.35}$	PS
SL J1602.8+4335	15	$0.4156^{+0.0005}_{-0.0018}$	675^{+589}_{-265}	2.74 ± 0.37	0.632 ± 0.043	$4.03^{+10.11}_{-2.59}$	CS
SL J1605.4+4244	6	$0.2233^{+0.0014}_{-0.0068}$	1525^{+382}_{-188}	2.03 ± 0.80	0.306 ± 0.200	$9.94^{+6.85}_{-4.56}$	PS
SL J1607.9+4338	9	$0.3109^{+0.0004}_{-0.0004}$	273^{+66}_{-40}	1.52 ± 0.44	0.291 ± 0.173	$0.30^{+0.19}_{-0.12}$	PS
SL J1634.1+5639	13	$0.2377^{+0.0017}_{-0.0021}$	1402^{+334}_{-121}	2.28 ± 0.66	0.360 ± 0.126	$9.87^{+5.99}_{-3.29}$	CS
SL J1647.7+3455	12	$0.2592^{+0.0010}_{-0.0008}$	673^{+158}_{-99}	2.09 ± 0.26	0.352 ± 0.053	$2.23^{+1.20}_{-0.67}$	CS

5. Weak lensing analysis

5.1. Basic equations

Let us first summarize several expressions useful for weak lensing analysis. We closely follow the notation of Bartelmann & Schneider (2001). For more details, see that excellent review and references therein.

The aim of weak lensing mass reconstruction is to measure the dimensionless surface mass density, frequently called the gravitational lensing density,

$$\kappa = \frac{\Sigma}{\tilde{\Sigma}_{cr}(z_l)}, \quad (3)$$

where Σ is the two-dimensional projected mass density, and $\tilde{\Sigma}_{cr}(z_l)$ is the source weighted critical density

$$\tilde{\Sigma}_{cr}(z_l) = \frac{c^2}{4\pi G D_l} \frac{\int_{z_l}^{\infty} dz_s n_s(z_s) D_s / D_{ls}}{\int_0^{\infty} dz_s n_s(z_s)}, \quad (4)$$

where $n_s(z)$ is the redshift distribution of source galaxies, and D_l , D_s , D_{ls} are the angular diameter distances from the observer to a lens, the observer to a source and the lens and a source, respectively.

Our weak lensing mass reconstruction used the Fourier space relation between κ and the gravitational lensing shear γ (Kaiser & Squires 1993). Note that the directly observable quantity is not γ but the reduced shear

$$g = \frac{\gamma}{1 - \kappa}. \quad (5)$$

We adopt the weak lensing approximation, $g \simeq \gamma$, because most of our signal lies in the wings of clusters, where $\kappa \lesssim 0.1$ (see Figures 8-43).

5.2. Source redshift distribution

For the redshift distribution of source galaxies, we adopted the conventional parametric model,

$$n_s(z) = \frac{\beta}{z_* \Gamma[(1+\alpha)/\beta]} \left(\frac{z}{z_*}\right)^\alpha \exp\left[-\left(\frac{z}{z_*}\right)^\beta\right]. \quad (6)$$

The mean redshift is given by $\langle z_s \rangle = z_* \Gamma[(2+\alpha)/\beta] / \Gamma[(1+\alpha)/\beta]$. Since our galaxy catalog ($R_C < 25.5$ mag [Vega]) was much deeper than any sizable galaxy catalog with spectroscopic redshifts, the redshift distribution of our galaxies is uncertain. We took a fiducial model of $\langle z_s \rangle = 1$, $\alpha = 1.5$ and $\beta = 1$, and evaluated two errors arising from uncertainty in the model parameters. The first error, due to uncertainty in $\langle z_s \rangle$, we denote as σ_{z_s} . We evaluate this in the standard manner as $\sigma_{z_s} = d\tilde{\Sigma}_{cr}/dz_s \delta z_s$, and consider an uncertainty of $\delta z_s = 0.2$. We found $\sigma_{z_s} \simeq 0.2 \times z_l$ for $z_l < 0.35$ and $\sigma_{z_s} \simeq 0.07$ for $z_l > 0.35$. The second error, due to uncertainty in α and β , we denote as σ_{n_s} . In order to evaluate this, we considered two models of $(\alpha, \beta) = (2, 1.5)$ and $(3, 2)$. The relative differences in $\tilde{\Sigma}_{cr}$ from the fiducial model were found to be about 10 percent or less at the redshifts of our clusters. We therefore decided to take $\sigma_{n_s} = 0.1 \times \tilde{\Sigma}_{cr}$. These errors were properly propagated to the errors in weak lensing mass and the SIS velocity dispersion (see below).

5.3. Aperture densitometry

One convenient way to compute the mass of galaxy clusters exploits the relation between κ and the tangential shear, γ_t (Squires & Kaiser 1996)

$$\langle \gamma_t \rangle(\theta) = -\frac{1}{2} \frac{d\bar{\kappa}}{d \ln \theta}, \quad (7)$$

where $\langle \gamma_t \rangle$ is the azimuthal average of the tangential shear, and $\bar{\kappa}$ is the averaged κ over a circular aperture with radius θ . From this, one can obtain an expression for the average projected density within a radius θ_1 , $\bar{\kappa}(\theta < \theta_1)$, subtracted from that within an annulus $\theta_2 < \theta < \theta_3$, $\bar{\kappa}(\theta_2 < \theta < \theta_3)$,

$$\begin{aligned} \zeta(\theta_1, \theta_2, \theta_3) &= \bar{\kappa}(\theta < \theta_1) - \bar{\kappa}(\theta_2 < \theta < \theta_3) \\ &= 2 \int_{\theta_1}^{\theta_2} d \ln \theta \langle \gamma_t \rangle \\ &\quad + \frac{2}{1 - \theta_2^2 / \theta_3^2} \int_{\theta_2}^{\theta_3} d \ln \theta \langle \gamma_t \rangle. \end{aligned} \quad (8)$$

This is the so-called ζ -statistic. In our computation of ζ , we adopted the weak lensing approximation $\gamma \simeq g$, which should be valid in all but the very inner part of clusters ($r \lesssim 100$ kpc or $\theta \lesssim 0.5$ arcmin). It is then straightforward to relate ζ with the aperture mass,

$$M(< \theta) = \pi \theta^2 \zeta(\theta, \theta_2, \theta_3) \tilde{\Sigma}_{cr}. \quad (9)$$

This is the mass within an aperture θ minus an unknown mass. While the value of this additional mass is difficult to evaluate, it presumably tends to zero if θ_2 is sufficiently large to be hardly affected by the cluster mass. We took $\theta_2 = 10$ arcmin and $\theta_3 = 20$ arcmin. The statistical error in ζ was estimated from the rms of 100 recalculations of ζ ,

each time randomizing the orientation of galaxy ellipticities. This error was propagated to $M(< \theta)$ in the standard manner. The results are presented in Figures 8-43.

5.4. Lens models of clusters

An alternative way to estimate the cluster mass from weak lensing data is to fit the shear profile to an analytical model of a galaxy cluster. One merit of this method over the ζ -statistic is that this is free from the uncertainty in the additive mass (see §5.3). It is also of fundamental importance to check that a model prediction agrees with the observed shear profile, to provide a direct observational test on the theoretical model.

5.4.1. NFW model

Currently, the most successful model is that proposed by Navarro, Frenk & White (1996; 1997; NFW hereafter). We adopted a truncated NFW model, in which the density profile is truncated at the virial radius

$$\rho_{\text{nfw}}(x) = \begin{cases} \frac{\rho_s}{r/r_s(1+r/r_s)^2}, & \text{for } r < r_{\text{vir}} \\ 0 & \text{otherwise,} \end{cases} \quad (10)$$

where r_s and r_{vir} are the scale radius and virial radius respectively. It is convenient to introduce the concentration parameter $c_{\text{nfw}} = r_{\text{vir}}/r_s$. Bullock et al. (2001) found from N -body simulations that the concentration parameter is related to halo mass as

$$c_{\text{nfw}}(M, z) = \frac{c_*}{1+z} \left(\frac{M}{10^{14} h^{-1} M_\odot} \right)^{-0.13}, \quad (11)$$

where $c_* \simeq 8$ for the Λ CDM model. By definition, the mass enclosed within a sphere of radius r_{vir} gives the virial mass

$$M_{\text{vir}} = 4\pi \rho_s r_s^3 \left[\log(1 + c_{\text{nfw}}) - \frac{c_{\text{nfw}}}{1 + c_{\text{nfw}}} \right]. \quad (12)$$

The virial mass is also defined from the spherical top-hat collapse model as

$$M_{\text{vir}} = \frac{4\pi}{3} \delta_{\text{vir}}(z) \bar{\rho}(z) r_{\text{vir}}^3, \quad (13)$$

where δ_{vir} is the threshold over-density for spherical collapse (see Nakamura & Suto 1997 and Henry 2000 for useful fitting functions). Using equations (12) and (13), one can express ρ_s in terms of $\delta_{\text{vir}}(z)$ and c_{nfw} . Introducing $\delta_s = \rho_s / \bar{\rho} - 1$, one finds

$$\delta_s = \frac{\delta_{\text{vir}}}{3} \frac{c_{\text{nfw}}^3}{\log(1 + c_{\text{nfw}}) - c_{\text{nfw}}/(1 + c_{\text{nfw}})}. \quad (14)$$

Thus the density profile of the NFW halo can be characterized by two parameters: the virial mass M_{vir} and the concentration parameter c_{nfw} . In the following analyses we fixed the mass-concentration relation to the empirical result, eq. (11). This is necessary because, with high S/N measurements of the tangential shear in only a limited angular range (typically $1 < \theta < 4$ arcmin), only a poor constraint on the concentration parameter is obtained. See Appendix 1 for details.

Cluster masses are also often defined by M_{200} , which is the mass contained within the radius r_{200} , where the mean mass density of the halo is equal to 200 times the

Table 3. Summary of weak lensing analyses: (a) the amplitude of tangential shear profile at 1 arcmin, when fitted with an *SIS* model (see §5.4.2). (b) the *SIS* velocity dispersion parameter. (c) the virial mass estimated by fitting the radial shear profile with an NFW model. (d) the M_{200} estimated adopting the NFW model. (e) the M_{500} estimated adopting the NFW model. (f) the virial radius computed from the NFW mass using the relation eq (13).

Name	z_c	$\gamma_{\text{sis}}^{(a)}$	$\sigma_{\text{SIS}}^{(b)}$ [km/s]	$M_{\text{NFW}}^{(c)}$	$M_{200}^{(d)}$ [$\times 10^{14} h^{-1} M_{\odot}$]	$M_{500}^{(e)}$	$r_{\text{vir}}^{(f)}$ [comoving $\text{Mpc} h^{-1}$]
SL J0217.3–0524	0.4339	0.048	723 ⁺⁴³⁹ _{–451}	1.95 ^{+1.44} _{–0.95}	1.71 ^{+1.26} _{–0.83}	1.20 ^{+0.88} _{–0.58}	1.3
SL J0219.6–0453	0.3322	0.072	789 ⁺³⁸³ _{–409}	2.75 ^{+1.25} _{–1.02}	2.37 ^{+1.08} _{–0.88}	1.67 ^{+0.76} _{–0.62}	1.5
SL J0222.8–0416	0.3219	0.058	695 ⁺³⁸⁸ _{–408}	2.09 ^{+0.09} _{–0.40}	1.81 ^{+0.08} _{–0.35}	1.28 ^{+0.06} _{–0.24}	1.3
SL J0224.4–0449	0.4945	0.071	946 ⁺⁴³⁷ _{–477}	4.79 ^{+0.83} _{–1.42}	4.19 ^{+0.73} _{–1.24}	2.85 ^{+0.49} _{–0.84}	1.8
SL J0224.5–0414	0.2627	0.066	679 ⁺³¹⁰ _{–340}	1.78 ^{+0.73} _{–0.59}	1.53 ^{+0.63} _{–0.51}	1.09 ^{+0.45} _{–0.36}	1.3
SL J0225.3–0441	0.2642	0.087	800 ⁺⁴⁰⁵ _{–425}	3.02 ^{+1.32} _{–1.04}	2.58 ^{+1.13} _{–0.89}	1.82 ^{+0.80} _{–0.63}	1.5
SL J0225.4–0414	0.1415	0.059	573 ⁺²⁷³ _{–293}	1.86 ^{+0.45} _{–0.45}	1.57 ^{+0.38} _{–0.38}	1.14 ^{+0.27} _{–0.27}	1.2
SL J0225.7–0312	0.1395	0.112	790 ⁺³⁵⁶ _{–379}	2.95 ^{+0.83} _{–0.79}	2.48 ^{+0.70} _{–0.66}	1.77 ^{+0.50} _{–0.47}	1.4
SL J0228.1–0450	0.2948	0.102	898 ⁺⁵²³ _{–527}	4.37 ^{+1.67} _{–1.86}	3.73 ^{+1.43} _{–1.59}	2.60 ^{+0.99} _{–1.11}	1.7
SL J0850.5+4512	0.1935	0.068	650 ⁺³⁶¹ _{–371}	1.95 ^{+1.17} _{–0.77}	1.66 ^{+0.99} _{–0.65}	1.19 ^{+0.71} _{–0.47}	1.3
SL J1000.7+0137	0.2166	0.091	775 ⁺³³² _{–347}	2.69 ^{+1.03} _{–0.32}	2.29 ^{+0.88} _{–0.27}	1.63 ^{+0.62} _{–0.19}	1.4
SL J1048.1+5730	0.3173	0.069	758 ⁺⁴⁴¹ _{–435}	2.51 ^{+1.13} _{–1.03}	2.16 ^{+0.97} _{–0.89}	1.53 ^{+0.69} _{–0.63}	1.4
SL J1049.4+5655	0.4210	0.091	983 ⁺⁵⁰² _{–525}	3.72 ^{+3.28} _{–0.70}	3.23 ^{+2.85} _{–0.61}	2.23 ^{+1.97} _{–0.42}	1.6
SL J1057.5+5759	0.6011	0.087	1194 ⁺⁵²³ _{–544}	8.71 ^{+2.58} _{–1.56}	7.65 ^{+2.27} _{–1.37}	5.05 ^{+1.50} _{–0.90}	2.2
SL J1135.6+3009	0.2078	0.100	804 ⁺³⁴⁴ _{–373}	4.17 ^{+0.69} _{–1.06}	3.52 ^{+0.58} _{–0.90}	2.48 ^{+0.41} _{–0.63}	1.6
SL J1201.7–0331	0.5219	0.087	1085 ⁺⁵²⁷ _{–530}	7.24 ^{+2.97} _{–2.46}	6.32 ^{+2.59} _{–2.15}	4.23 ^{+1.74} _{–1.44}	2.1
SL J1204.4–0351	0.2609	0.098	844 ⁺⁴²⁷ _{–460}	3.55 ^{+1.64} _{–1.28}	3.03 ^{+1.40} _{–1.09}	2.13 ^{+0.98} _{–0.77}	1.6
SL J1334.3+3728	0.3006	0.123	991 ⁺⁴⁵⁴ _{–482}	4.79 ^{+1.67} _{–1.35}	4.09 ^{+1.43} _{–1.15}	2.84 ^{+0.99} _{–0.80}	1.8
SL J1335.7+3731	0.4070	0.093	978 ⁺⁴⁵² _{–493}	6.61 ^{+2.18} _{–1.92}	5.70 ^{+1.88} _{–1.66}	3.88 ^{+1.28} _{–1.13}	2.0
SL J1337.7+3800	0.1798	0.071	655 ⁺³¹³ _{–346}	1.62 ^{+0.69} _{–0.42}	1.38 ^{+0.59} _{–0.36}	1.00 ^{+0.42} _{–0.26}	1.2
SL J1602.8+4335	0.4155	0.087	954 ⁺⁴¹⁸ _{–418}	4.79 ^{+1.20} _{–1.05}	4.15 ^{+1.04} _{–0.91}	2.85 ^{+0.71} _{–0.62}	1.8
SL J1605.4+4244	0.2233	0.066	665 ⁺³¹⁹ _{–342}	1.82 ^{+0.79} _{–0.63}	1.55 ^{+0.67} _{–0.54}	1.12 ^{+0.48} _{–0.39}	1.2
SL J1607.9+4338	0.3109	0.063	718 ⁺⁴¹⁸ _{–447}	1.74 ^{+0.04} _{–0.74}	1.50 ^{+0.03} _{–0.64}	1.07 ^{+0.02} _{–0.46}	1.3
SL J1634.1+5639	0.2377	0.076	724 ⁺⁴⁰² _{–404}	2.09 ^{+1.01} _{–0.87}	1.79 ^{+0.86} _{–0.74}	1.28 ^{+0.62} _{–0.53}	1.3
SL J1647.7+3455	0.2592	0.079	759 ⁺⁵⁵¹ _{–560}	4.90 ^{+2.48} _{–1.89}	4.16 ^{+2.11} _{–1.60}	2.90 ^{+1.47} _{–1.12}	1.8

critical density at the redshift of the cluster. In order to allow the direct comparison with other works, we compute M_{200} assuming the NFW profile.

Analytical expressions for weak lensing convergence and shear behind an NFW profile are given in Takada & Jain (2003a; b). Note that those expressions differ from those by Bartelmann (1996) and Wright & Brainerd (2000). The latter are for a non-truncated NFW halo and give a larger surface mass density than ours due to the infinite extend of the mass. In Appendix 1, we illustrate how the shear and projected mass profile depend on the virial mass and scale radius.

5.4.2. *SIS* model

The singular isothermal sphere (SIS) model has frequently been adopted as a lens model, because of its simplicity. One convenient feature of this model is that it provides an estimate of the velocity dispersion, which is a useful measure of the gravitational potential and allows a direct comparison with the observed velocity dispersion in galaxies.

The density profile of the SIS model is

$$\rho_{\text{sis}}(r) = \frac{\sigma_{\text{sis}}^2}{2\pi G} \frac{1}{r^2}, \quad (15)$$

where σ_{sis} is the SIS velocity dispersion. The mass within

a radius r is

$$M_{\text{SIS}}(< r) = \frac{2\sigma_{\text{sis}}^2}{G} r. \quad (16)$$

The projected density is

$$\Sigma(y) = \int dz \rho_{\text{sis}}(y, z) = \frac{\sigma_{\text{sis}}^2}{2G} \frac{1}{y}, \quad (17)$$

where y is a radial coordinate in the plane perpendicular to the line-of-sight direction. The shear profile is

$$\begin{aligned} \gamma(\theta) &= \frac{1}{\Sigma_{cr}} \frac{\sigma_{\text{sis}}^2}{2G} \frac{1}{D_l \theta} \\ &\equiv \frac{\gamma_{\text{sis}}}{(\theta/1\text{arcmin})}, \end{aligned} \quad (18)$$

where θ is the angular separation from the lens center, and we define γ_{sis} as the amplitude of shear profile at $\theta = 1$ arcmin. We evaluated γ_{sis} by fitting the measured shear over the range $1 < \theta < 4$ arcmin. We used this range for three reasons: (1) for most clusters, the shear signal was measured with a good S/N throughout this interval, but degraded outside it. (2) at larger radii, nearby structures (either physically related or unrelated to the main cluster) could contribute to the shear signal. (3) at smaller radii, the reduced shear g , and the dilution effect due to

the cluster member galaxies could have non-negligible effect on the shear signal (Broadhurst et al. 2004). The measured γ_{sis} values are summarised in Table 3.

By combining equations for the definition of virial mass (13) and the mass in a SIS (16), one finds

$$M_{\text{SIS}}(< r_{\text{vir}}) = \left[\frac{6}{\pi} \frac{\sigma_{\text{sis}}^6}{G^3 \delta_{\text{vir}}(z_l) \bar{\rho}(z)} \right]^{1/2} \\ \simeq 6.6 \times 10^{14} [h^{-1} M_{\odot}] \\ \times C \times \left(\frac{\sigma_{\text{sis}}}{1000 \text{km/s}} \right)^3, \quad (19)$$

where

$$C \equiv \left[\frac{1}{\Omega_m} \frac{1}{(1+z_l)^3} \frac{200}{\delta_{\text{vir}}(z_l)} \right]^{\frac{1}{2}}. \quad (20)$$

In the notation of Bryan & Norman (1998) C is written by $C = (200/\Delta_c)^{1/2} E(z)^{-1}$, where Δ_c is the critical overdensity of the spherical collapse, and

$$E(z) = \frac{H(z)}{H_0} = [\Omega_m(1+z)^3 + \Omega_{\Lambda}]^{1/2} \quad (21)$$

for a Λ -flat cosmology. A reasonably accurate fitting function of C for a Λ -cosmology ($\Omega_m = 0.3$, $\Omega_{\Lambda} = 0.7$) over the redshift range $0 < z_l < 0.8$ is found to be $C \simeq 1.44/(1+z_l)^{1.08}$, and in the case of Einstein-de Sitter cosmology ($\Omega_m = 1$, $\Omega_{\Lambda} = 0$), it reduces to $C = \sqrt{200/178}/(1+z_l)^{1.5} \simeq 1.06/(1+z_l)^{1.5}$.

5.5. Results

The results of our weak lensing analyses are compiled in Table 3. A detailed discussion of each system is presented in Appendix 2, including a comparison of weak lensing and optical properties, and the results of MOS observations.

6. Cluster scaling relations

6.1. Clean sample of clusters

We shall now examine statistical relations between the dynamical mass estimator (σ_v) and the weak lensing mass estimators (σ_{sis} and M_{NFW}). In this paper, we shall restrict our analysis to clusters with the very cleanest measurements; a statistical treatment of the entire sample, taking into account all selection effects, will follow in Green et al. (in preparation). We define a *clean (sub)-sample* of clusters (“CS” in Table 2) as those whose velocity dispersion was evaluated from at least 12 spectroscopic member galaxies, and whose weak lensing mass estimation could not have been affected by proximity to either a neighboring system (“NS”) or a field boundary (“FB”). Ten clusters satisfy these criteria.

We additionally include two clusters in our survey area whose velocity dispersions have been measured by other authors. Observations by Willis et al. (2005) of SL J0221.7–0345 ($z = 0.43$, $\sigma_v = 821^{+92}_{-74}$ km/s from 39 galaxy redshifts) and SL J0228.4–0425 ($z = 0.43$, $\sigma_v = 694^{+204}_{-91}$ km/s from 13 redshifts) satisfy the same stringent selection criteria as above. We examine the weak lensing

properties of those clusters in the same manner described in §5, and the results are described fully in Appendix 3.

6.2. Velocity dispersions

The relation between cluster galaxies’ velocity dispersion (σ_v) and the velocity dispersion parameter of the best-fit SIS model (σ_{sis}) has been measured for various clusters, in the context of their dynamical status (Irgens et al. 2002; Hoekstra et al. 2002; Hoekstra 2007; Milvang-Jensen et al. 2008). Results for our sample are presented in figure 2 (with a comparison to optically selected clusters) and figure 3 (with a comparison to X-ray selected clusters). The optically selected catalog of Milvang-Jensen et al. (2008) contains less massive clusters, at higher redshift ($\bar{z} = 0.58$) than our sample ($\bar{z} = 0.28$). Conversely, the wide but shallow Einstein Medium Sensitivity Survey (EMSS; Gioia et al. 1990) and X-ray Brightest Abell Cluster Survey (XBACS; Ebeling et al. 1996) include the most massive clusters at more modest redshift. The mean redshift of the catalog by Cypriano et al. (2004) is $\bar{z} = 0.13$ and by Hoekstra (2007) is $\bar{z} = 0.31$.

Only a few outliers in Figures 2 and 3 are inconsistent with $\sigma_v = \sigma_{\text{sis}}$. The main outlier from our sample, SL J1634.1+5639, has $\sigma_v \sim 2\sigma_{\text{sis}} \sim 1400$ km/s, but the velocity distribution of spectroscopic member galaxies is also strongly skewed (see Figure 1). The reason for this is currently not clear, but discussed further in Appendix 2.34. Overall, despite variations in samples’ range of cluster masses and redshifts, the scatter in the $\sigma_v - \sigma_{\text{sis}}$ relation is remarkably similar for all four catalogs. Thus, as far as the relation between σ_v and σ_{sis} is concerned, no strong selection bias is identified between the various cluster detection techniques.

It is worth noting that the density (and shear) profile of a real cluster is typically *not* a single power law. The best-fit SIS model, and value of σ_{sis} , may therefore depend on the specific fitting method, and the range over which data are fit. Our above finding, that $\sigma_v \simeq \sigma_{\text{sis}}$, may therefore be somewhat method-dependent. A corollary of this issue is that it might also be possible to minimize scatter in the $\sigma_v - \sigma_{\text{sis}}$ relation by optimizing the fitting method used to obtain σ_{sis} . We have not attempted to do this.

6.3. Velocity dispersion versus mass

We next examine the relation between the velocity dispersion of a cluster’s galaxies (σ_v) and its weak lensing mass. Since the NFW virial masses and aperture masses agree for all 12 cleanly-measured clusters, we adopt $M_{\text{vir}} = M_{\text{NFW}}$ as our sole weak lensing mass estimate. Figure 4 shows our results, and compares them to measurements of X-ray selected clusters by Hoekstra (2007). It is important to note that weak lensing measurements do not depend upon the dynamical status of the clusters. Motivated by SIS model prediction (eqs (19) and (20)), we adopt a functional form of the scaling relation $M_{\text{vir}} \propto M_* \sigma_v^p / (1+z_c)^{1.08}$. For pure SIS clusters in a Λ CDM cosmology, the parameters would be $p = 3$ and $M_* = 9.5 \times 10^{14}$ (see eq. (19) and below). This simplistic toy model is shown as a dotted line, and al-

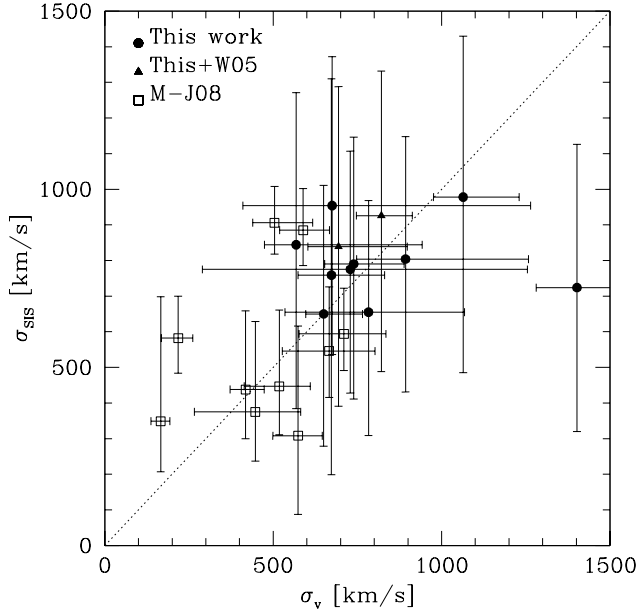


Fig. 2. Comparison between the velocity dispersion measured from galaxy redshifts (σ_v) and the velocity dispersion parameter of the weak lensing SIS model (σ_{SIS}). Filled circles show our *clean sample* (see text). Filled triangles show two clusters whose σ_v was measured by Wills et al. (2005) (see Appendix 3). Open squares show optically selected clusters from Milvang-Jensen et al. (2008; note that clusters with structures possibly affecting the velocity dispersion estimate are excluded, see §8 of their paper for details).

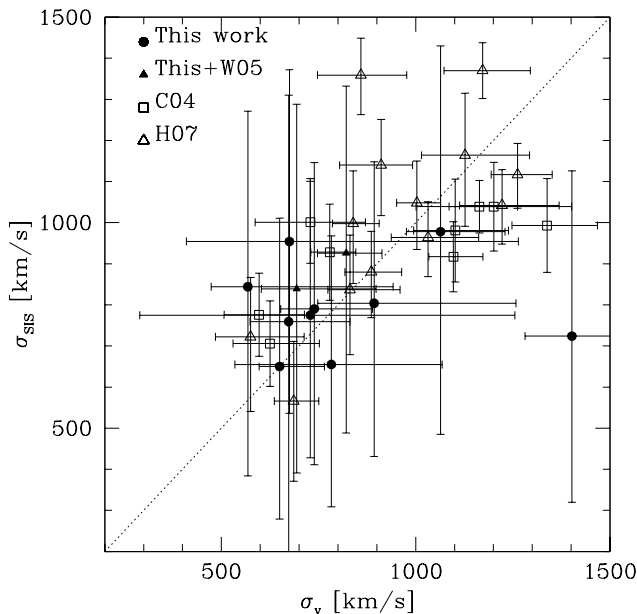


Fig. 3. Same as Fig 2 but compared with X-ray selected clusters from Cypriano et al. (2004; open squares) and Hoekstra (2007, open triangles).

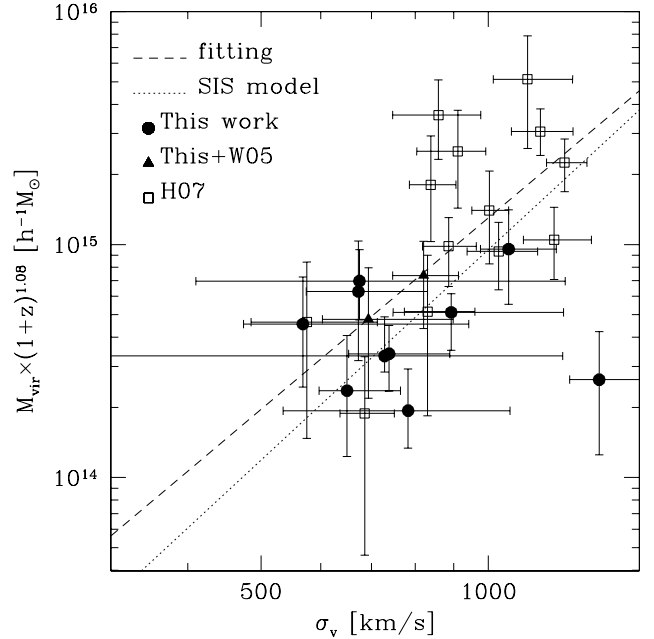


Fig. 4. Comparison between the velocity dispersion measured from galaxy redshifts (σ_v) and the virial mass measured from weak lensing (M_{NFW}). In order to account for redshift evolution in the relation, cluster masses were multiplied by a factor of $(1+z_c)^{1.08}$ (as motivated by eqs (19) and (20)). The filled circles show clusters in this study; the two filled triangles show clusters in this study whose σ_v were measured by Wills et al. (2005) (see Appendix 3), and the open circles show the sample of Hoekstra (2007). The dotted line shows the prediction of a pure SIS model, $M_{\text{vir}} \times (1+z_c)^{1.08} = 9.5 \times 10^{14} \times (\sigma_v/1000\text{km/s})^3 h^{-1} M_{\odot}$. The dashed line shows the best-fit empirical relation, $M_{\text{vir}} \times (1+z_c)^{1.08} = 13 \times 10^{14} \times (\sigma_v/1000\text{km/s})^{2.7} h^{-1} M_{\odot}$.

ready provides a reasonable approximation to the observed $M_{\text{vir}} - \sigma_v$ data. A least-squares fit (excluding the outlier SL J1634.1+5639) yields $M_{\text{vir}}(1+z_c)^{1.08} = (13 \pm 2) \times 10^{14} \times (\sigma_v/1000\text{km/s})^{2.7 \pm 0.6} h^{-1} M_{\odot}$. The best-fit power-index is thus consistent with the SIS prediction of 3, but the normalization is slightly higher.

A more sophisticated prediction of the cluster $M - \sigma_v$ relation, using N -body simulations, was obtained by Evrard et al. (2008). They find $M_{200} E(z) = 9.358 \times 10^{14} \times (\sigma_v/1000\text{km/s})^{2.975} h^{-1} M_{\odot}$, and argue that it is insensitive to cosmological parameters in a variety of CDM models. To aid in comparison, we estimate M_{200} from our measurements of M_{NFW} by assuming every cluster has an NFW density profile. These masses are listed in Table 3 and our results are shown in Figure 5, together with those of Hoekstra (2007). Evrard et al.'s prediction is overlaid as a dotted line, and the best-fit power-law model (excluding the outlier SL J1634.1+5639), $M_{200} E(z) = (9.6 \pm 1.6) \times 10^{14} \times (\sigma_v/1000\text{km/s})^{2.7 \pm 0.6} h^{-1} M_{\odot}$, as a dashed line.

Interpretation of this apparent consistency is not trivial because Evrard et al. evaluated σ_v from simulated dark matter particles instead of galaxies. However, since both galaxies and cold dark matter particles may be safely regarded as collisionless particles in the cluster potential, it is reasonable to assume that they have approximately the

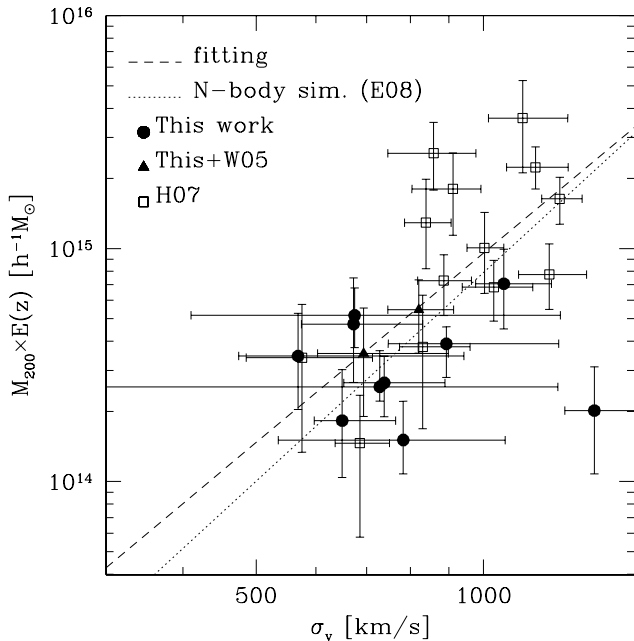


Fig. 5. Same as Figure 4 but with M_{200} instead of virial mass M_{NFW} , for comparison with numerical simulations. The dotted line shows a prediction from N -body simulations $M_{200} E(z) = 9.358 \times 10^{14} \times (\sigma_v/1000\text{km/s})^{2.975} h^{-1} M_{\odot}$ (Evrard et al. 2008). The dashed line shows the best-fit empirical relation $M_{200} E(z) = 9.6 \times 10^{14} \times (\sigma_v/1000\text{km/s})^{2.7} h^{-1} M_{\odot}$.

same velocity dispersion outside a central region in which the effect of dynamical friction is important (Okamoto & Habe 1999). If this is the case, our findings indicate that the dynamical structure of galaxy clusters is indeed consistent with that expected in the standard CDM paradigm of structure formation. It will be interesting to compare our observations with simulations of cluster evolution that also incorporate mechanisms for galaxy formation.

7. Summary and Discussions

We have presented the results of a multi-object spectroscopic campaign to target 36 cluster candidates located by the Subaru weak lensing survey (Miyazaki et al. 2007). We obtained the redshifts of 15–32 galaxies within a few arcminutes of each cluster candidate. Our primary goals were to search for a spatial concentration of galaxies as an optical counterpart of each weak lensing density peak, and to determine the cluster redshifts. We found 31 galaxy concentrations containing more than five spectroscopic galaxies within a velocity of $\pm 3000\text{km/s}$, and determined their redshifts. These included 25 detections of isolated clusters, and three systems (SL J1000.7.3+0137, SL J1047.3+5700, SL J1601.6+4245) in which two galaxy clusters are projected at different redshifts along the same line-of-sight. This demonstrates that spectroscopic follow-up of weak lensing cluster candidates is a reliable way not only to identify their optical counterparts but also to distinguish superposed systems.

We have therefore identified secure optical counterparts

of the weak lensing signal in 28 out of 36 targets. In 6 of the 8 unconfirmed cluster candidates, we found multiple small galaxy concentrations at different redshifts (each containing at least 3 spectroscopic galaxies). This suggests that the weak lensing signal in those cases may arise from the projection of small clusters along the same line-of-sight. However, it is also possible that a real, massive cluster is responsible for the weak lensing density peak, but was missed by our relatively sparse MOS observations. This is also the case for the final two unconfirmed candidates, where only a single small galaxy concentration was identified. In order to obtain a firm confirmation of the optical counterpart of such unconfirmed candidates, denser spectroscopic observations would be required.

We measured the mass of single cluster systems with known redshifts using two weak lensing methods: aperture densitometry and by fitting the shear profile to an NFW model. In most cases, the two mass estimators agree well: providing observational support for the NFW model. In the few clusters where the mass estimators did not agree, the weak lensing κ signal clearly deviates from spherical symmetry. This could account for the disagreement. It was also found, by eye, that the aperture mass profile of some clusters does not flatten even at a large radius of $\theta \sim 10$ arcmin. This can be accounted for by the mass contribution from surrounding structures. We found some candidates of super-cluster systems, whose weak lensing mass reconstructions show evidence of filamentary structure connecting the main cluster to surrounding systems.

We investigated statistical relations between clusters' weak lensing properties (σ_{sis} and M_{vir} or M_{200}) and the velocity dispersion of their member galaxies (σ_v), comparing our results to optically and X-ray selected cluster samples from the literature. Although our *clean sample* contained only 12 clusters, we found our clusters to be consistent with $\sigma_v = \sigma_{\text{sis}}$, with a scatter as large as that of optically and X-ray selected samples. Therefore, as far as the relation between σ_v and σ_{sis} is concerned, no strong bias between the cluster selection techniques was identified. We also derived the empirical relation between the cluster virial mass and the galaxy velocity dispersion: $M_{\text{vir}}(1+z_c)^{1.08} = (13 \pm 2) \times 10^{14} \times (\sigma_v/1000\text{km/s})^{2.7 \pm 0.6} h^{-1} M_{\odot}$. The derived $M_{\text{vir}} - \sigma_{\text{sis}}$ relation is similar to theoretical expectations from the SIS model, eq. (19). It is important to note that, unlike the SIS model assumption, real cluster shear profiles (and density profiles) are *not* single power-laws, so this result may depend upon details of the fitting technique. For comparison with numerical simulations, we also derived the $M_{200} - \sigma_v$ relation and found $M_{200} E(z) = (9.6 \pm 1.6) \times 10^{14} \times (\sigma_v/1000\text{km/s})^{2.7 \pm 0.6} h^{-1} M_{\odot}$. This is in good agreement with predictions by Evrard et al. (2008), demonstrating that the dynamical structure of galaxy clusters is similar to that expected in the standard CDM paradigm of structure formation.

We are very grateful to Subaru astronomers: Y. Ohyama, K. Aoki and T. Hattori for their dedicated supports of the FOCAS observing. Numerical computations presented in this paper were carried out on computer sys-

tem at CfCA (Center for Computational Astrophysics) of the National Astronomical Observatory Japan. Data reduction and analysis were in part carried out on general common use computer system at ADAC (Astronomical Data Analysis Center) of the National Astronomical Observatory of Japan. This research was supported in part by the Grants-in-Aid from Monbu-Kagakusho and Japan Society of Promotion of Science: Project number 15340065 (TH&SM) and 17740116 (TH).

References

- Bartelmann M., 1996, *A&A*, 313, 443
 Bartelmann M., Schneider P., 2001, *Physics Report*, 340, 291
 Beers T. C., Flynn K., Gebhardt K., *AJ*, 1990, 100, 32
 Broadhurst T., Takada M., Umetsu K., Kong X., Arimoto N., Chiba M., Futamase T., 2004, *ApJL*, 619, L143
 Bryan G. R., Norman M. L., 1998, *ApJ*, 495, 80
 Bullock J. S., Kolatt T. S., Sigad Y., Somerville R. S., Kravtsov A. V., Klypin A. A., Primack J. R., Dekel A. 2001, *MNRAS*, 321, 559
 Cohen J. G., Hogg D. W., Pahre M. A. Blandford R., Shopbell P. L., Richberg K. *AJ*, 1999, 129, 171
 Cohen J. G., Kneib, j.-P., 2002, *ApJ*, 573, 524
 Cypriano E. S., Sodré, L. Jr., Kneib J.-P., Campusano L. E., 2004, *ApJ*, 613, 95
 Donahue M., Scharf C. A., Mack J., Lee Y. P., Postman M., Rosati P., Dickinson M., Voit G. M., Stocke J. T., 2002, *ApJ*, 569, 689
 Ebeling H., Voges W., Bohringer H., Edge A. C., Huchra J. P., Briel U. G., 1996, *MNRAS*, 281, 799
 Evrard A. E., et al. 2008, *ApJ*, 672, 122
 Gal R. R., De Carvalho R. R., Lopes P. A. A., Djorgovski S. G., Brunner R. J., 2003, *AJ*, 125, 20064
 Gavazzi R., Soucail G., 2007, *A&A*, 462, 459
 Gioia I. M., Maccacaro T., Schild R. E., Wolter A., Stocke J. T., Morris S. L., Henry J. P., 1990, *ApJS*, 72, 1990
 Gunn J. E., Hoessel J. G., Oke, J. B., 1986, *ApJ*, 306, 30
 Hamana T., Takada, M., Yoshida N., 2004, *MNRAS*, 350, 893
 Hennawi J. F., Spergel D. N., 2005, *ApJ*, 624, 59
 Henry, J. P. 2000, *ApJ*, 534, 565
 Hettterscheidt M., Erben T., Schneider P., Maoli R., van Waerbeke L., Mellier Y., 2005, *A&A*, 442, 43
 Hoekstra, H., 2007, 379, 317
 Hoekstra, H., Franx M., Kuijken K., van Dokkum, P. G., 2002, *MNRAS*, 333, 911
 Irgens R., Lilje, P. B., Dahle, H., Maddox, S. J., 2002, *ApJ*, 579, 227
 Jing, Y. P., 2000, *ApJ*, 535, 30
 Kaiser N., Squires G., 1993, *ApJ*, 404, 441
 Kashikawa N., et al., 2002, *PASJ*, 54, 819
 Kolokotronis V., Georgakakis A., Basilakos S., Kitsionas S., Plionis M., Georgantopoulos I., Gaga T., 2006, *MNRAS*, 366, 163
 Limber D. N., Mathews W. G., 1960, *ApJ*, 132, 286
 Massey R., et al, 2007, *Nature*, 445, 286
 Milvang-Jensen B., et al., 2008, *A&A*, 482, 419
 Miyazaki S. et al., 2002, *ApJL*, 580, 97
 Miyazaki S., Hamana, T, Ellis, R. S., Kashikawa, N., Massey R. J., Taylor, J., Refregier, A., 2007, *ApJ*, 669, 714 (P1)
 Mullis C. R., McNamara B R., Quintana H., Vikhlinin A., Henry J. P., Gioia I. M., Hornstrup A., Forman W., Jones C., 2003, *ApJ*, 594, 154
 Nakamura, T. T., & Suto, Y. 1997, *Prog. Theor. Phys.*, 97, 49
 Navarro J., Frenk C., White S. D. M. 1996, *ApJ*, 462, 563
 Navarro J., Frenk C., White S. D. M. 1997, *ApJ*, 490, 493
 Nolthenius R., White S. D. M., 1987, *MNRAS*, 225, 505
 Okabe N., Umetsu K., 2007, *PASJ*, 60, 345
 Okamoto T. Habe A., 1999, *ApJ*, 516, 591
 Pierre M., et al., *MNRAS*, 372, 591
 Saslow W. C., 1985, *Gravitational Physics of Stellar and Galactic Systems* (New York: Cambridge Univ. Press)
 Takada M., Jain B., 2003, *MNRAS*, 340, 580
 Takada M., Jain B., 2003, *MNRAS*, 344, 857
 van Breukelen C. et al. (2006), *MNRAS*, 373, L26
 Vikhlinin A., McNamara B. R., Forman W., Jones C., Quintana H., Hornstrup A., 1998, *ApJ*, 502, 558
 White M., van Waerbeke L., M. Jonathan., 2005, *ApJ*, 575, 640
 Willis J. P. et al. 2005, *MNRAS*, 363, 675
 Wittman D., Dell’Antonio I. P., Hughes J. P., Margoniner V. E., Tyson J. A., Cohen J. G., Norman D., (2001) *ApJ*, 643, 128
 Wittman D., Tyson J. A., Margoniner V. E., Cohen J. G., Dell’Antonio I. P., (2006) *ApJ*, 557, 89
 Wright, C. O., Brainerd, T. G., 2000, *ApJ*, 534, 34

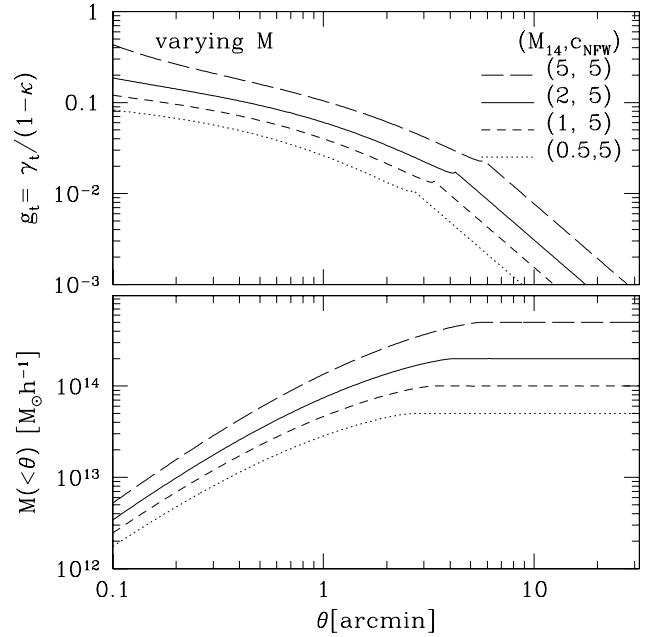


Fig. 6. The top panel shows the reduced shear profile of a truncated NFW model, for different virial masses ($5\times$, $2\times$, $1\times$ and $0.5\times 10^{14} M_{\odot} h^{-1}$ from upper to lower). The bottom panel shows the projected mass within an aperture θ . In all cases, the concentration parameter is $c_{\text{NFW}} = 5$, and the lens and source redshifts are $z_l = 0.4$ and $z_s = 1$ (a single source plane approximation is employed).

Appendix 1. Weak lensing properties of the truncated NFW model

Here, we present the reduced shear profile of a truncated NFW model (§5.4.1), to illustrate the dependence on model parameters. In Figure 6 and 7, we plot the reduced shear (upper panel) and the projected mass within an aperture θ (lower panel) for various values of the model

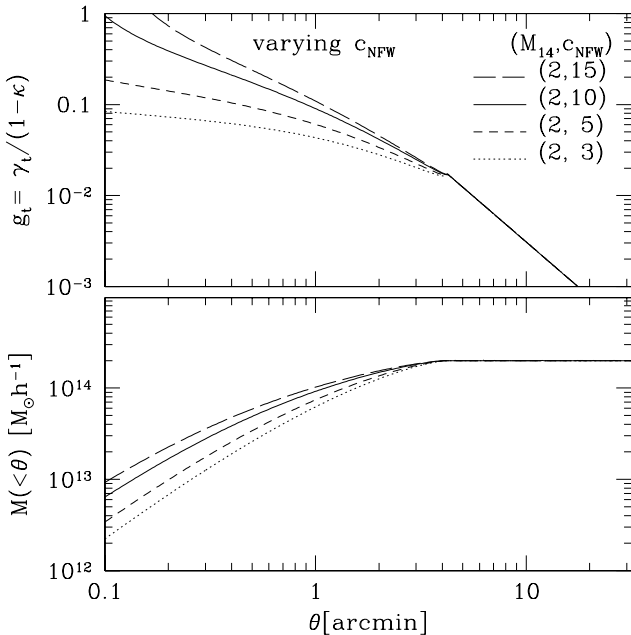


Fig. 7. Same as Fig 6 but for different concentration parameters ($c_{\text{NFW}} = 15, 10, 5$ and 3 , from upper to lower). In all cases, the virial mass $M_{\text{vir}} = 5 \times 10^{14} M_{\odot} h^{-1}$.

parameters M_{vir} and c_{NFW} . Since we adopt the truncated model (eq. (10)), κ becomes zero outside the virial radius, so the aperture mass flattens and the reduced shear (where $g = \gamma$) scales as $\propto \theta^{-2}$.

As shown in the Figure 6, changes in M_{vir} alter the amplitude of the shear profile, but leave the overall shape almost unchanged. The slight discontinuity at the virial radius in the reduced shear profile is a numerical artifact caused by the discontinuity there in κ . Figure 7 illustrates that changes in the concentration parameter alter the slope of the shear profile, but not the amplitude at the virial radius. The higher the concentration, the steeper the slope becomes, as expected.

In principle, a measurement of the weak lensing shear profile over a broad angular range therefore allows simultaneous constraints on both the cluster mass and the concentration parameter (i.e. the mass would be determined mainly by the shear amplitude near the virial radius, and the concentration parameter by the slope at $\theta < \theta_{\text{vir}}$). However, in our case, the angular range over which tangential shear is measured with a good S/N is rather narrow (typically $1 < \theta < 4$ arcmin). This especially prevents us from obtaining a tight constraint on the concentration parameter, which requires measurements over a broad angular range. Instead of treating both the virial mass and the concentration parameter as free parameters, we therefore decided to adopt an empirically observed relation between the concentration parameter and mass, eq. (11).

Appendix 2. Properties of individual targets

Here, we describe each target’s weak lensing and optical properties, and discuss the full results of the MOS observations. Quantitative summaries of these data are found

in Tables 1, 2 and 3.

Figures 8-43 also present the data, in a uniform format for easy visual comparison. Each figure is laid out as follows. The top-left panel shows an optical image of the cluster core, overlaid with contours reproducing the weak lensing density. The contours start from $\kappa = 0.04$ and increase in increments of $\Delta\kappa = 0.01$. Galaxies with successfully measured redshifts are marked with circles, their target ID and their redshift (in parentheses). The colors correspond to the galaxies’ observed spectral types. The top-right panel shows the positions of those galaxies in cone diagrams. The horizontal axis corresponds to radial comoving distance, and the vertical axes to a sky direction, with x and y standing for R.A. and Dec. respectively. The bottom-left panel reproduces the weak lensing density map on a larger scale, to show any nearby structure. Overlaid on the gray scale map are red contours, starting from $\kappa = 0.04$ and increasing in increments of $\Delta\kappa = 0.02$. White contours show instead the smoothed number density of galaxies with $18 < R_C < 23$ ($18 < i' < 23$ for the COSMOS field), starting from $n_g = 10$ arcmin $^{-2}$ and in increments of $\Delta n_g = 2$ arcmin $^{-2}$. For candidates where a single, well-defined concentration of galaxies was found, the bottom-right panel shows the weak lensing tangential shear profile (upper plot) and aperture mass profile (lower plot). Black points with error bars show measured data. The dashed line shows the best-fit SIS model, and the solid line shows the best-fit NFW model, plotted up to the virial radius. The red diamond shows the virial mass of this best-fit NFW model.

A.2.1. SL J0217.3–0524

This is not listed in the P1 catalogue because the peak κ S/N does not exceed P1’s threshold. As observed in Figure 8, the weak lensing κ peak is well correlated with a galaxy over-density. In the redshift data, there exists one galaxy concentration that passes our cluster criteria, with 8 members at $z_c = 0.43$. There is also a small concentration at $z = 0.31$. The velocity dispersion of the galaxy cluster is consistent with the SIS velocity dispersion. The NFW cluster mass agrees with the aperture mass at the corresponding virial radius. However, the aperture mass keeps increasing even outside of the expected virial radius. This is likely due to the mass associated with two κ over-densities located a few arcminutes to the west and the north-east of the cluster center.

A.2.2. SL J0217.6–0530

This is not listed in the P1 catalogue because the peak κ S/N is below the threshold. The weak lensing density peak appears isolated and is correlated with a galaxy over-density. In the redshift data, there is no galaxy concentration passing our criterion of five galaxies within a velocity of ± 3000 km/s, but there is a small group of three galaxies at $z = 0.43$. With only this information, it is currently not clear whether the weak lensing shear signal comes solely from the halo of the small galaxy concentration or whether there are other mass concentrations along the same line-of-sight. Since no galaxy concentration that

passes our cluster criterion was found, no weak lensing mass estimation or radial profiles are displayed.

A.2.3. *SL J0217.9–0452*

This is not listed in the P1 catalogue because the peak κ S/N is below the threshold. The weak lensing κ map shows a bimodal feature, with a second peak located at 2 arcminutes to the west of the main peak. There is a galaxy over-density near the main peak. No galaxy concentration in the redshift data is sufficiently rich to qualify as a cluster under our criterion, but there is a small group of four galaxies at $z = 0.19$. With only the current information, it is not clear whether the weak lensing shear signal comes from the halo of the small galaxy concentration alone or from additional concentrations along the same or an adjacent line-of-sight. Since no galaxy concentration passing our cluster criterion was found, we did not make the weak lensing mass estimation.

A.2.4. *SL J0218.0–0444*

This is not listed in the P1 catalogue because the peak κ S/N does not exceed P1's threshold. The weak lensing density distribution is elongated along the south-east to north-west direction. There is a galaxy over-density overlapping with the weak lensing κ peak but elongated perpendicular to this. In the redshift data, no galaxy concentration passes our cluster criterion, but there are two small concentrations at $z = 0.37$ (five galaxies) and at $z = 0.31$ (four galaxies). Since no dominant galaxy concentration was found, we have not estimated a weak lensing mass. Note that in the vicinity of this target there is a known galaxy cluster, identified in optical-near infrared imaging and with an estimated photometric redshift of $z_p = 0.71 \pm 0.03$ (van Breukelen et al. 2006, their ID 5, R.A. = 34.50, Dec. = -4.72). This cluster is located 2 arcminutes to the north-west and is within the elongated over-density region. It is therefore likely that the κ excess consists of the chance projection of several halos located at different redshifts along adjacent lines-of-sight.

A.2.5. *SL J0219.6–0453*

This is not listed in the P1 catalogue because the peak κ S/N is below the threshold. As shown in Figure 12, the weak lensing κ peak is elongated in the east-west direction, with a smaller, secondary peak 3 arcminutes east of the cluster center. An extended galaxy over-density overlaps with both κ peaks. In the redshift data, a galaxy concentration with 11 members at $z_c = 0.33$ passes our cluster criterion. There is also a small concentration of three galaxies at $z = 0.3$. The measured velocity dispersion of the galaxy cluster is smaller than the SIS velocity dispersion, but within $1-\sigma$ error. The NFW cluster mass is slightly larger than the aperture mass at the corresponding virial radius. This could be due to a contaminated measurement of tangential shear. Looking more closely at the aperture mass profile shows a flattening at $\theta = 1 - 2$ arcmin, followed by a second subsequent increase at larger radii up to ~ 4 arcminutes. Mass associated with the secondary peak may account for that second rise.

A.2.6. *SL J0222.8–0416*

The weak lensing density distribution looks relaxed, and correlates well with the galaxy over-density. In the redshift data, one concentration of six galaxies lies $z_c = 0.32$ with 6 members that passes our cluster criterion. In addition, there are small concentrations at $z = 0.435$ (4 galaxies) and at $z = 0.227$ (3 galaxies). The velocity dispersion of the galaxy cluster is larger than the SIS velocity dispersion, though they are within $1-\sigma$ error. The NFW cluster mass agrees with the aperture mass at the corresponding virial radius. However, the aperture mass keeps increasing at outer radii of the expected virial radius. This is due to the mass associated with the structure located at about 4–8 arcminutes to the east–south from the cluster center where no associated galaxy excess is observed.

A.2.7. *SL J0224.4–0449*

This is a galaxy cluster previously identified by weak lensing shear (Cl-02 of Gavazzi & Soucail 2007). The redshift was photometrically estimated to be $z = 0.497$ (Gavazzi & Soucail 2007) but had not been spectroscopically obtained. The weak lensing density distribution is elongated in the north-south direction. The elongation of the galaxy distribution is less pronounced, but in the same direction. In the redshift data, there one strong concentration of ten, mainly absorption galaxies at $z_c = 0.49$. There may also be a small concentration at $z = 0.32$. The velocity dispersion of the galaxy cluster is found to be smaller than the SIS velocity dispersion. The reason for this discrepancy is not clear, but one possibility is the small number of member galaxies used for the estimation of the velocity dispersion. The NFW cluster mass agrees with the aperture mass at the corresponding virial radius. The aperture mass flattens at the scales larger than the virial radius and no substructure is observed in the weak lensing density map.

A.2.8. *SL J0224.5–0414*

The weak lensing density distribution shows irregular morphology, with a second peak about 3 arcminutes east of the first peak. There is an apparent galaxy over-density that largely overlaps with the first peak. In the redshift data, there is one strong galaxy concentration at $z_c = 0.26$ with 12 members, dominated by absorption galaxies. In addition, there is a small concentration at $z = 0.316$ (4 galaxies). The velocity dispersion of the galaxy cluster is smaller than the SIS velocity dispersion, though they are within $1-\sigma$ error. The NFW cluster mass agrees with the aperture mass at the corresponding virial radius. The aperture mass profile increases erratically at larger radii looks, probably reflecting contributions to the signal from nearby structures.

A.2.9. *SL J0225.3–0441*

This is a galaxy cluster previously identified by weak lensing shear (Cl-05 of Gavazzi & Soucail 2007). The photometric redshift was estimated to be $z = 0.269$ (Gavazzi & Soucail 2007) but a spectroscopic redshift had not

been obtained. The weak lensing density distribution is slightly elongated in the north-west to south-east direction, with an additional small extension to the north-east. Interestingly, the center of the galaxy over-density is at the position of the small extension, and a possible cD galaxy is also found there (target ID 1). At $z_c = 0.26$, there is a concentration of seven (mainly absorption) galaxies, including the possible cD galaxy. In addition, there are nearby concentrations of three galaxies at both $z = 0.21$ and $z = 0.46$. The velocity dispersion of the galaxy cluster is consistent with the best-fit SIS velocity dispersion parameter, and the NFW cluster mass is consistent with the aperture mass at the virial radius.

A.2.10. *SL J0225.4–0414*

This is a galaxy cluster previously identified by weak lensing shear (Cl-14 of Gavazzi & Soucail 2007). The photometric redshift was estimated to be $z = 0.153$ (Gavazzi & Soucail 2007) but a spectroscopic redshift had not been obtained. The weak lensing density distribution is slightly elongated in the north-south direction. Two additional peaks lie in the same direction: one 4 arcminutes to the north and another 7 arcminutes to the south. There is a filamentary-like structure connecting the three peaks. The northern clump was previously identified by weak lensing shear (Cl-04 of Gavazzi & Soucail 2007) but the spectroscopic redshift has not been obtained.

There are galaxy over-densities corresponding to (but slightly offset from) all the three weak lensing peaks. Interestingly, the galaxy over-density associated with the central peak is elongated in a perpendicular direction to the weak lensing density. In the redshift data, there is a concentration of eight absorption galaxies at $z_c = 0.14$. The velocity dispersion of the galaxy cluster is consistent with the SIS velocity dispersion. The tangential shear profile is not well fit by an NFW model, with an excess at large radii due to the surrounding structures observed in the weak lensing density map. Similarly, the aperture mass profile does not flatten at scales even as large as $\theta = 10$ arcminutes. The mass contribution from the surrounding structures may also account for this. It was therefore difficult to define the boundary of this galaxy cluster, in which to calculate the total mass.

A.2.11. *SL J0225.7–0312*

This cluster has one of the strongest weak lensing signals ($\kappa_{peak} = 0.114$) of our catalog. The weak lensing density distribution looks relaxed except for an extension to the north-east. The galaxy distribution correlates with the weak lensing density but is off-centered towards the extension. In the redshift data, there is an apparent galaxy concentration at $z_c = 0.14$, with 15 members dominated by absorption galaxies. The velocity dispersion of the galaxy cluster is in good agreement with the SIS velocity dispersion. The NFW cluster mass consistent with the aperture mass at the largest radius.

A.2.12. *SL J0228.1–0450*

This is a galaxy cluster previously identified by weak lensing shear (Cl-14 of Gavazzi & Soucail 2007). The photometric redshift was estimated to be $z = 0.292$ (Gavazzi & Soucail 2007) but no spectroscopic redshift had been obtained. We found a strong concentration of 13 absorption galaxies at $z = 0.29$. The weak lensing density distribution shows irregular morphology. The low-level feature to the south may be edge effects due to a bright star mask. However, a second cluster, 7 arcminutes ($16.5h^{-1}$ comoving Mpc) to the west and at the same redshift is real. This was listed as SL J0227.7–0450 in P1 and was first identified from XMM-Newton data by Pierre et al. (2006), where it was named XLSS J022739.9–045129 [also XLSSC022]. The weak lensing map shows a filamentary structure connecting the two clusters, which appear to form a super cluster system.

There is an apparent galaxy over-density that largely overlaps with the weak lensing high density region. There is a possible cD galaxy (the target ID 3, $z = 0.294$) slightly south-east of the weak lensing density peak. The velocity dispersion of the galaxy cluster is found to be smaller than the SIS velocity, though they are within $1-\sigma$ error. The NFW cluster mass agrees with the aperture mass. However, the boundary of the cluster is very uncertain because of the filament. The aperture mass profile does not show flattening at large scales of $\theta = 10$ arcminutes.

A.2.13. *SL J0850.5+4512*

This is a known cluster first identified from its galaxy overdensity (NSC J85029+451141, Gal et al. 2003), but no spectroscopic redshift had been obtained. The weak lensing density distribution looks relaxed. There is a possible associated substructure in the north-east from the cluster. The galaxy distribution agrees well with the weak lensing density map. Two possible cD galaxies (target IDs 1 and 31) are located very close to the weak lensing density peak. In the redshift data, there exists one strong galaxy concentration at $z_c = 0.19$ with 15 members dominated by the absorption galaxies. The velocity dispersion of the galaxy cluster is found to be in a good agreement with the SIS velocity dispersion. The NFW cluster mass agrees with the aperture mass.

A.2.14. *SL J1000.7+0137*

This is a known cluster first identified from its galaxy concentration (NSC J100047+013912, Gal et al. 2003), and later via X-ray emission by Finoguenov et al. (2006, their ID 67; the photometric redshift they obtained is $z = 0.22$) but the spectroscopic redshift had not been determined. The weak lensing density distribution shows irregular morphology. There is an over-density of galaxies, but its peak is about 2 arcminutes north of the weak lensing density peak. About 6 arcminutes east of the cluster center there is another weak lensing density peak, which is our target SL J1001.2+0135 described in §2.15. A smaller, third peak lies a similar distance to the east. In the redshift data, we find a strong galaxy

concentration at $z_c = 0.22$, with 14 members dominated by absorption galaxies. Note that we find galaxy cluster SL J1001.2+0135 at the same redshift. There are additional small concentrations of galaxies at $z = 0.34$ and $z = 0.52$. The separation between the two main clusters is $11h^{-1}$ comoving Mpc (at $z = 0.22$), and a filamentary structure connecting the two clusters is observed in the weak lensing density map. Thus it is likely that they form a super cluster system.

The velocity dispersion of the galaxy cluster is in a good agreement with the SIS velocity dispersion. The NFW cluster mass is slightly larger than the aperture mass. It is likely that the spherical NFW model does not give a good description of this cluster, because of asymmetry in the density distribution.

A.2.15. SL J1001.2+0135

This is not listed in the P1 catalogue because the peak κ S/N does not exceed the required threshold. Note that an extended X-ray source discovered by XMM-Newton (Finoguenov 2006, their ID 54; RA.=150.33413, Dec.=1.60301) lies about 3 arcminutes east of the weak lensing density peak, and a known optically selected cluster (Gal et al. 2003, NSC J100113+013335 R.A.=150.30812, Dec.=1.55967, $z_{p\text{hot}} = 0.242$). The weak lensing κ map appears elongated, with filamentary structure connecting this cluster to SL J0850.5+4512 (§2.14).

In the redshift data, there are two strong galaxy concentrations at $z = 0.22$ (11 members; we name it SL J1001.2+0135A) and $z = 0.37$ (11 members; we name it SL J1001.2+0135B). The velocity dispersions are $\sigma_{\text{sis}} \sim 1380\text{km/s}$ (A) and 930km/s (B). Since we do not have enough information to de-project the weak lensing density into two components (e.g., accurate photometric redshifts of faint galaxies, e.g. Massey et al. 2007), we are unable to separately estimate the weak lensing mass of each cluster.

A.2.16. SL J1002.9+0131

This is not listed in the P1 catalogue because the κ peak is located close to the field edge and thus outside the *secure survey area*. There is a galaxy over-density correlated with the weak lensing κ peak. In the redshift data, there is no galaxy concentration passing our cluster criterion, but there are two small concentrations at $z = 0.37$ (3 galaxies) and at $z = 0.66$ (3 galaxies). Since no galaxy concentration that passes our cluster criterion was found, we did not estimate the weak lensing mass.

Note that very near this target is a known X-ray cluster with the estimated photometric redshift of $z_p = 0.75$ (Finoguenov et al. 2006, their ID; R.A.=150.75121, Dec.=1.52793). Since the lensing efficiency of such a high redshift cluster is low (see Figure 3 of Hamana et al. 2004), it is unlikely to be solely responsible for the κ peak. Therefore one possible explanation of the observed κ excess is a chance projection of several halos located at different redshifts in adjacent lines-of-sight.

A.2.17. SL J1047.3+5700

The weak lensing density distribution is elongated in the north-west to south-east direction. The galaxy over-density correlates with the κ map very well. However, the redshift information reveals that the weak lensing and galaxy over-densities arise from not one but two clusters, located at different redshifts along the same line-of-sight. The foreground cluster is at $z = 0.24$ with 6 members ($\sigma_v = 412\text{km/s}$); the background cluster is at $z = 0.30$ with 10 members ($\sigma_v = 619\text{km/s}$). We call these SL J1047.3+5700A and SL J1047.3+5700B respectively. Since we do not have enough information to de-project the weak lensing density into two components (e.g., accurate photometric redshifts of faint galaxies, e.g., Massey et al 2007), we can not make separate mass estimates.

A.2.18. SL J1048.1+5730

The weak lensing density distribution is slightly elongated. There is a separate weak lensing density peak about 3 arcminutes south-east of the cluster center, which was not listed in the P1 catalogue because its κ S/N (as opposed to the illustrated κ) is lower than the required threshold. There is a galaxy over-density that largely overlaps with the κ peak. The redshift data contains one strong galaxy concentration at $z_c = 0.31$, with 9 members of mainly absorption type. There is also a small concentration at $z = 0.36$. The velocity dispersion of the galaxy cluster is found to be smaller than the SIS velocity dispersion, but within $1-\sigma$ error. The aperture mass profile shows a jump at $\theta \simeq 3.3$ arcminutes, probably due to the south-east peak. The NFW cluster mass agrees with the aperture mass within $\theta < 3$ arcmin.

A.2.19. SL J1049.4+5655

The weak lensing density distribution is elongated from the north-east to the south-west, with a second peak about 3 arcminutes north-east of the cluster center. The distribution of galaxies is more isotropic. In the redshift data, there is one galaxy concentration at $z_c = 0.42$ (6 members) that passes our cluster criterion, plus small groups at $z = 0.24$ (4 galaxies), $z = 0.31$ (4 galaxies) and possibly $z = 0.59$ (3 galaxies). The velocity dispersion of the galaxies is smaller than the best-fit SIS velocity dispersion. This discrepancy is probably due to a combination of line-of-sight projections and the small number of redshifts used to compute σ_v .

A.2.20. SL J1051.5+5646

The weak lensing density distribution is slightly elongated, and there is a second peak (catalogued as SL J1051.6+5647) 4 arcminutes to the north-east, for which we have not obtained galaxy spectra. There is no galaxy concentration sufficiently rich to fulfill our cluster criterion in the redshift data, but two small groups lie at $z = 0.33$ and $z = 0.35$. Note that galaxies with target IDs 2, 3 and 5 are found to be very nearby. Also note that the bright galaxy located at the peak of the κ map (SDSS SpecObjID 255522745545129984) is a nearby galaxy at

$z = 0.047$, and a second bright galaxy at R.A.=162.87, Dec.=56.82 (SDSS SpecObjID 267344926176444416) is also at $z = 0.46$. Since no galaxy concentration passing our cluster criterion was found, we did not make estimate a weak lensing mass.

A.2.21. SL J1052.0+5659

This is not listed in the P1 catalogue because its peak κ S/N is below the required threshold. The weak lensing density distribution looks well relaxed. A galaxy over-density is present but its peak is off-center, about 2 arcmin south of the κ peak. In the redshift data, there is no galaxy concentration passing our cluster criterion, but there are two small concentrations at $z = 0.34$ (4 galaxies) and $z = 0.52$ (4 galaxies). Since no rich galaxy concentration was found, we did not make the weak lensing mass estimation.

A.2.22. SL J1052.5+5731

This is not listed in the P1 catalogue because its κ S/N is below the required threshold. The weak lensing density distribution shows irregular morphology. A projected galaxy over-density overlaps with the κ peak but, in the redshift data, there is no galaxy concentration passing our cluster criterion. There are two small concentrations around $z = 0.34$ (5 galaxies) and $z = 0.61$ (3 galaxies). Since no dominant galaxy concentration was found, we did not calculate the weak lensing mass.

Note that this region also contains two X-ray cluster candidates (Kolokotronis et al. 2006): SEXCLAS-12 (R.A.=163.159, Dec.=57.514, at photometric redshift $z_p = 0.61$) and SEXCLAS-13 (R.A.=163.226, Dec.=57.536; $z_p = 0.58$). The sky position of SEXCLAS-12 is very close to the κ peak (~ 1 arcmin) and its estimated photometric redshift is very similar to the redshift of our small galaxy concentration. It is therefore likely that the galaxy concentration at $z = 0.61$ is the optical counter part of X-ray cluster candidate SEXCLAS-12 (Kolokotronis et al. 2006). The observed κ peak appears to consist of a chance projection of halos of galaxy clusters at different redshifts.

A.2.23. SL J1057.5+5759

The weak lensing density distribution looks relaxed, and is coincident with a very prominent overdensity of galaxies. 18 (mainly absorption) galaxies are found at $z_c = 0.60$. Their velocity dispersion is larger than the velocity dispersion parameter of the best-fit SIS model, but within $1\text{-}\sigma$ error. The NFW cluster mass agrees with the aperture mass at the corresponding virial radius. The aperture mass does not flatten at large radii. The reason for this is not currently clear, although the measurements beyond 5 arcminutes are noisy because the cluster is near the edge of a field.

A.2.24. SL J1135.6+3009

The weak lensing density distribution looks well isolated but with an extension to the north. A prominent over-density of bright galaxies includes a cD galaxy precisely at the κ peak position. The redshift data reveals a con-

centration of 15 (mainly absorption) galaxies at $z_c = 0.21$. The velocity dispersion of the galaxy cluster is consistent with the best-fit SIS parameter and the NFW cluster mass is consistent with the aperture mass.

A.2.25. SL J1201.7-0331

The weak lensing density distribution appears relaxed. There is a clear galaxy over-density which coincides with the κ peak. The redshift data contain a galaxy concentration at $z_c = 0.52$ with 8 members dominated by absorption galaxies. The velocity dispersion of the galaxy cluster is consistent with the SIS velocity dispersion. The NFW cluster mass is larger than the aperture mass at the corresponding virial radius. This small disagreement is likely due to poor measurements of the shear near the edge of a Subaru field. High S/N measurements are obtained only scales between $1 < \theta < 3.3$ arcmin.

A.2.26. SL J1204.4-0351

This is not listed in the P1 catalogue because the κ S/N is below that threshold. However, it is a known cluster, first identified by its extended X-ray emission (RX J1204.3-0350, Vikhlinin et al. 1998) and later confirmed with optical data (OC5 1204-0351, Donahue et al. 2002). The spectroscopic redshift of this cluster is $z = 0.261$ (Mullis et al. 2003).

The weak lensing density distribution shows irregular morphology. The galaxy over-density is clearly observed and its peak position is very close to the κ peak. A concentration of 14 galaxies is indeed seen at $z_c = 0.261$, dominated the absorption spectral types. Our measured velocity dispersion is consistent with the SIS velocity dispersion. The NFW cluster mass is slightly larger than the aperture mass at the corresponding virial radius. This small disagreement is likely due to the deviations from spherical symmetry apparent in the κ map. In this case, the NFW model would not be a good description of the cluster density distribution.

A.2.27. SL J1334.3+3728

This is a known cluster, first identified by galaxy counts (NSC J133424+372822, Gal et al. 2003), but a spectroscopic redshift has only been obtained for the cD galaxy (R.A.=203.60, Dec.=37.48, $z = 0.305$; SDSS SpecObjID 591610245776670720). This is located very close to the κ peak (R.A.=203.60, Dec.=37.48) whose redshift is $z = 0.305$ (SDSS, SpecObjID is 591610245776670720).

The weak lensing density distribution looks very irregular, with elongations to the north-west and south-east, as well as a neighbouring structure about 2 arcminutes north-east of the κ peak. However, the distribution of galaxies is centered neatly on only the main κ peak. The galaxy redshifts reveal 21 members of a cluster at $z_c = 0.30$, most of which are absorption galaxies. Upon further inspection, there is also a significant trend for southern (northern) galaxies to be at lower (higher) redshifts, which may imply an ongoing merger of two clusters. The measured velocity dispersion is larger than the best-fit SIS velocity dispersion parameter, but consistent within

1- σ error. The NFW cluster mass agrees with the aperture mass at the corresponding virial radius. However, the aperture mass profile does not flatten even at $\theta = 10$ arcminutes. This is probably due to mass of neighbour structures, and it is very difficult to define the boundary of the cluster.

A.2.28. SL J1335.7+3731

The weak lensing density distribution looks very irregular, with two distinct main peaks aligned in the east-west direction, and an additional structure between them extending towards the north. Only the central structure was listed in P1, as the S/N in κ (as opposed to the κ values shown) is below the required threshold. The galaxy over-density closely follows this elongated structure. A well-defined concentration of 14 galaxies is located at $z_c = 0.41$. Interestingly, more than half of these have emission or composite type spectra. There is also a small group of 3 galaxies at $z = 0.20$. The velocity dispersion of the galaxy cluster is in a reasonable agreement with the SIS velocity dispersion parameter. The NFW cluster mass is consistent with the aperture mass at the corresponding virial radius. However, it is unlikely that a spherical NFW model is a good description of this cluster, because of the asymmetry apparent in the weak lensing density map.

A.2.29. SL J1337.7+3800

The weak lensing density distribution looks relaxed. There is a galaxy over-density that coincides with the κ peak, including a cD galaxy very close to the center. In the redshift data, there is a prominent galaxy concentration at $z_c = 0.16$ with 16 members dominated by absorption galaxies. The velocity dispersion of the galaxy cluster is consistent with the SIS velocity dispersion. The NFW cluster mass is in a good agreement with the aperture mass at the corresponding virial radius.

A.2.30. SL J1601.6+4245

This is not listed in the P1 catalogue because the κ S/N is below the P1's threshold. The weak lensing density distribution looks relaxed, except for an additional filament extending to the north-west. A prominent over-density of galaxies coincides with the κ peak. This includes a cD galaxy at RA.=240.3934, Dec.=42.75902, whose spectrum was obtained by SDSS and was found to be $z = 0.208$ (SpecObjID 375714238640947200). Spectra of another two galaxies in this field were obtained by SDSS: SpecObjID=375714238619975680 at RA.=240.34840, Dec.=43.73718, $z = 0.208$ and SpecObjID=375714238666113024 at R.A.=240.45011, Dec.=42.79000, $z = 0.292$.

Our MOS observations in fact reveal a projection of several clusters at different redshifts along the same line-of-sight. A foreground cluster (SL J1601.6+4245A) is at $z = 0.208$, with 7 spectroscopically confirmed member galaxies, and a background cluster (SL J1601.6+4245B) at $z = 0.47$ with 8 members. We also find a small group of 5 new galaxies at $z = 0.29$. Therefore, SL J1601.6+4245A has 2+7 spectroscopically confirmed cluster members in-

cluding a cD galaxy, and the small galaxy concentration has 1+5 spectroscopic members. We therefore conclude that the observed κ excess is caused by the chance projection of at least three galaxy clusters located at different redshifts. Since we do not have enough information to de-project the weak lensing density into components, we can not compute their weak lensing masses.

A.2.31. SL J1602.8+4335

The weak lensing density distribution looks relaxed, with an additional low-level filamentary structure running from north to south. There is a galaxy over-density, including a cD galaxies, that coincides with the κ peak. In the redshift data, a strong concentration at $z_c = 0.42$ of 15 members is dominated by absorption galaxies. The velocity dispersion of the galaxy cluster is consistent with the SIS velocity dispersion. The NFW cluster mass is in a good agreement with the aperture mass at the corresponding virial radius. No conclusive explanation is found for the north-south filament.

A.2.32. SL J1605.4+4244

The weak lensing density distribution looks relaxed. There is a galaxy over-density that largely overlaps with the κ peak. In the redshift data, there exists one galaxy concentration at $z_c = 0.22$ with 6 members. The velocity dispersion is significantly larger than the SIS velocity dispersion, probably on account of the low number of observed member galaxies. The aperture mass profile behaves irregularly at larger radii. This may be noise due to a shortage of source galaxies, which are hidden by masks around nearby bright stars.

A.2.33. SL J1607.9+4338

This is not listed in the P1 catalogue because the κ S/N is below the P1 threshold. This is a known, optically selected cluster (GHO 1606+4346; Gunn, Hoessel, Oke, 1986), but no spectroscopic redshift had been obtained. The weak lensing density distribution appears elongated towards the north and south-west, with local κ maxima about 3 arcminutes from the target center in both directions. The south-west peak has the highest κ and is listed in the P1 catalogue (GTO 2deg² #04). A galaxy over-density overlaps the central and northern κ peaks. Our redshift data reveals a galaxy concentration at $z_c = 0.31$, passing our cluster criteria with 9 members. This is dominated by absorption galaxies. In addition, there is small concentration of five galaxies at $z = 0.25$. The velocity dispersion of the galaxy cluster is smaller than the SIS velocity dispersion. The reason for this is not clear but is probably due to poor statistics from the small number of spectroscopically confirmed cluster members. The NFW cluster mass is consistent with the aperture mass at the corresponding virial radius.

A.2.34. SL J1634.1+5639

The weak lensing density distribution looks relaxed. The clustering of bright galaxies is apparent, but the number density of galaxies with $18 < R_C < 23$ is lower than

the surrounding mean density. The redshift data reveals a single concentration of 13 galaxies at $z_c = 0.4$. The northern galaxies tend to have absorption spectra but, interestingly, the southern galaxies have emission spectra. The velocity dispersion of the galaxy cluster is significantly larger than the SIS velocity dispersion. As shown in Figure 1, the velocity distribution of spectroscopic members appears strongly skewed toward the bluer side. This skewness may account for the large measurement of dispersion. The reason of the large skewness is currently not clear: dynamical activity of the cluster may be involved, although there are poor statistics to constrain higher moments. The NFW cluster mass is in a good agreement with the aperture mass at the corresponding virial radius.

A.2.35. SL J1639.9+5708

The weak lensing density distribution is elongated in the north-south direction. The corresponding galaxy overdensity is clearly found. In the redshift data, there is no galaxy concentration passing our cluster criterion, but there are two small concentrations at $z = 0.2$ and $z = 0.63$. Since no sufficiently rich concentration of galaxies was found, we did not calculate the weak lensing mass.

A.2.35.1. SL J1647.7+3455

The weak lensing density distribution is elongated in the north-south direction. A prominent overdensity of bright galaxies includes one cluster of 12 galaxies at $z_c = 0.26$. This is dominated by absorption galaxies. There are small additional groups of galaxies at $z = 0.41$ and $z = 0.47$. The velocity dispersion of the main galaxy cluster is in a reasonable agreement with the SIS velocity dispersion. The NFW cluster mass is consistent with the aperture mass. However, the aperture mass profile does not flatten as expected at larger radii. This may be accounted for by the mass of a second cluster located about 6 arcminutes south-west of the cluster. It is also likely that the spherical NFW model does not accurately describe this cluster, as asymmetry is clearly visible in the weak lensing density map.

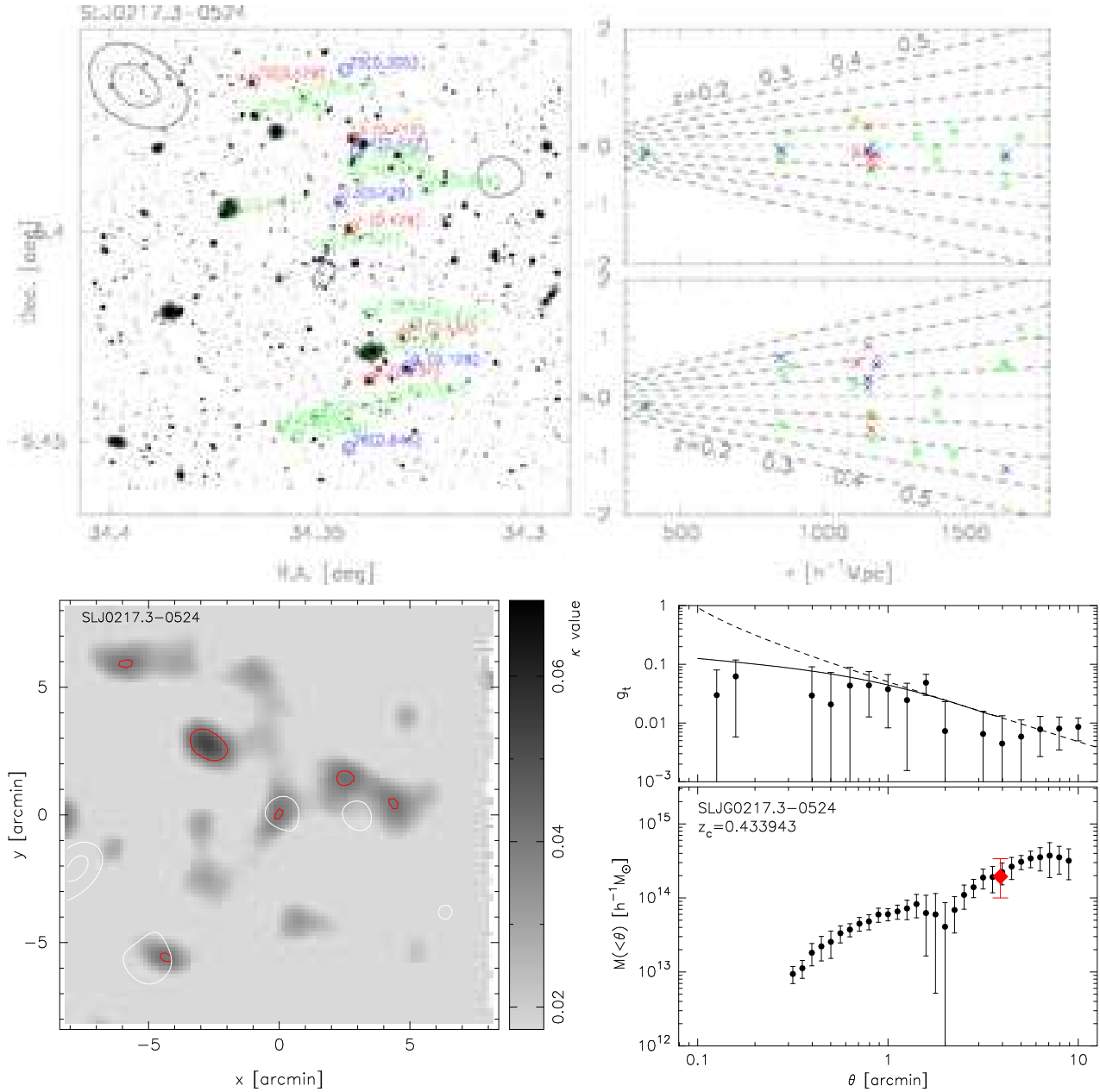


Fig. 8. SL J0217.3–0524: *Top-left panel:* R_C -band image with the weak lensing density overplotted as contours (starting from $\kappa = 0.04$ and in increments of $\Delta\kappa = 0.01$). Galaxies with measured redshifts are marked with circles, and labeled with their target ID and redshift (in parentheses). Red circles represent absorption galaxies, blue circles represent emission galaxies and green circles represent composite galaxies (see §3.3 and Cohen et al. 1999 for details). *Top-right panels:* Cone diagrams showing the 3D locations of galaxies. The horizontal axis shows the radial comoving distance. On the vertical axis, x and y correspond to the RA and Dec directions respectively. *Bottom-left panel:* The gray scale shows the weak lensing κ map (over an extended area), with red contours starting from $\kappa = 0.04$ and in increments of $\Delta\kappa = 0.02$. White contours show the smoothed number density of galaxies ($18 < mag < 23$), starting from $n_g = 10/\text{arcmin}^2$ and in increments of $2/\text{arcmin}^2$. *Bottom-right panel:* The measured weak lensing tangential shear profile $g_t = \gamma_t/(1 - \kappa)$, with the best-fit SIS model (dashed line) and NFW model (solid line, plotted up to the virial radius). The aperture mass profile $M(<\theta)$, computed from the tangential shear. The red diamond shows the virial mass of the best-fit NFW model.

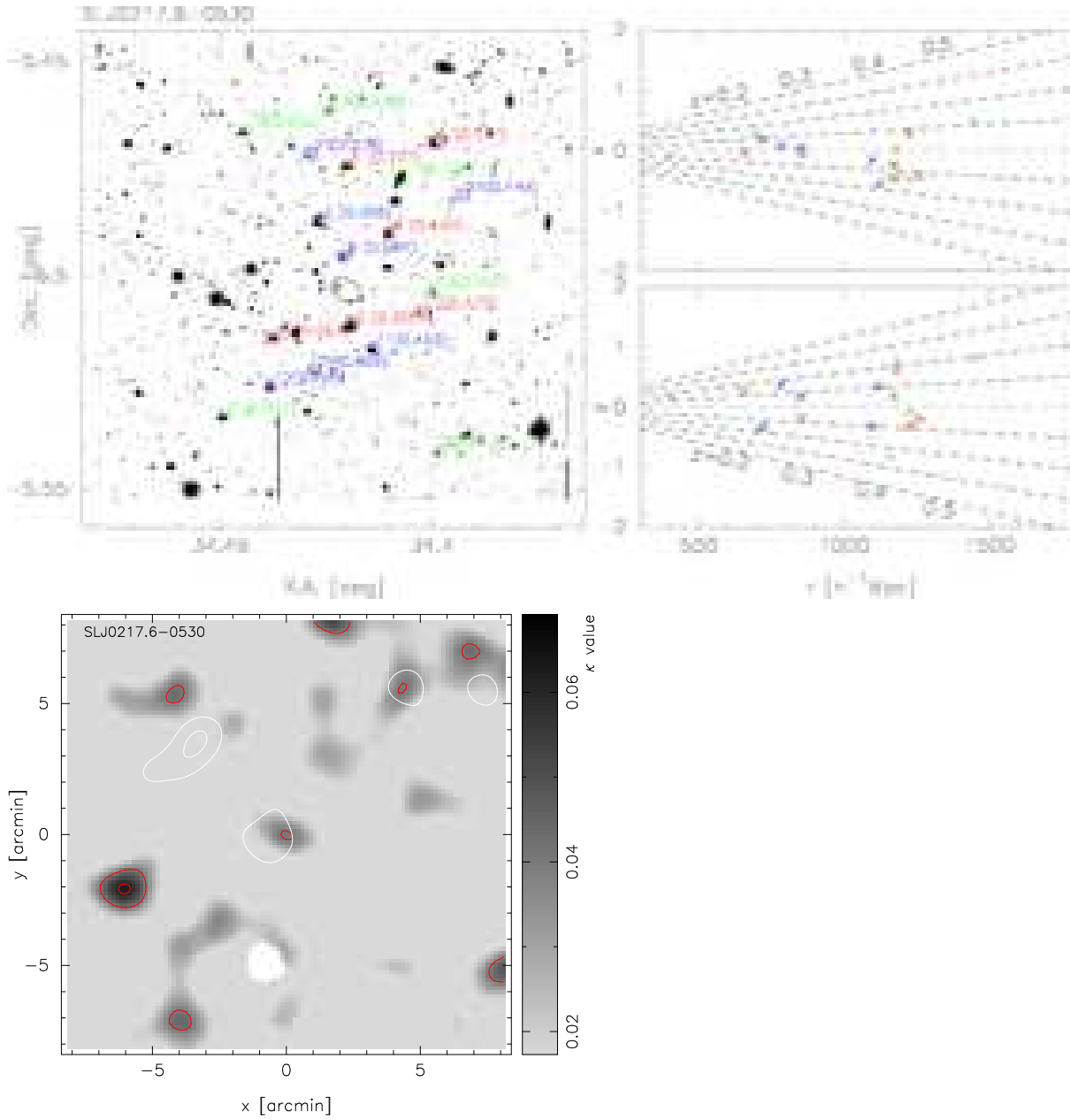


Fig. 9. Same as Figure 8 but for SL J0217.6–0530.

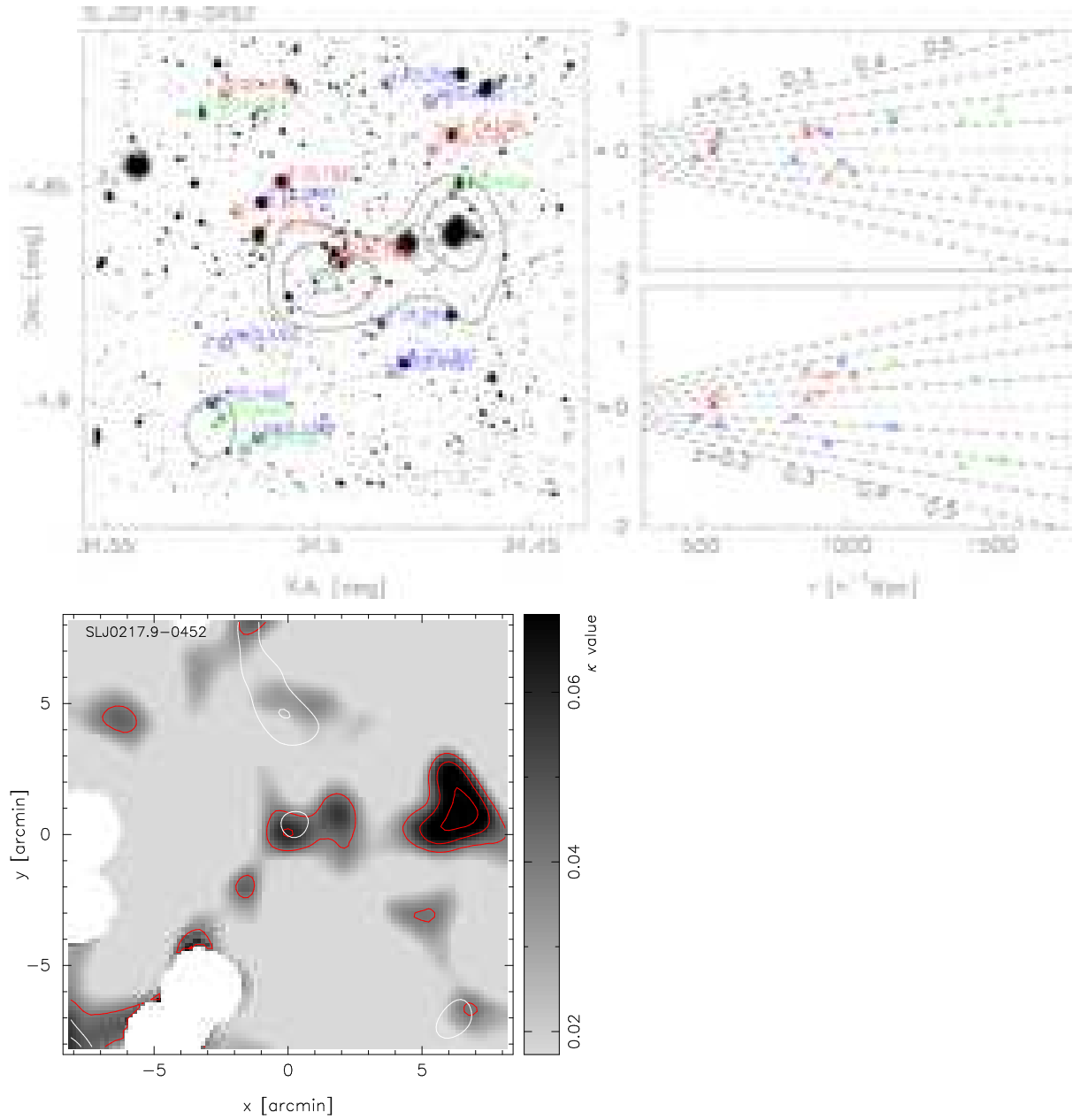


Fig. 10. Same as Figure 8 but for SL J0217.9–0452.

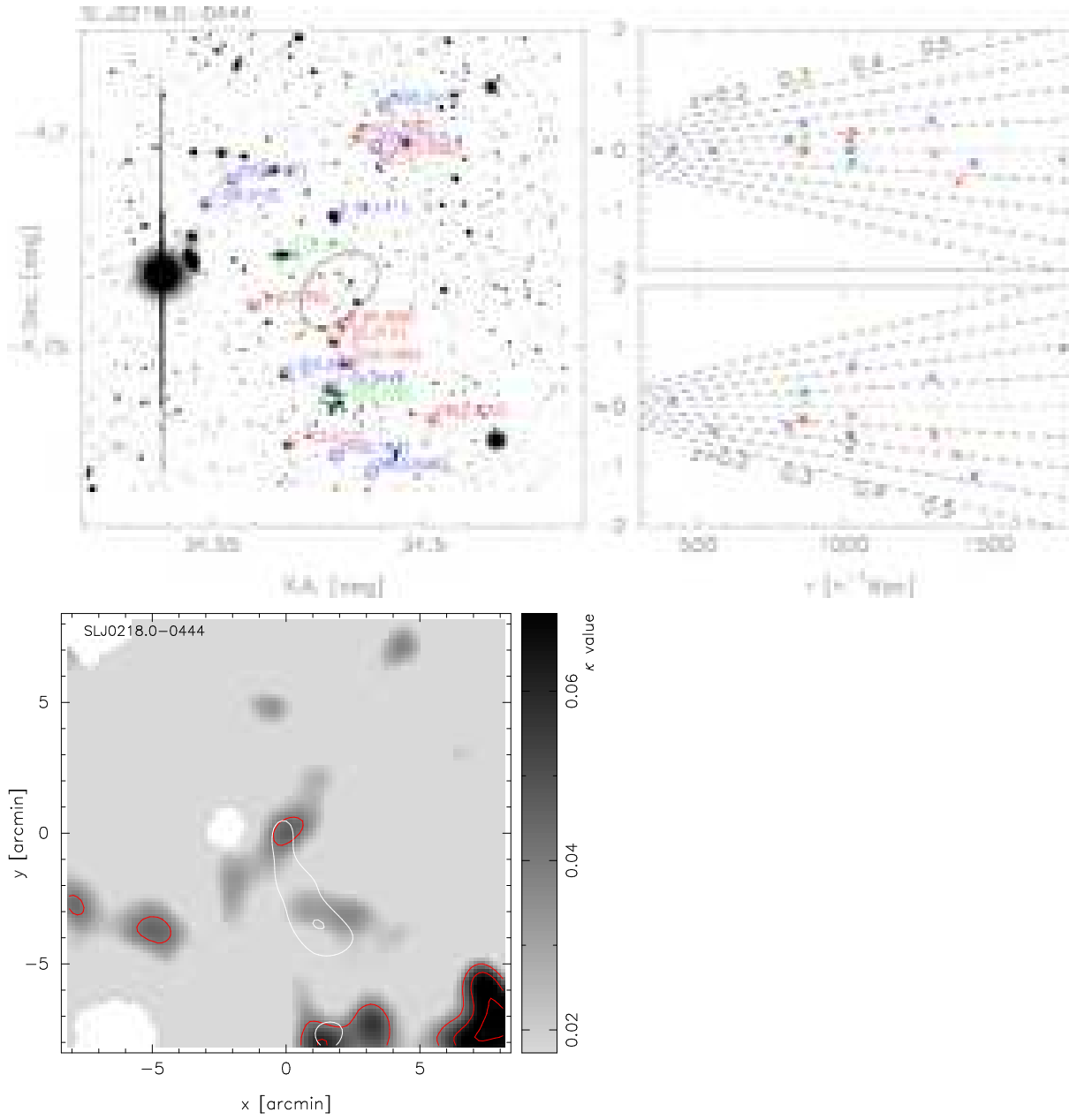


Fig. 11. Same as Figure 8 but for SL J0218.0-0444.

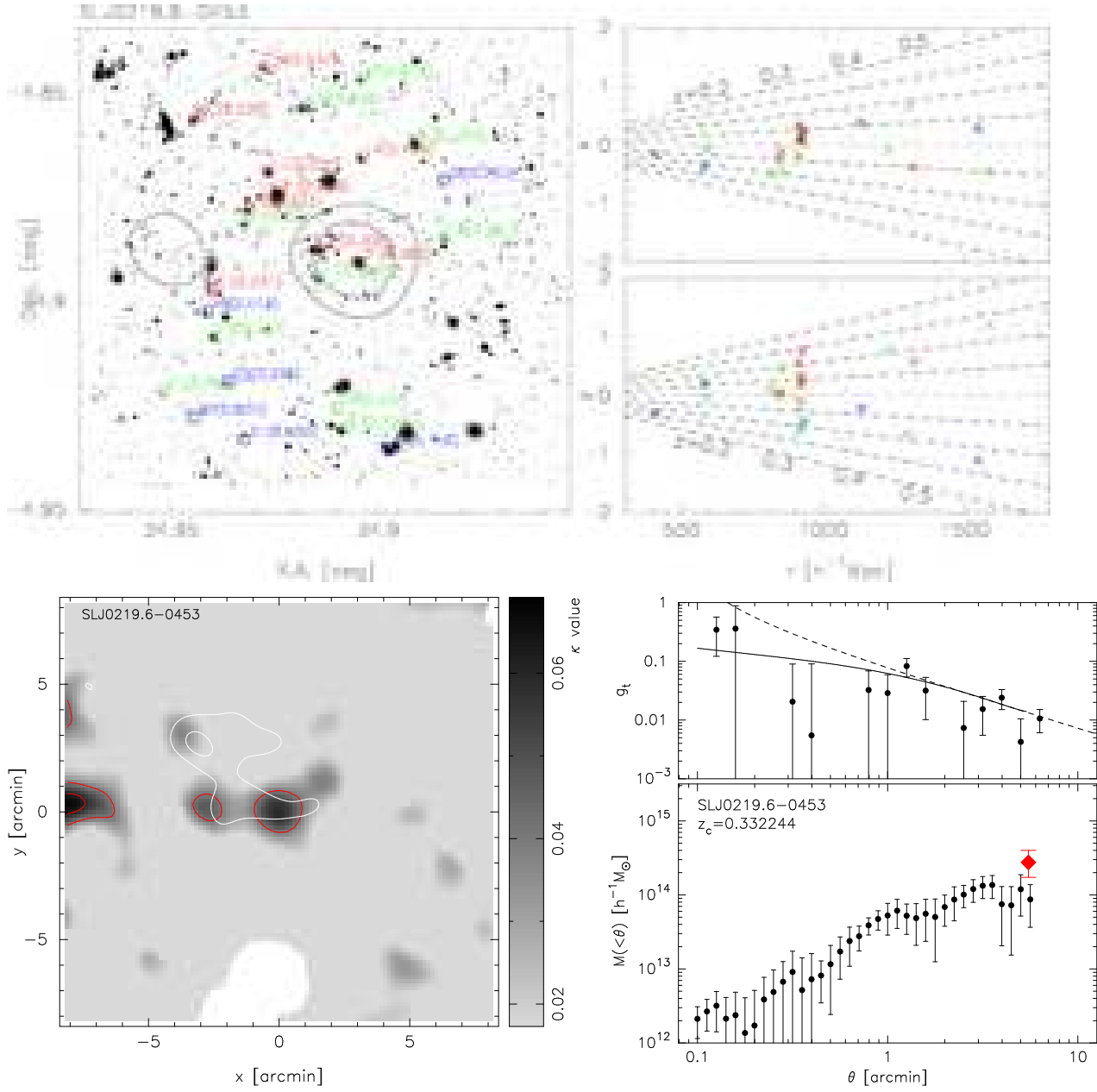


Fig. 12. Same as Figure 8 but for SL J0219.6-0453.

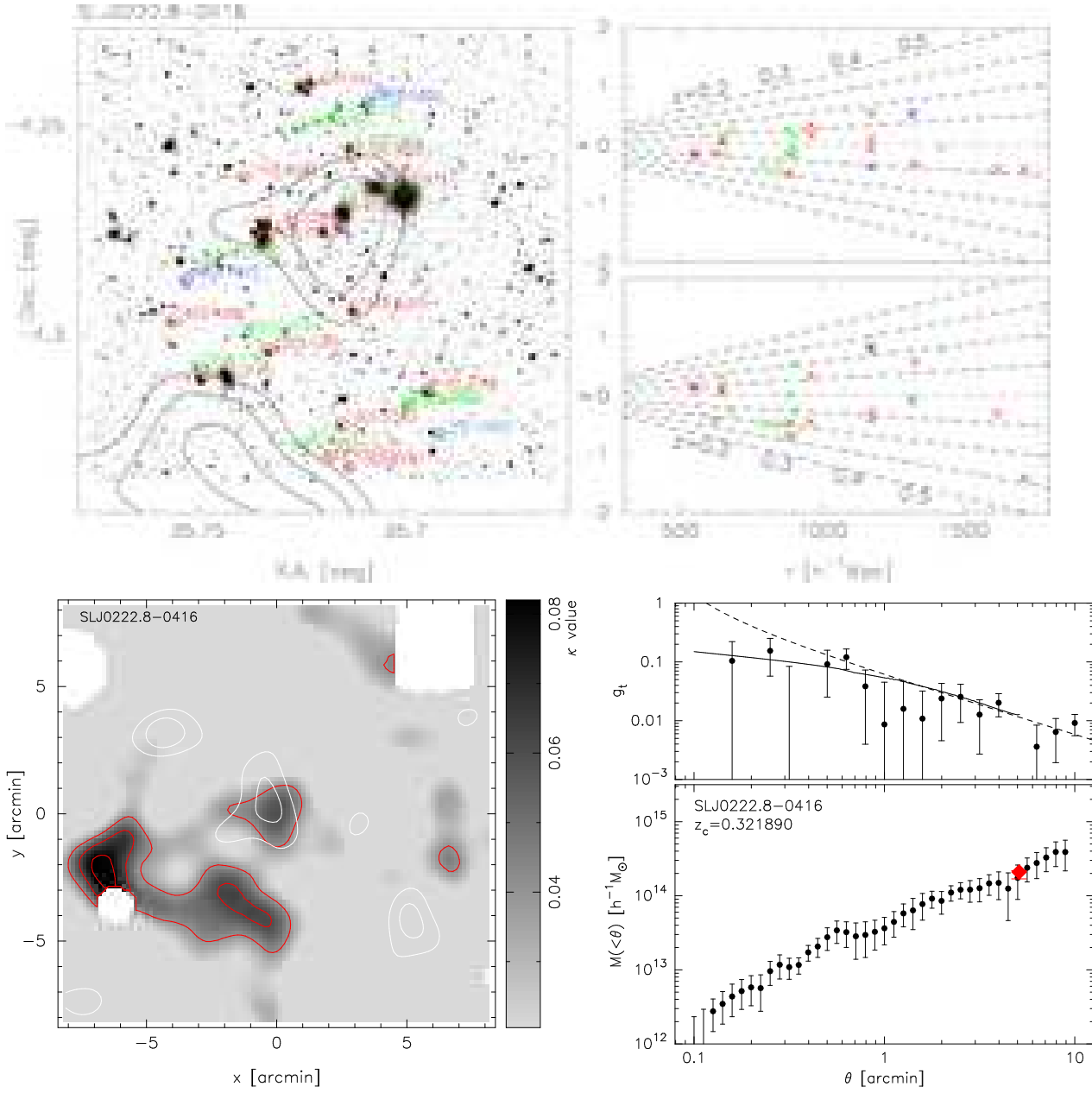


Fig. 13. Same as Figure 8 but for SL J0222.8-0416.

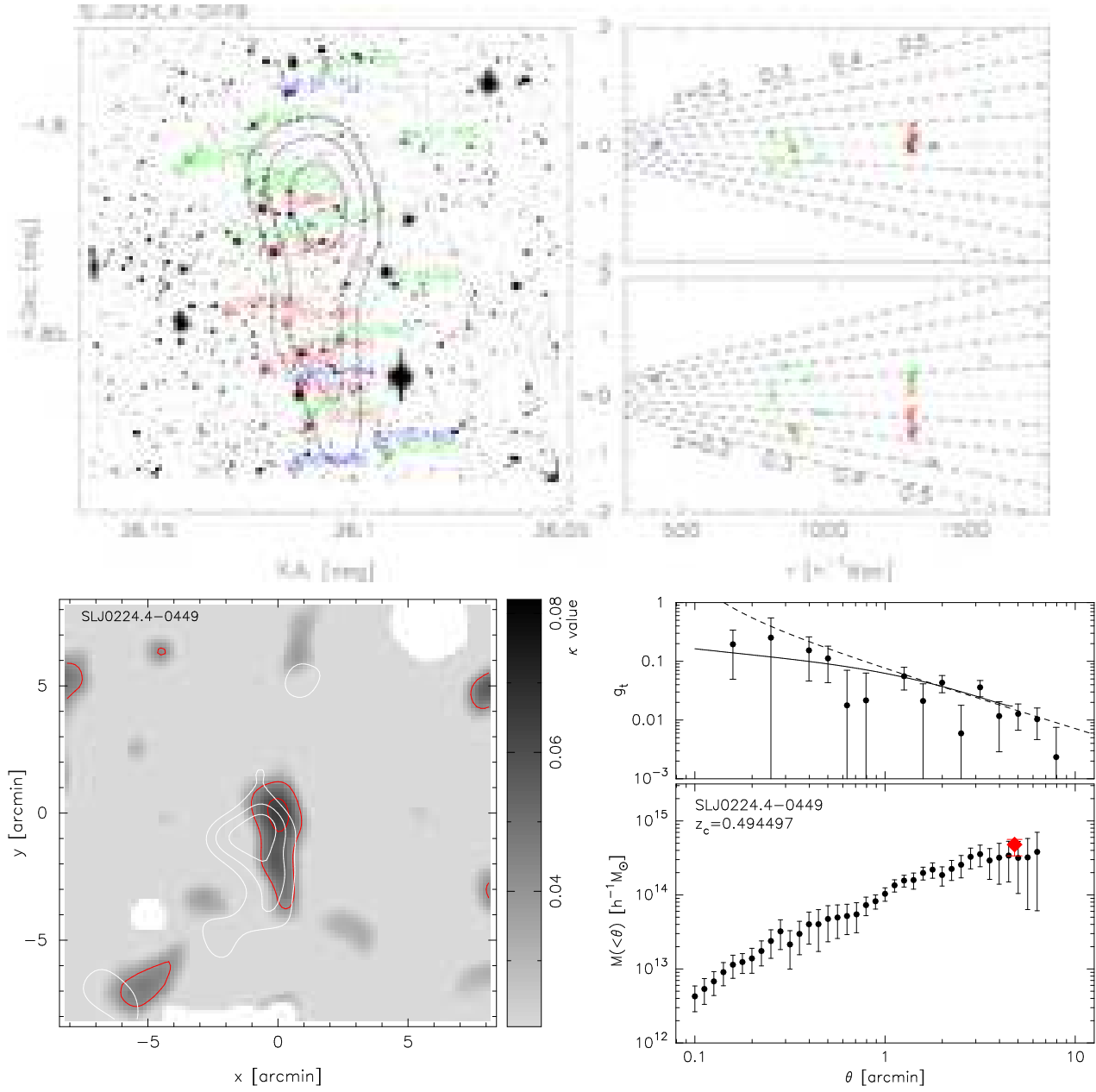


Fig. 14. Same as Figure 8 but for SL J0224.4-0449.

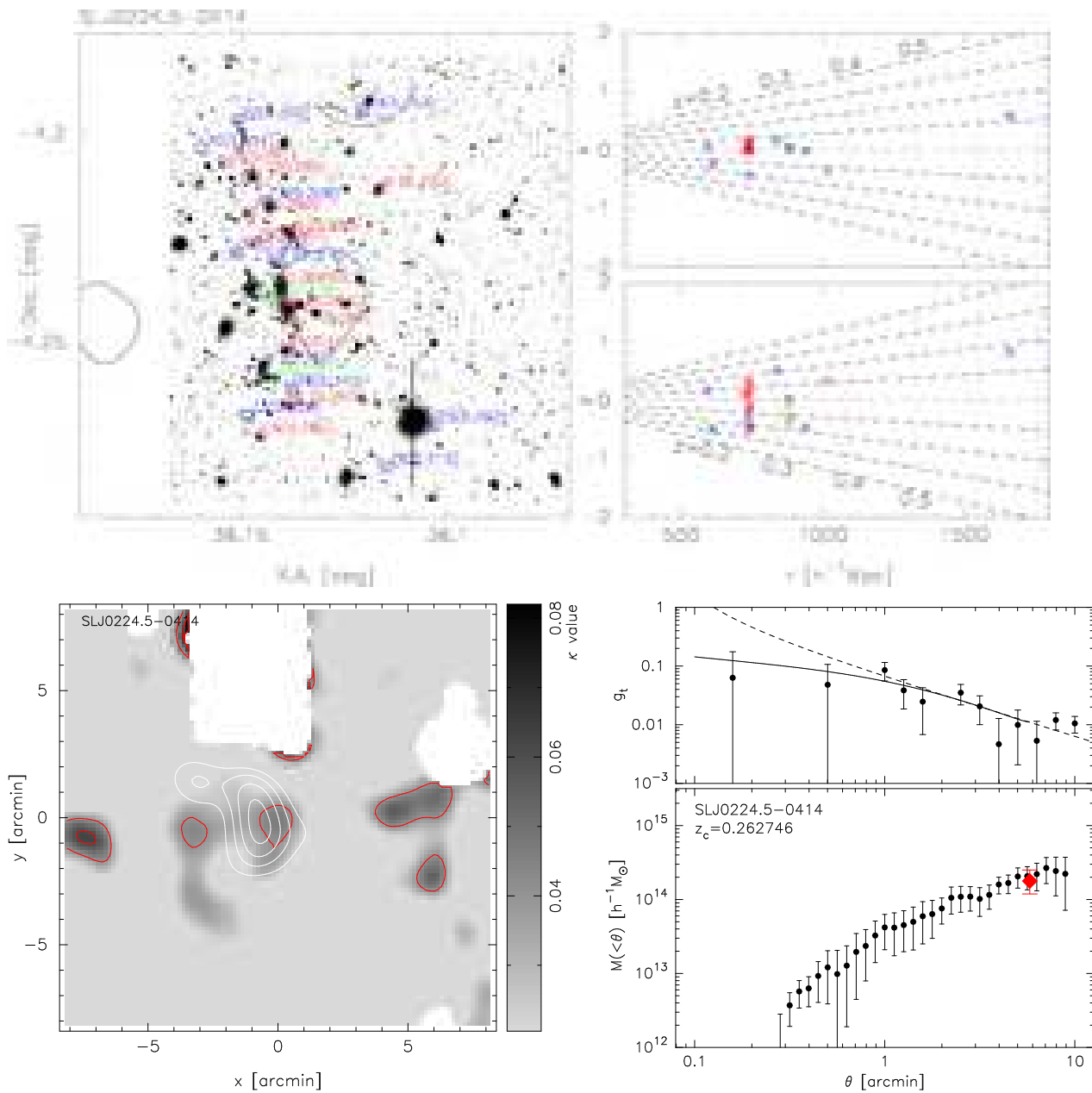


Fig. 15. Same as Figure 8 but for SL J0224.5–0414.

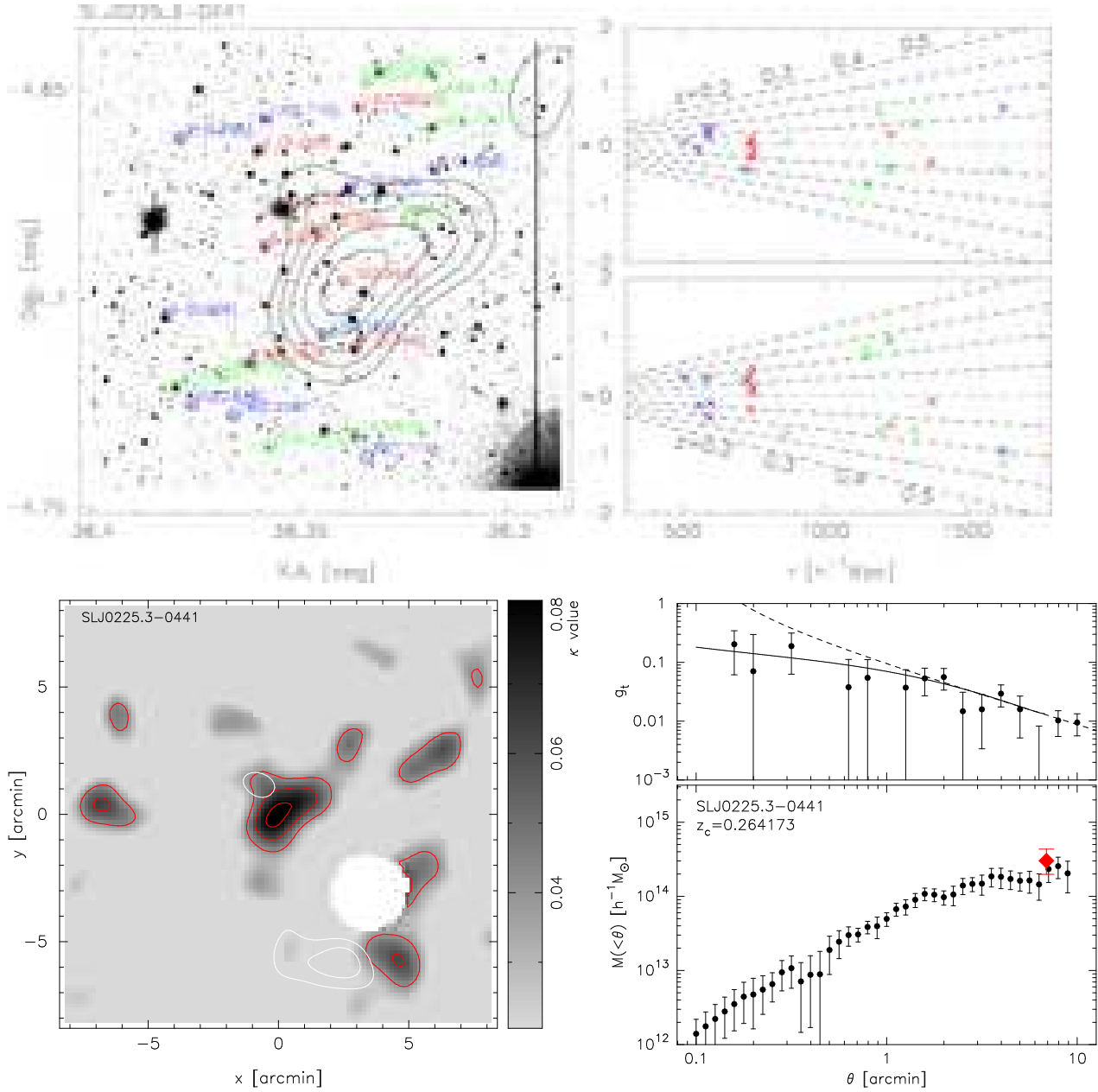


Fig. 16. Same as Figure 8 but for SL J0225.3-0441.

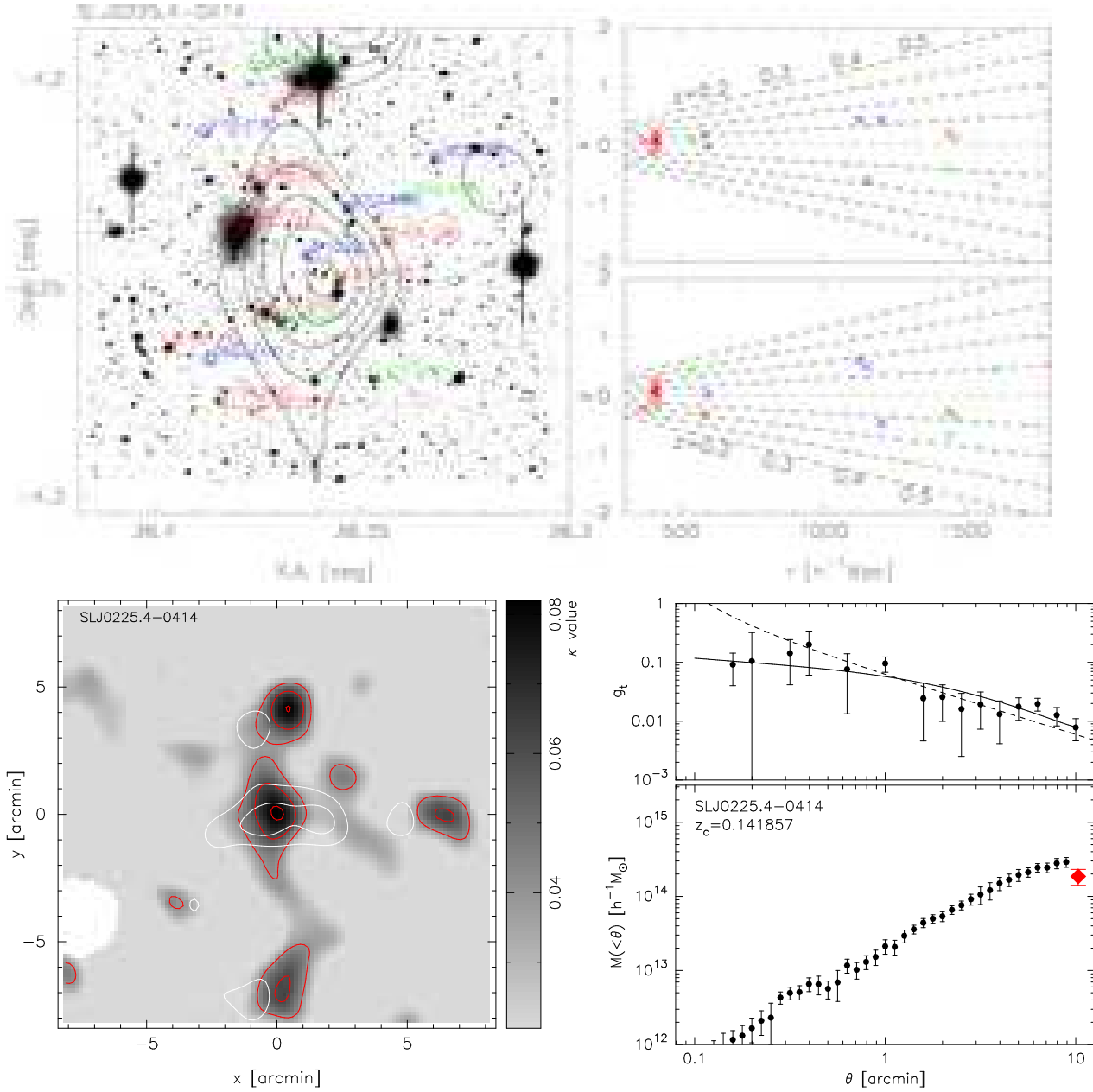


Fig. 17. Same as Figure 8 but for SL J0225.4–0414.

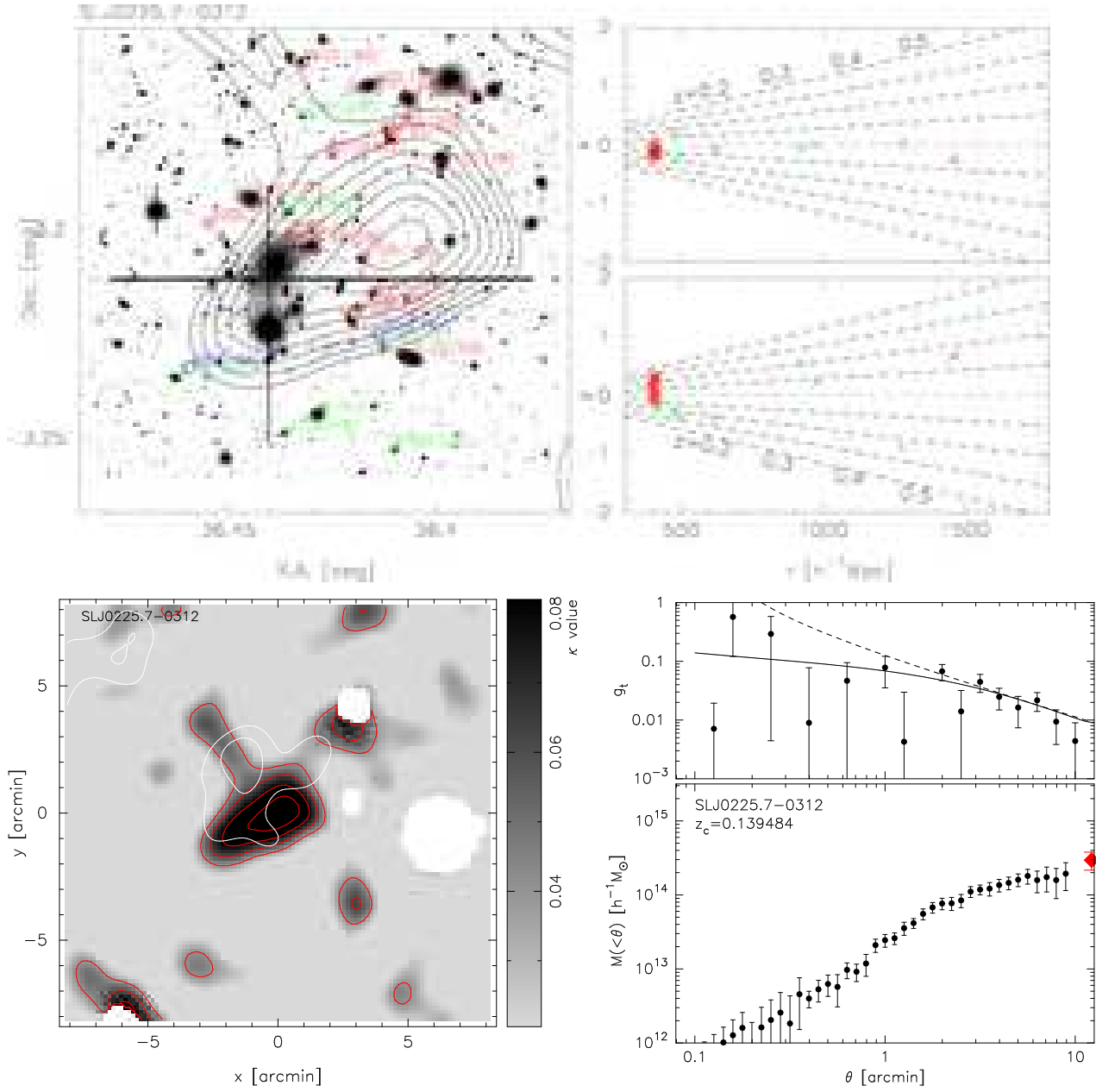


Fig. 18. Same as Figure 8 but for SL J0225.7–0312.

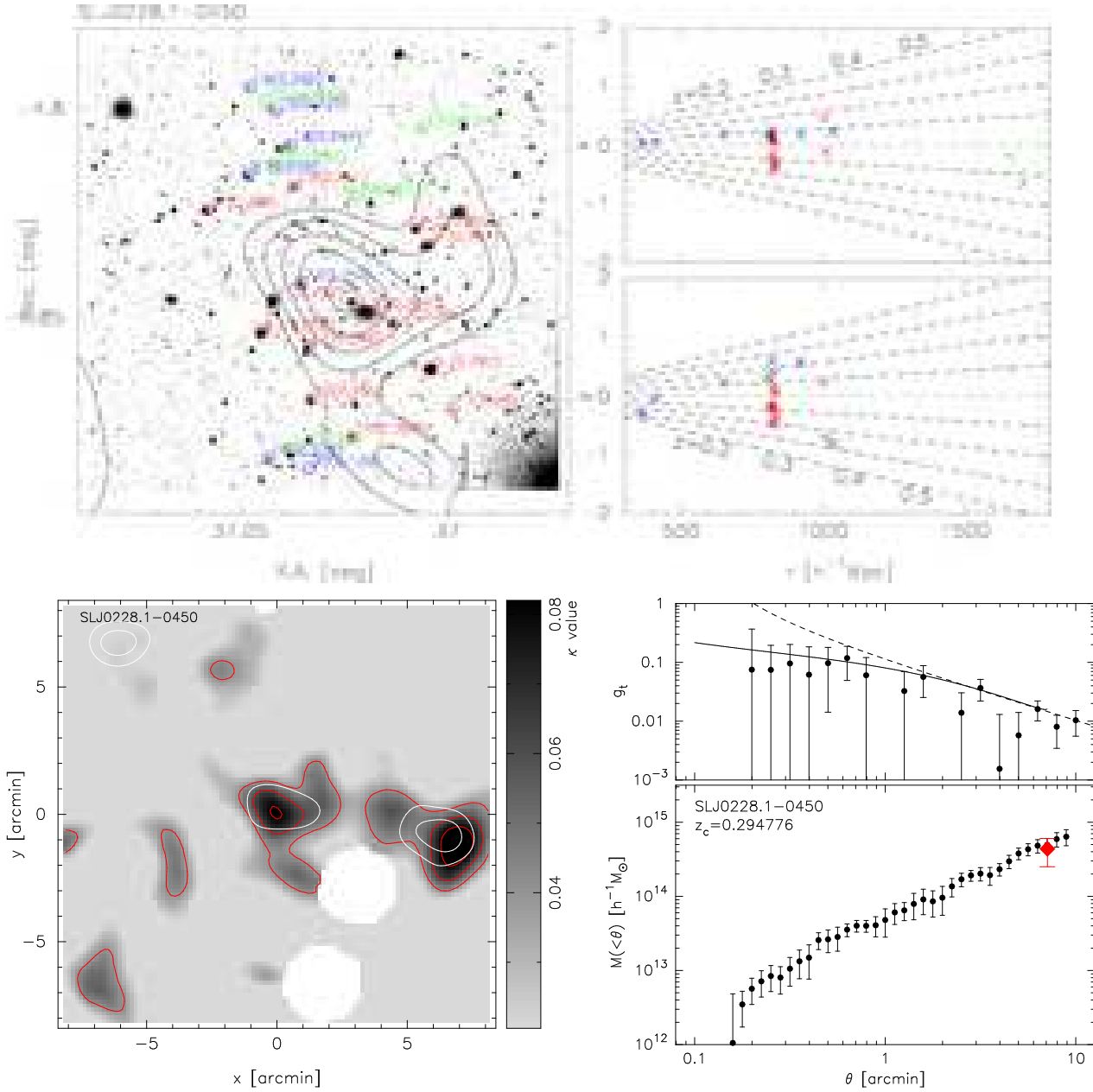


Fig. 19. Same as Figure 8 but for SL J0228.1-0450.

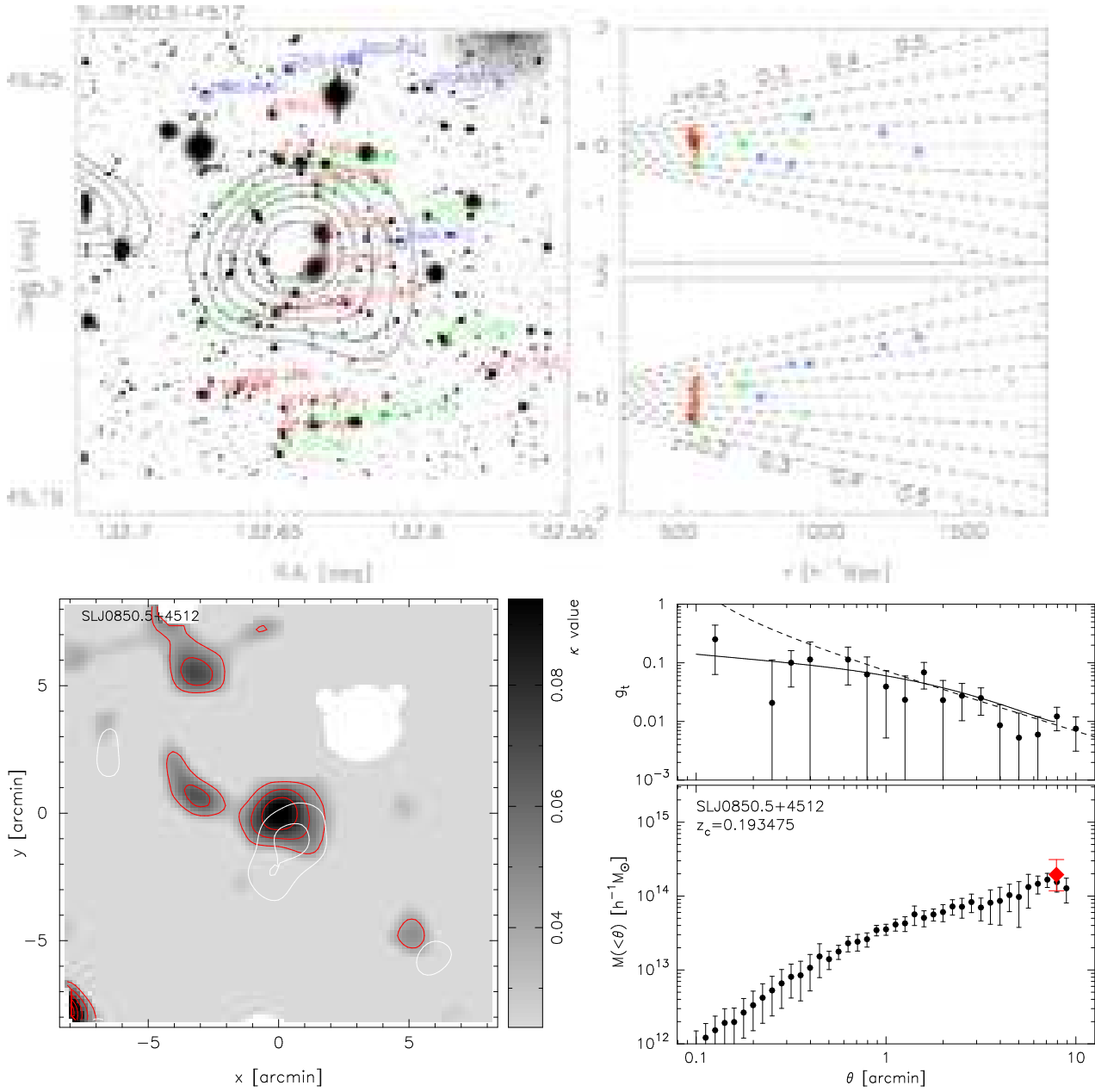


Fig. 20. Same as Figure 8 but for SL J0850.5+4512.

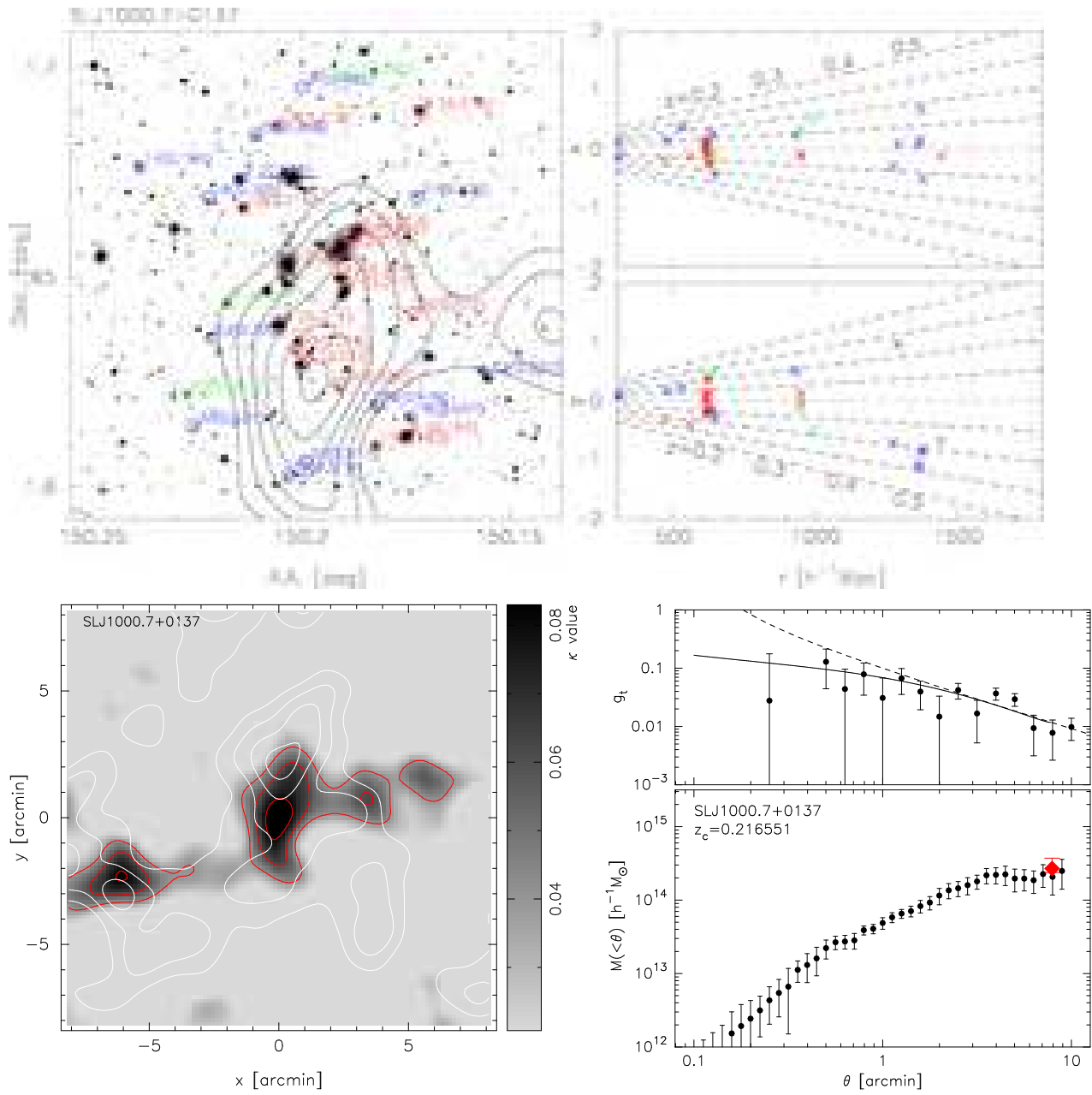


Fig. 21. Same as Figure 8 but for SL J1000.7+0137.

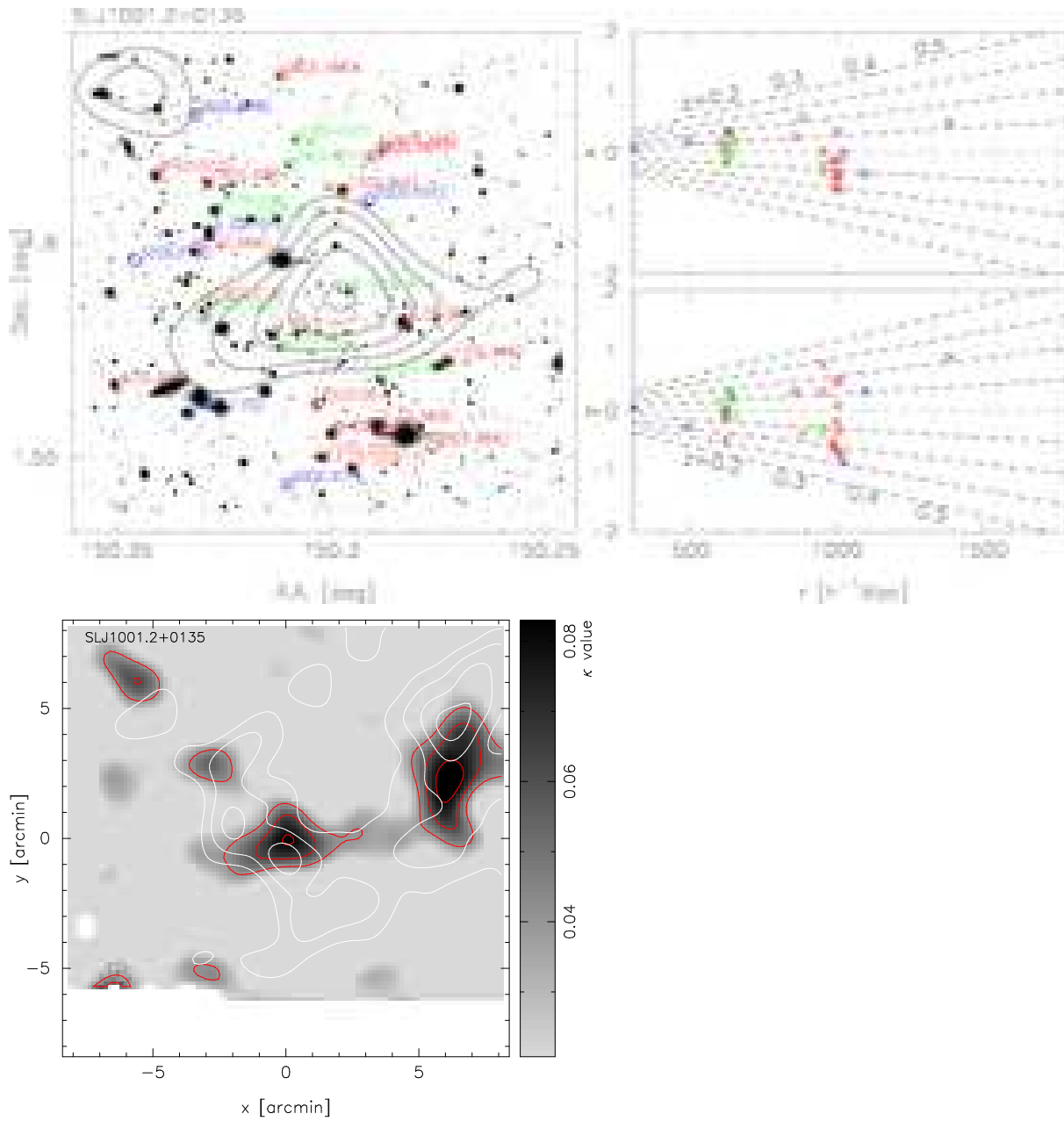


Fig. 22. Same as Figure 8 but for SL J1001.2+0135.

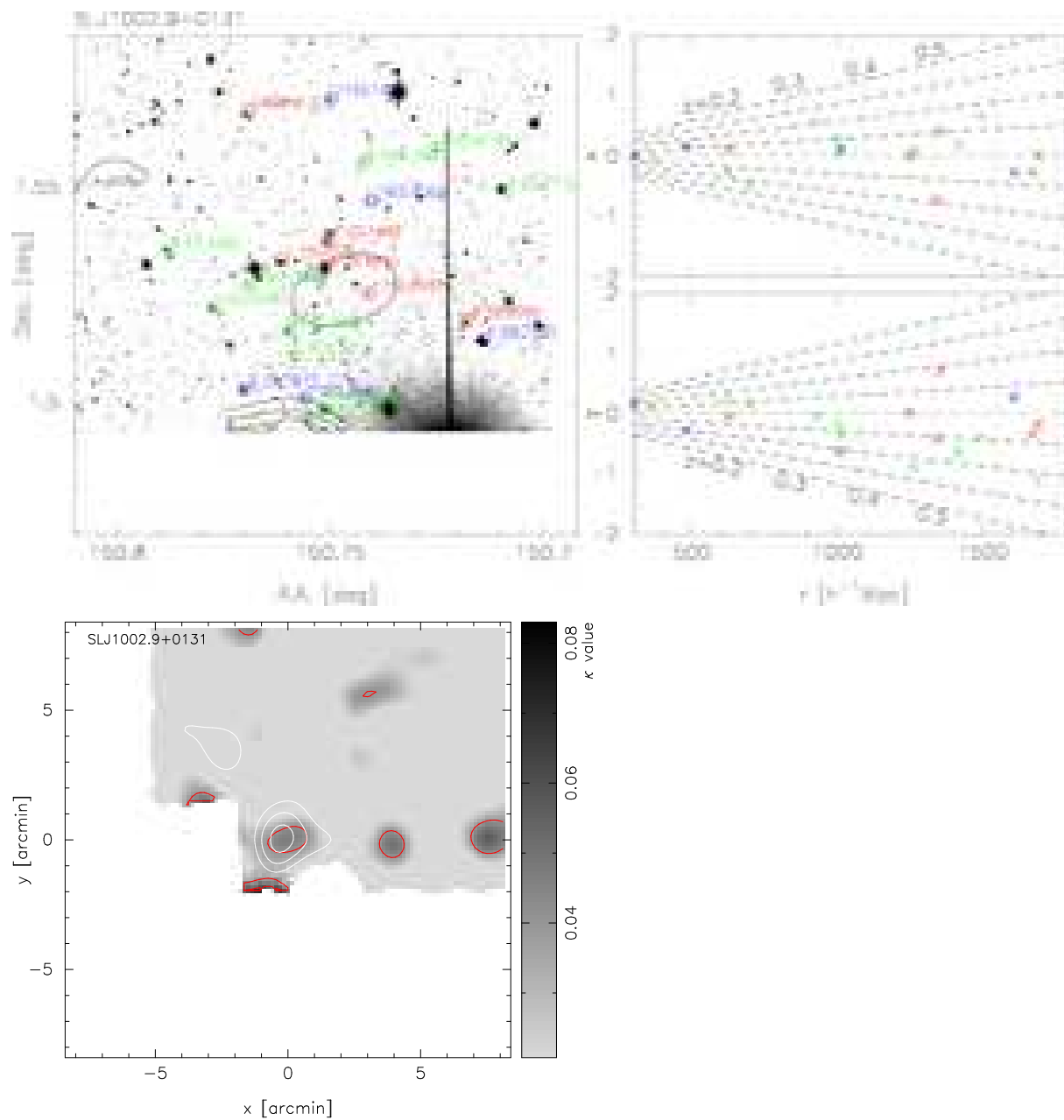


Fig. 23. Same as Figure 8 but for SL J1002.9+0131.

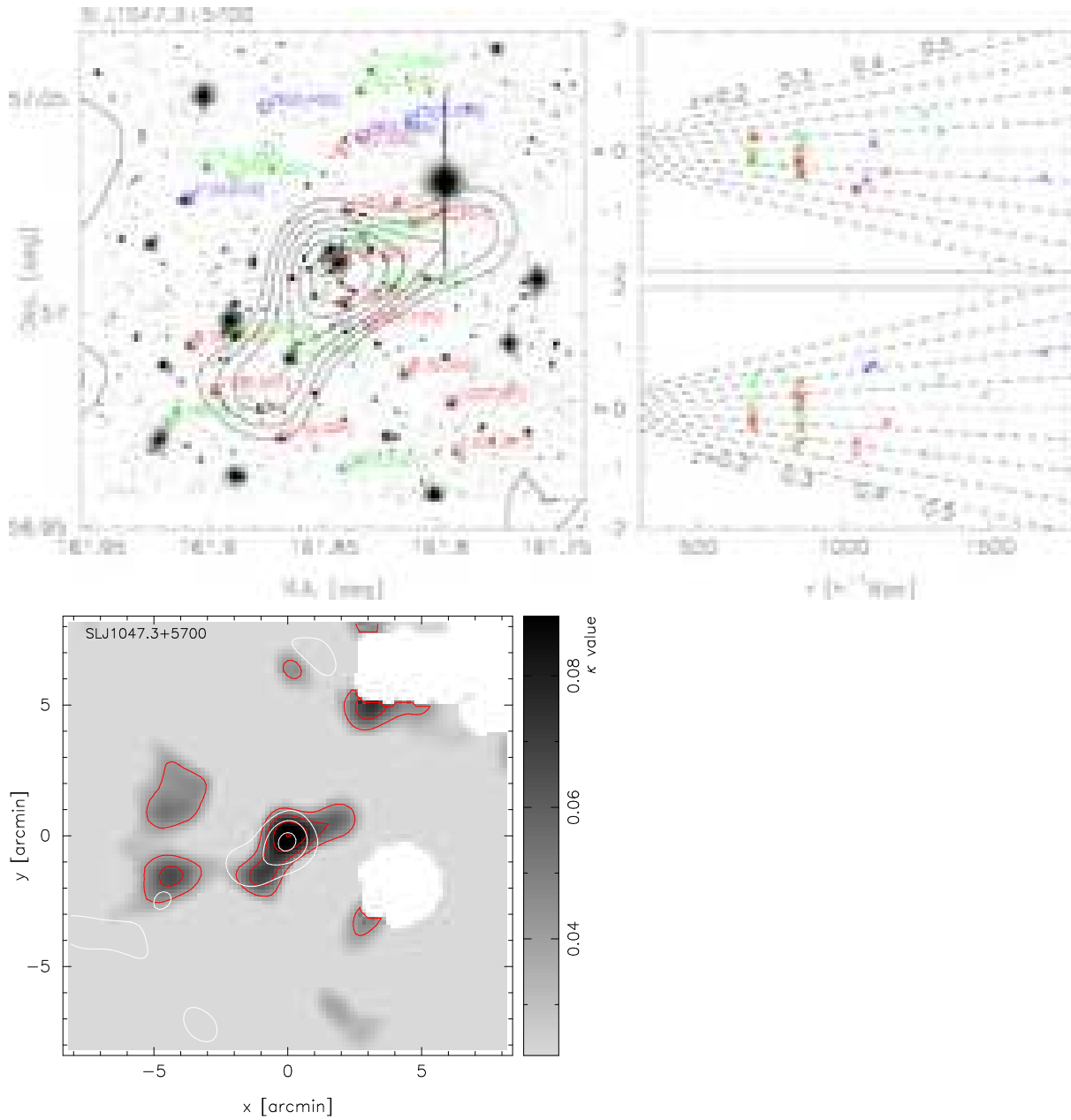


Fig. 24. Same as Figure 8 but for SL J1047.3+5700.

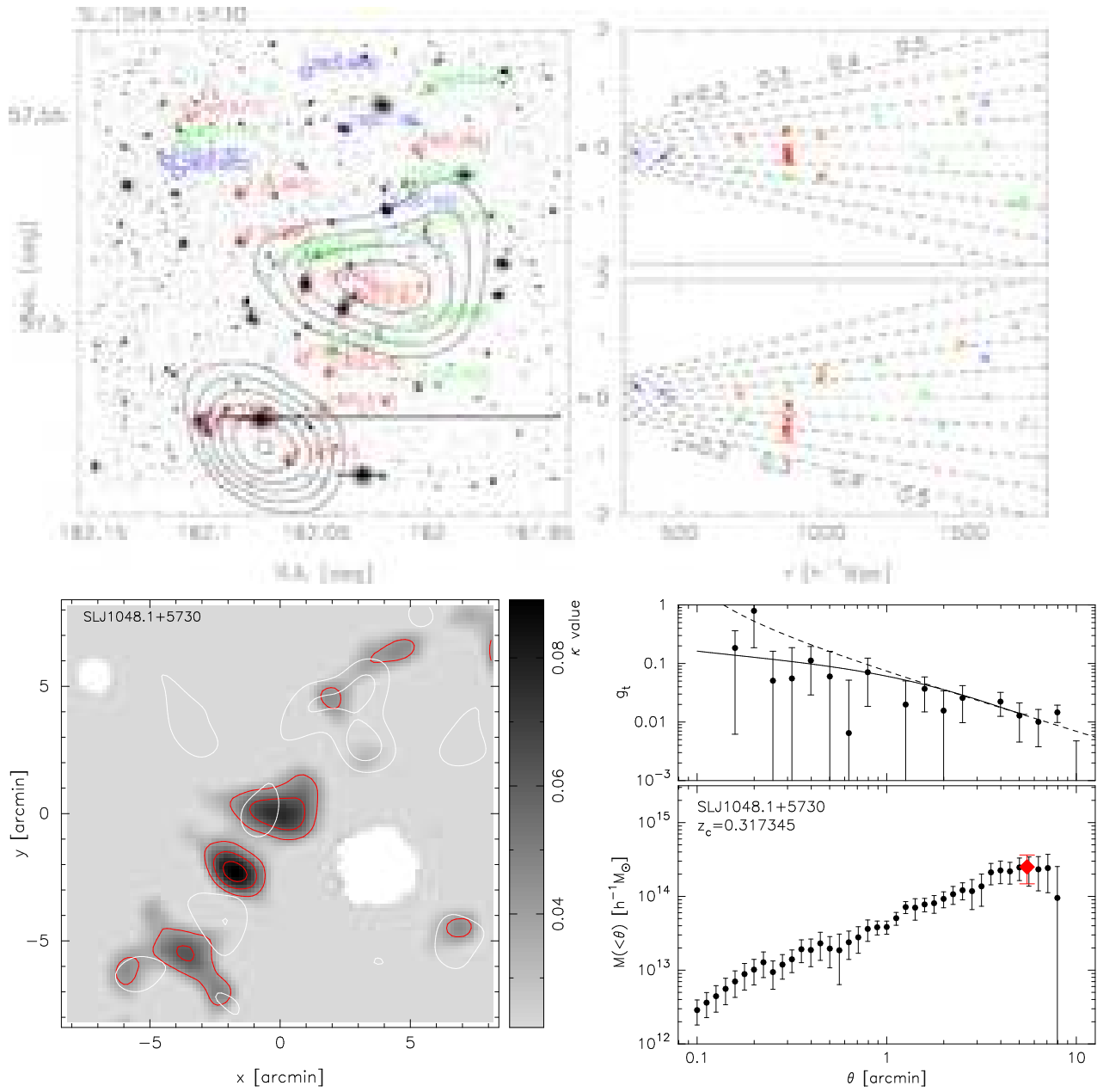


Fig. 25. Same as Figure 8 but for SL J1048.1+5730.

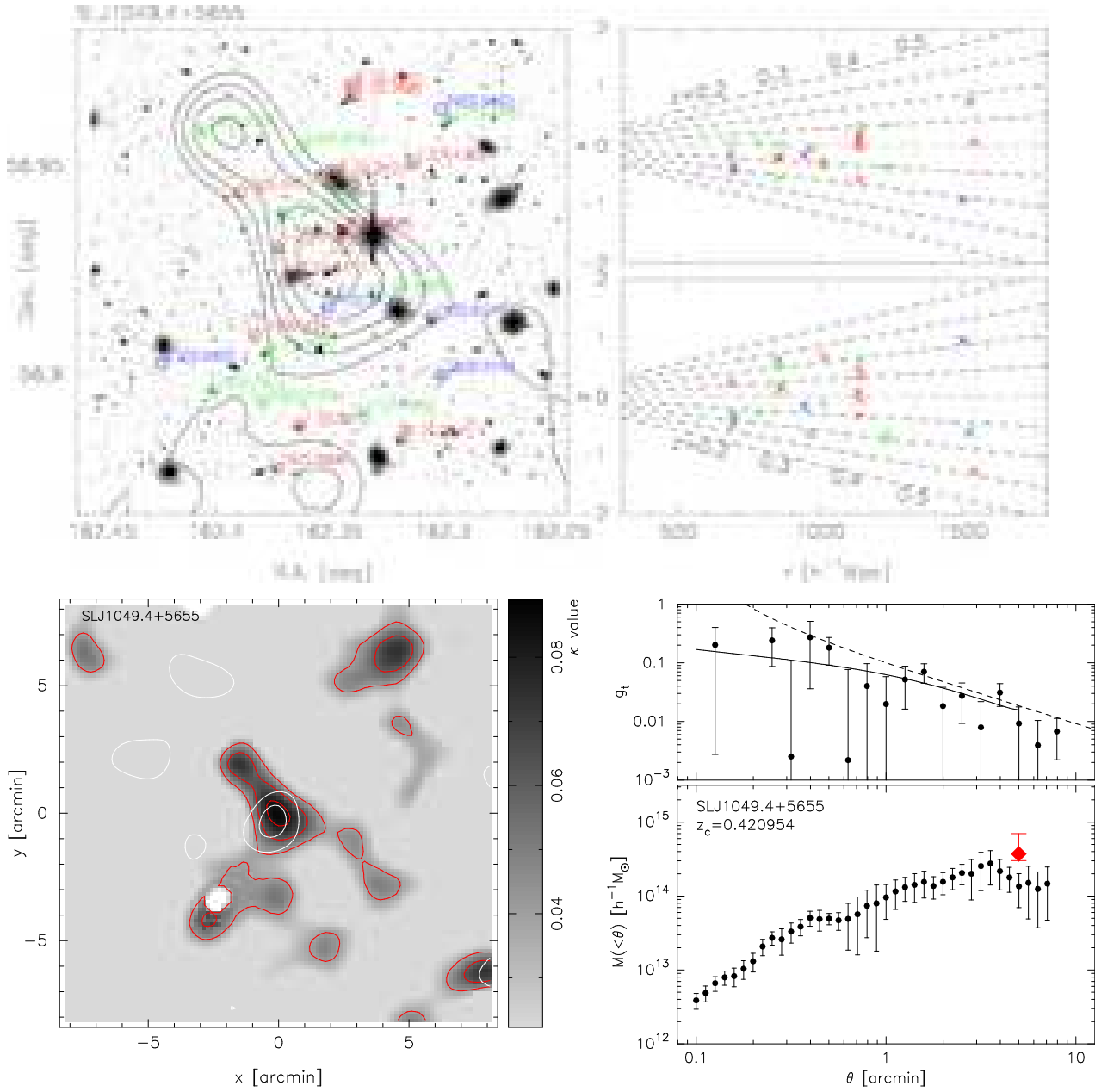


Fig. 26. Same as Figure 8 but for SL J1049.4+5655.

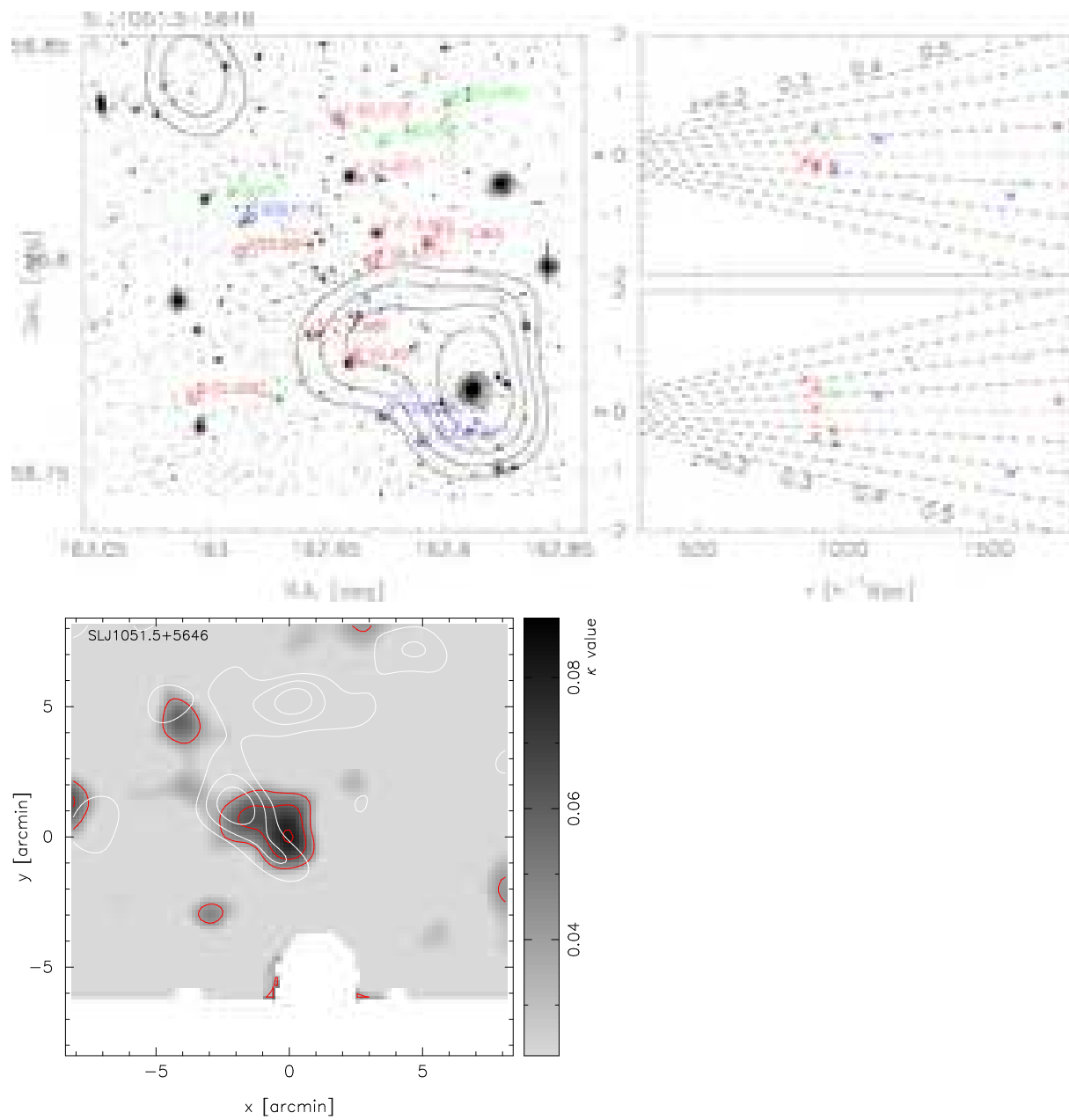


Fig. 27. Same as Figure 8 but for SL J1051.5+5646.

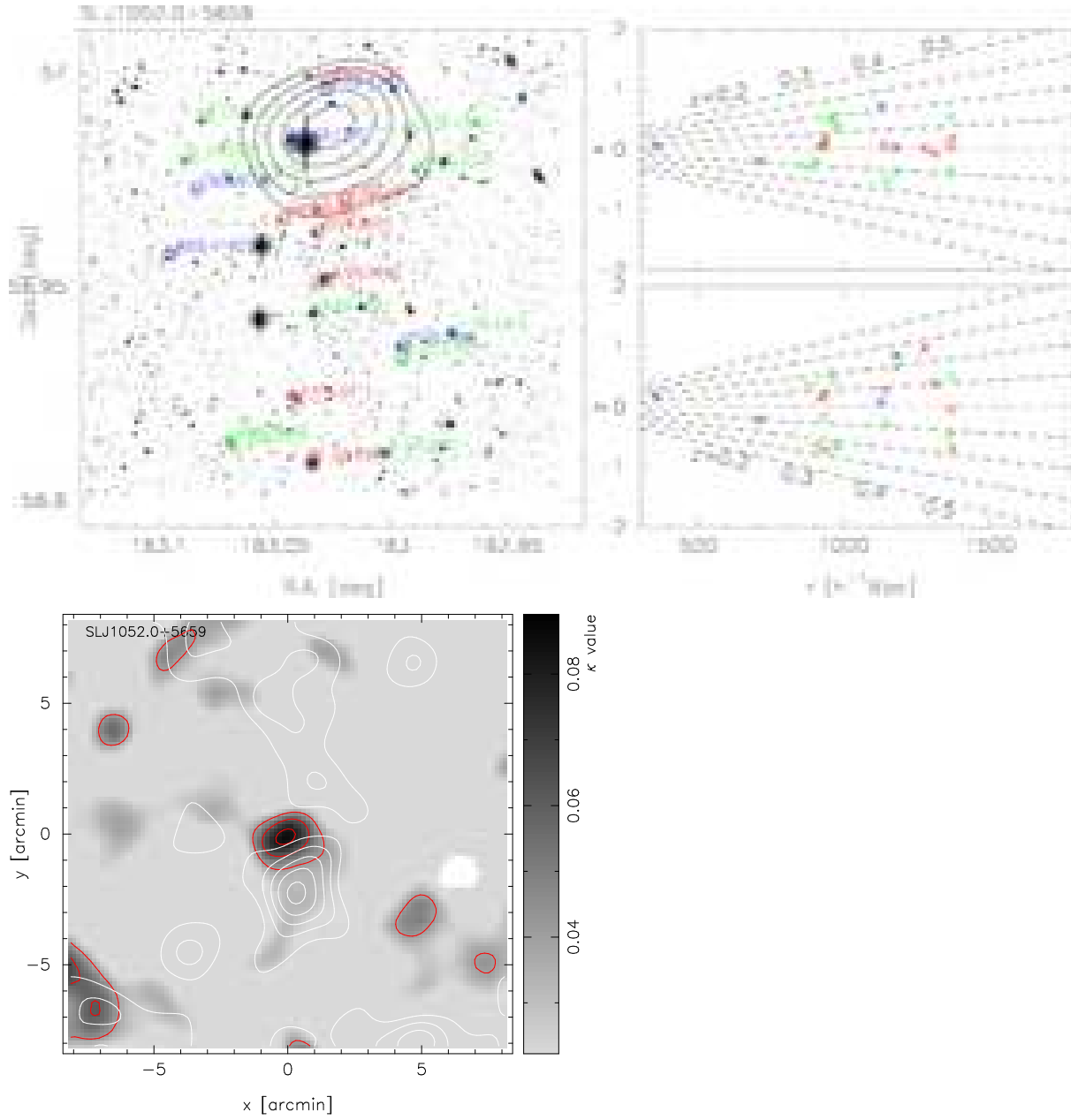


Fig. 28. Same as Figure 8 but for SL J1052.0+5659.

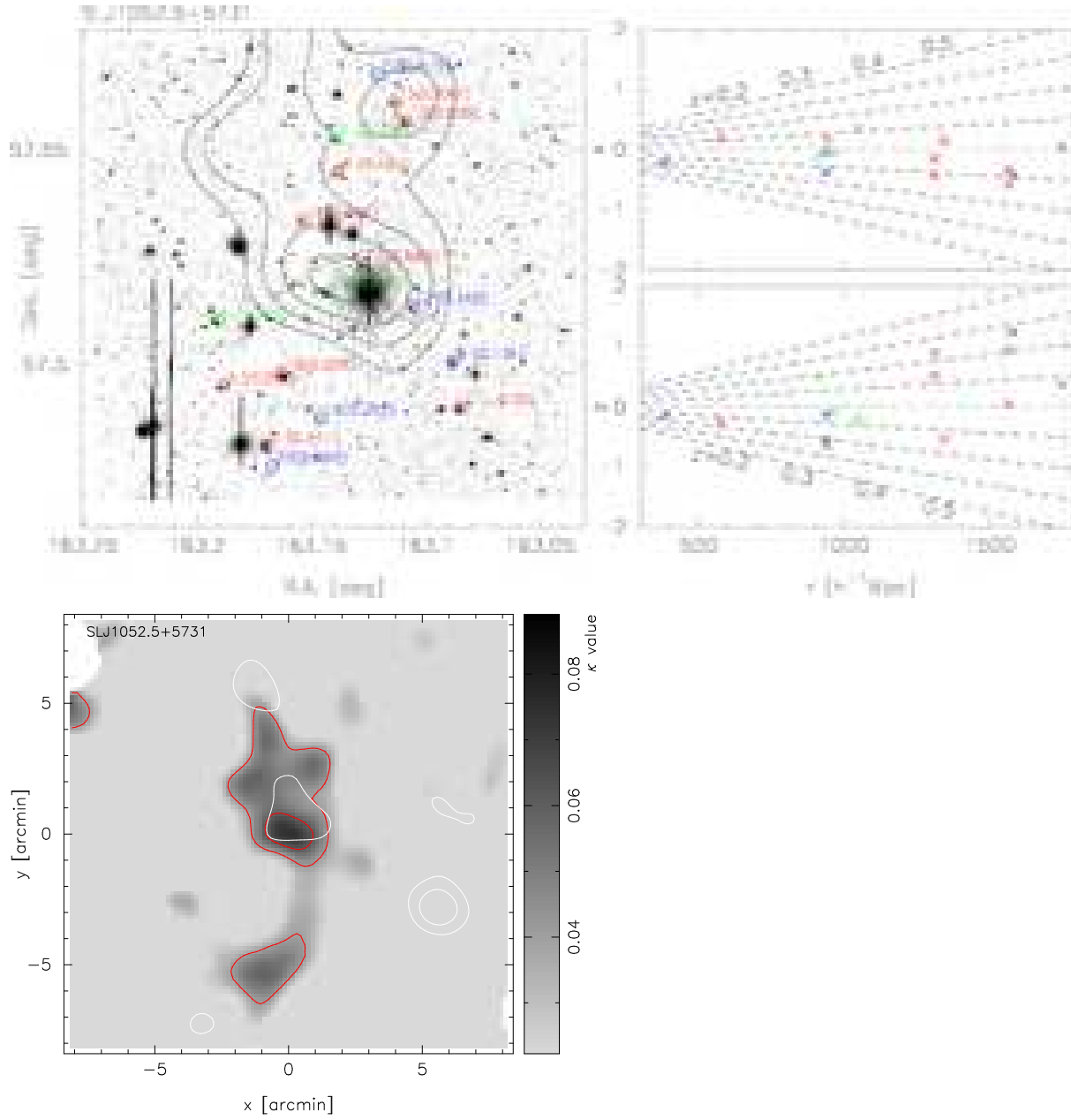


Fig. 29. Same as Figure 8 but for SL J1052.5+5731.

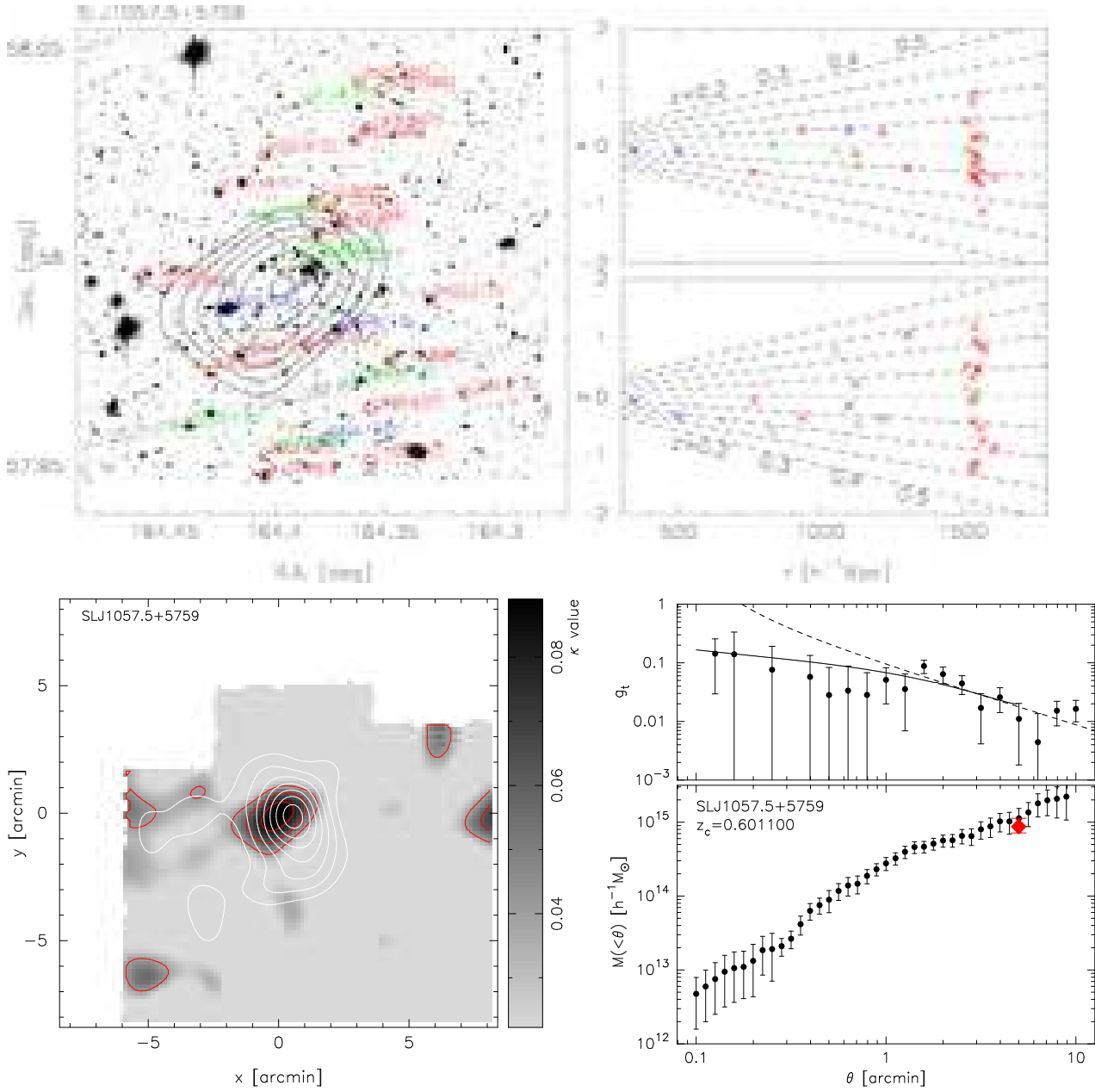


Fig. 30. Same as Figure 8 but for SL J1057.5+5759.

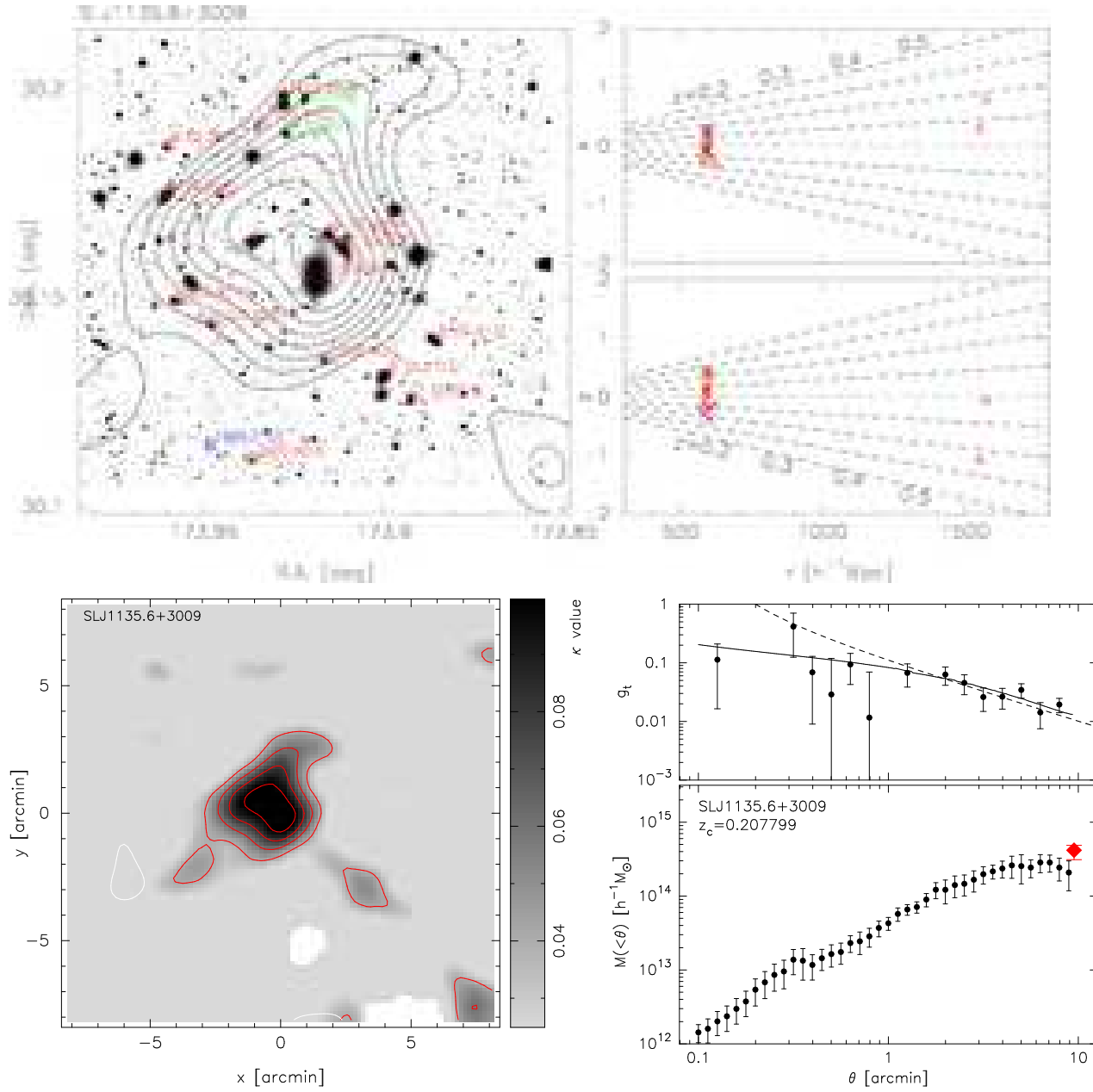


Fig. 31. Same as Figure 8 but for SL J1135.6+3009.

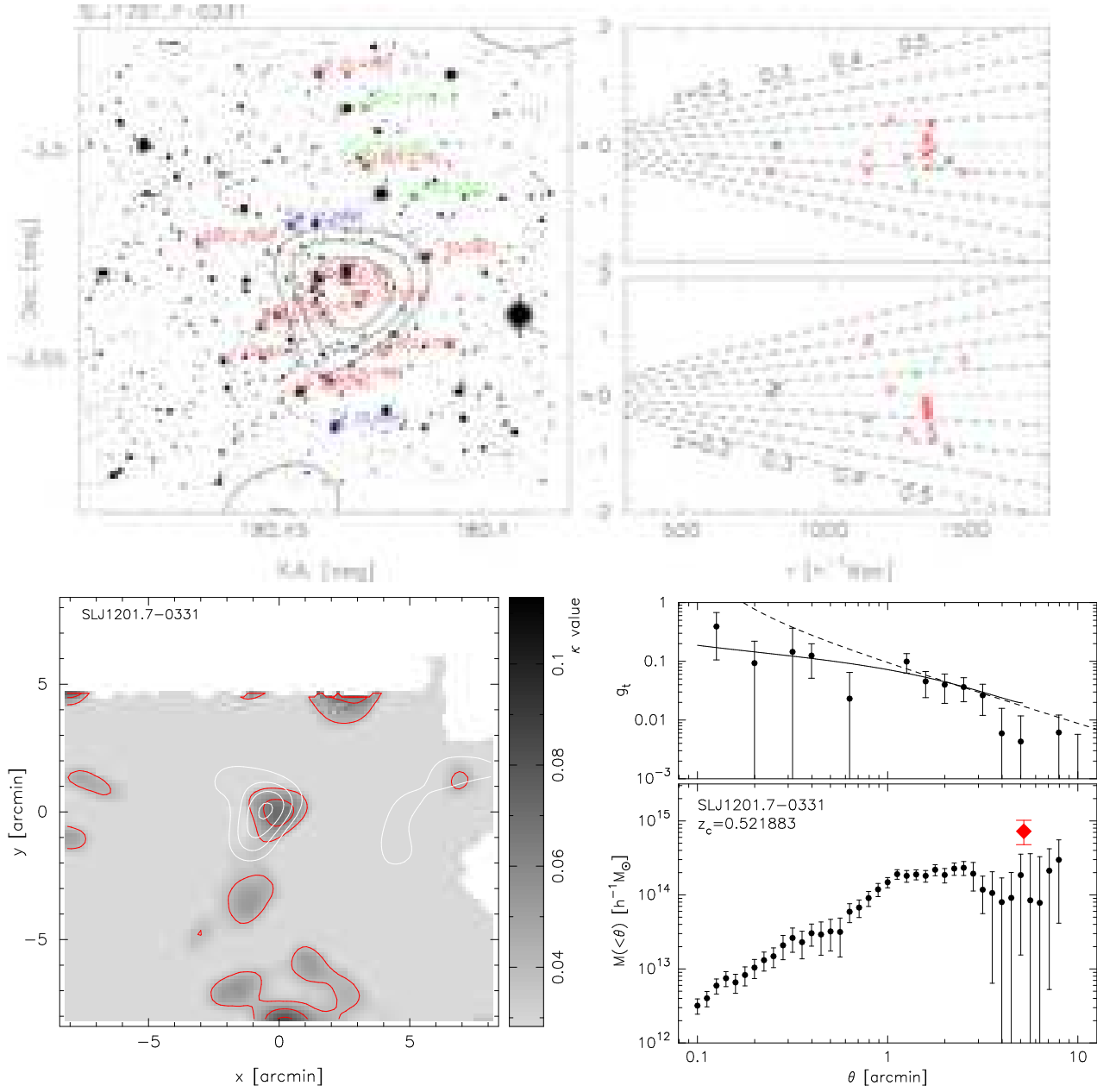


Fig. 32. Same as Figure 8 but for SL J1201.7–0331.

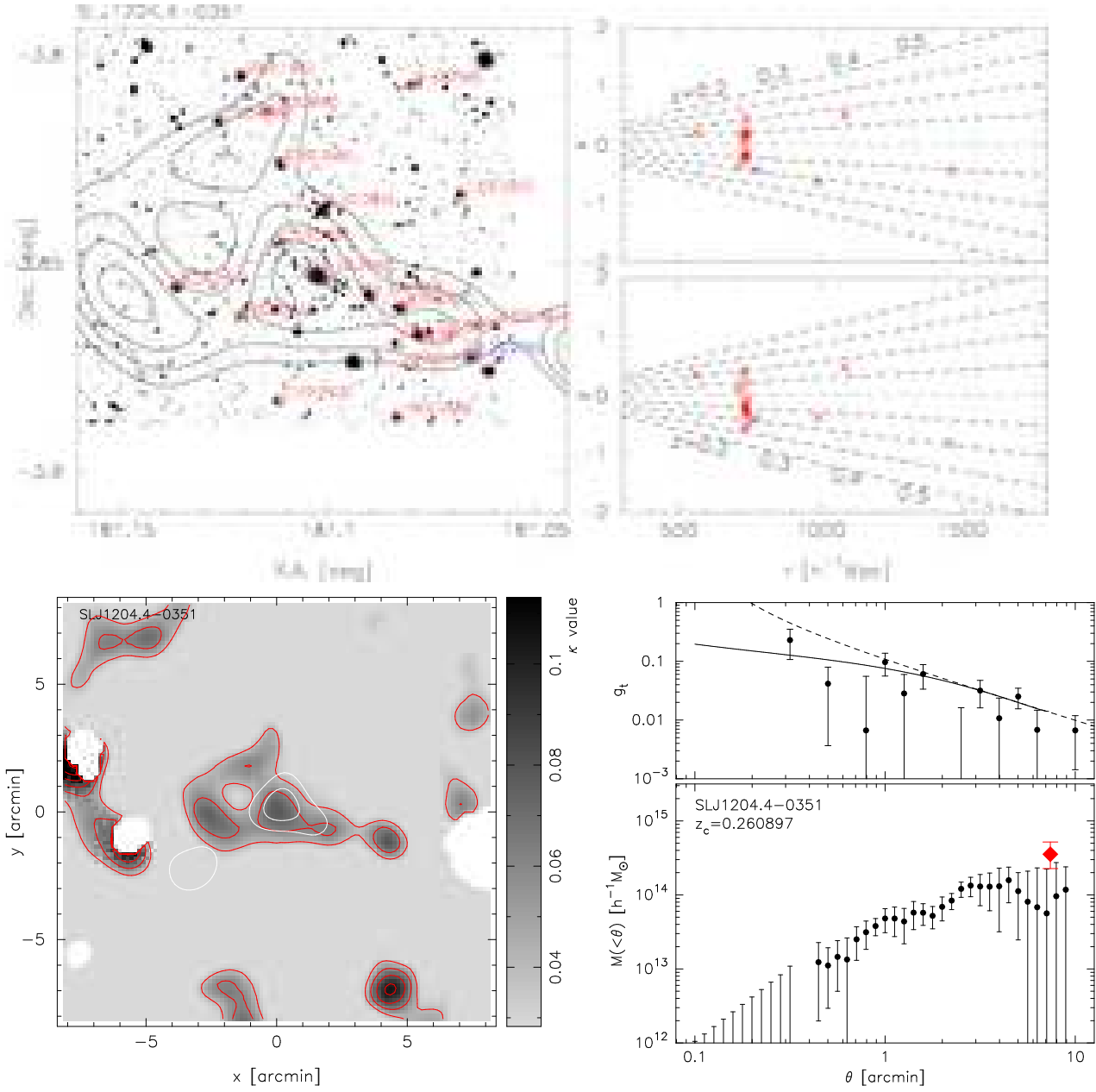


Fig. 33. Same as Figure 8 but for SL J1204.4–0351.

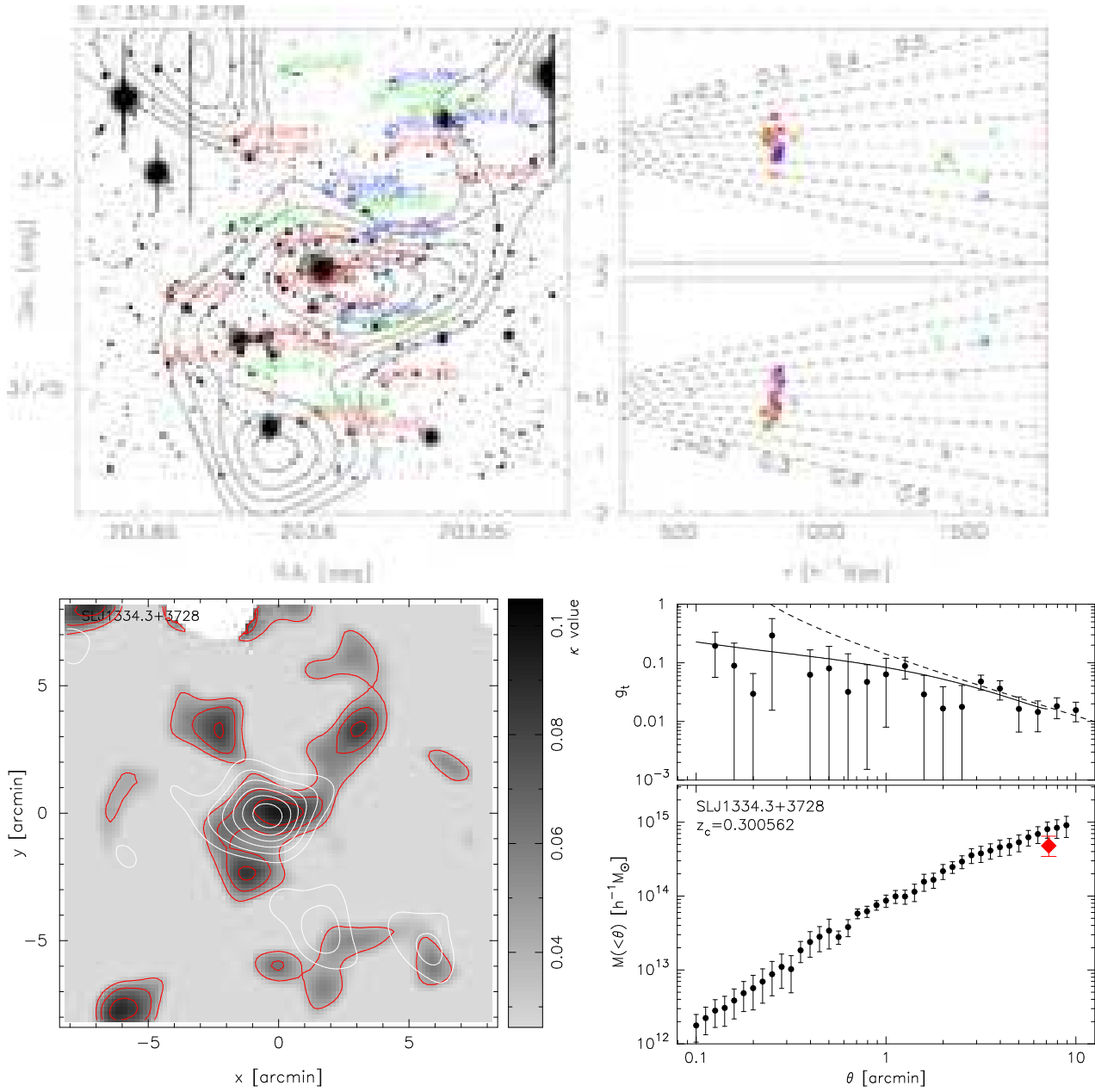


Fig. 34. Same as Figure 8 but for SL J1334.3+3728.

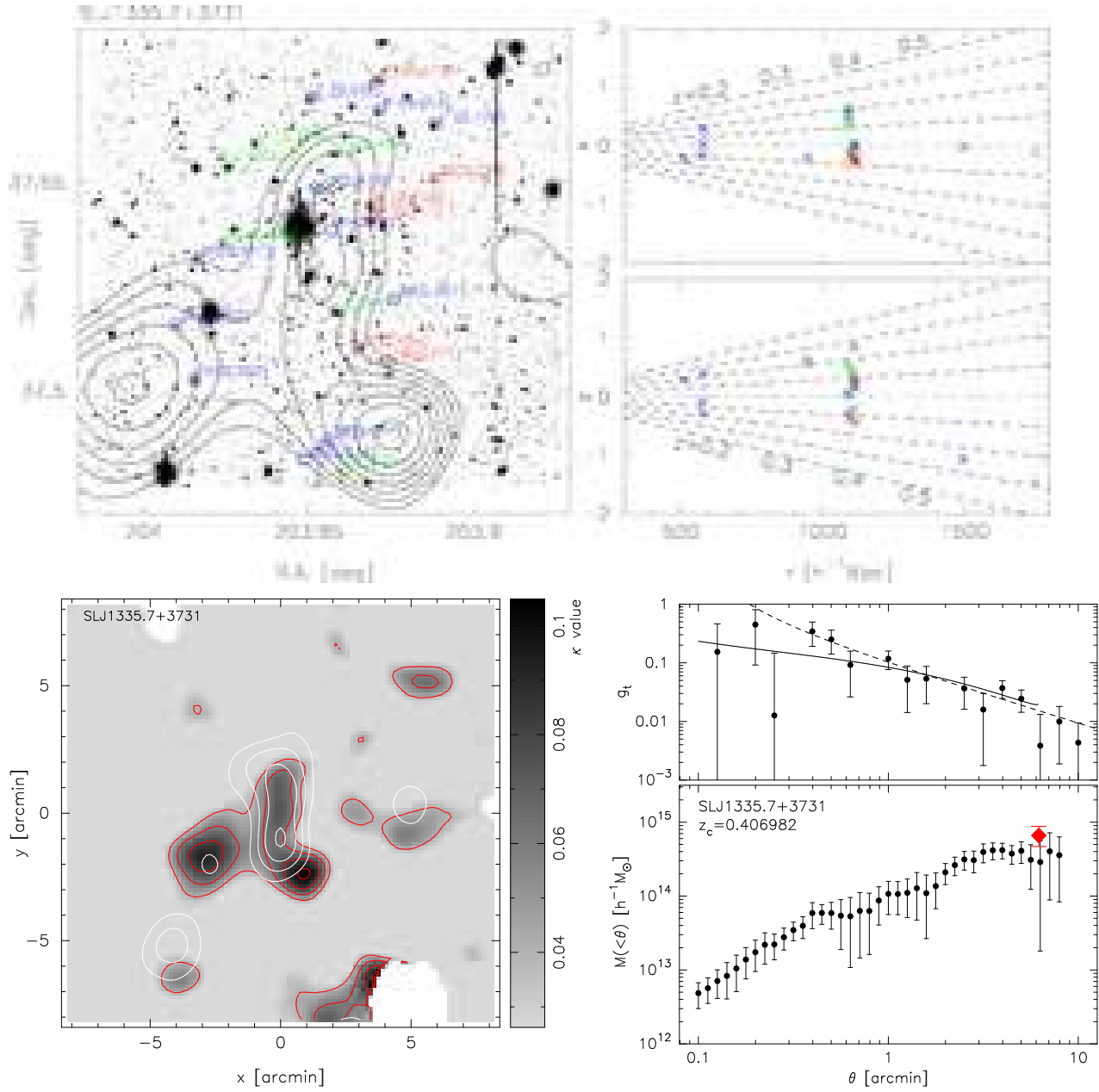


Fig. 35. Same as Figure 8 but for SL J1335.7+3731.

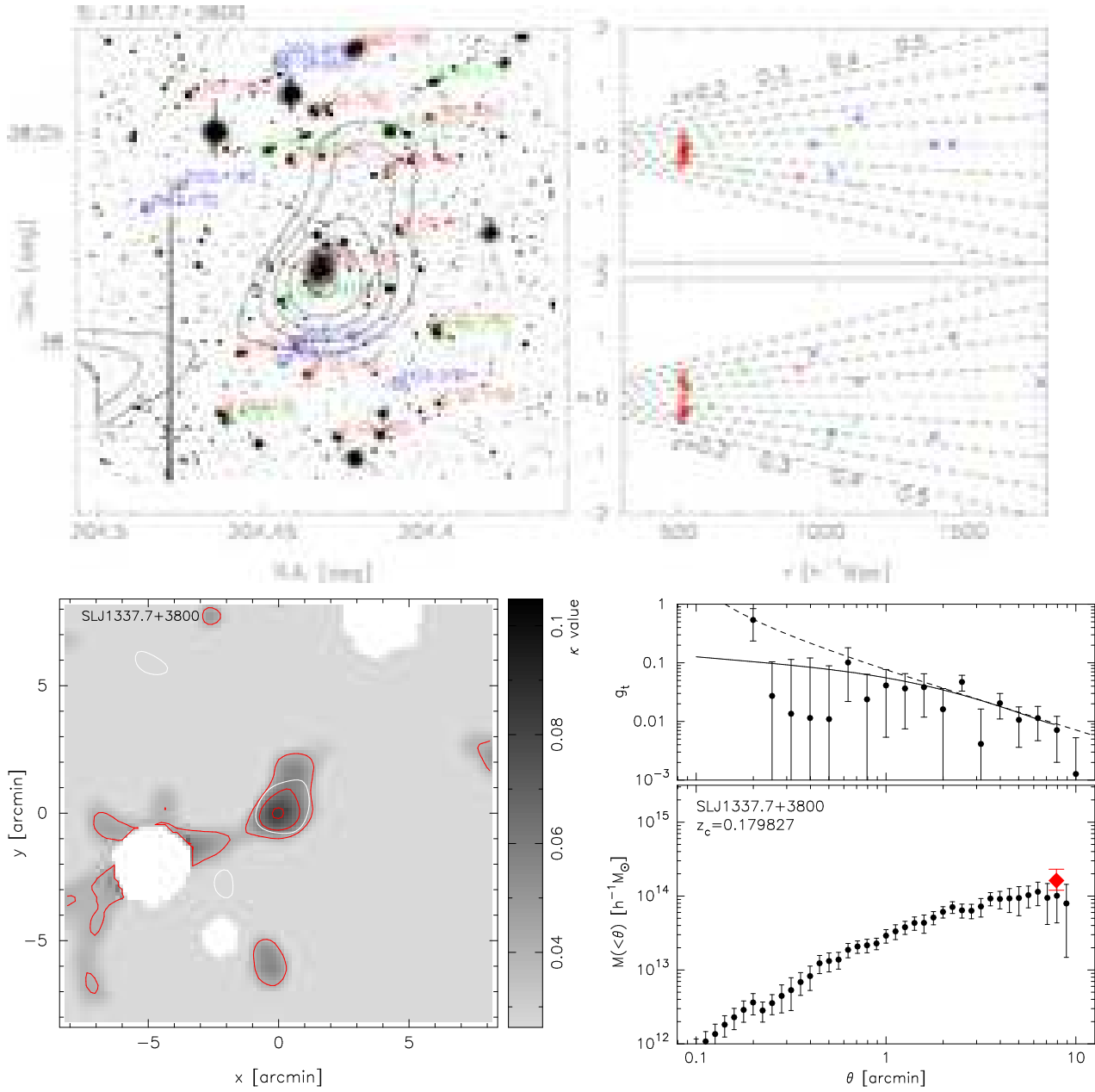


Fig. 36. Same as Figure 8 but for SL J1337.7+3800.

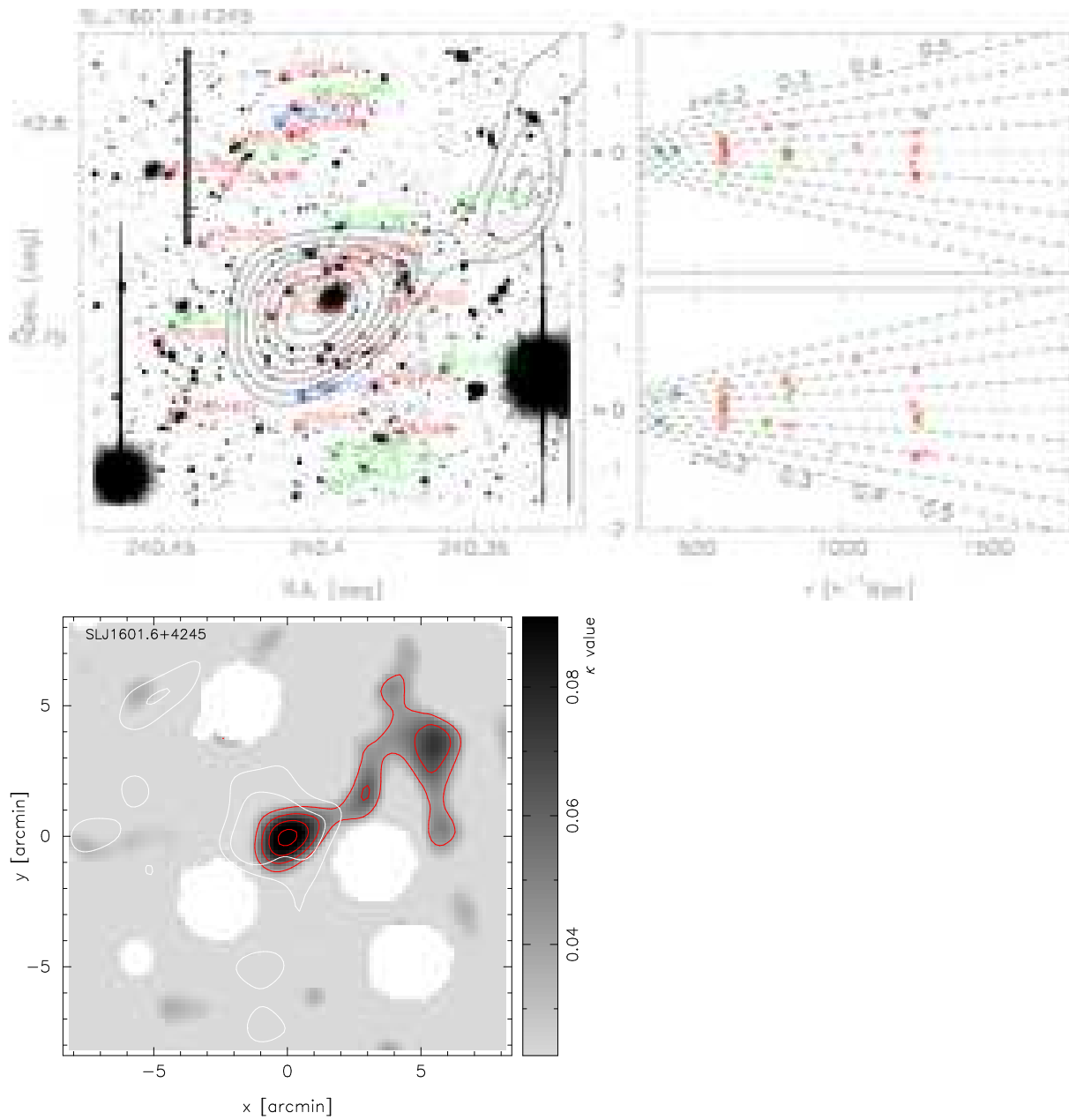


Fig. 37. Same as Figure 8 but for SL J1601.6+4245.

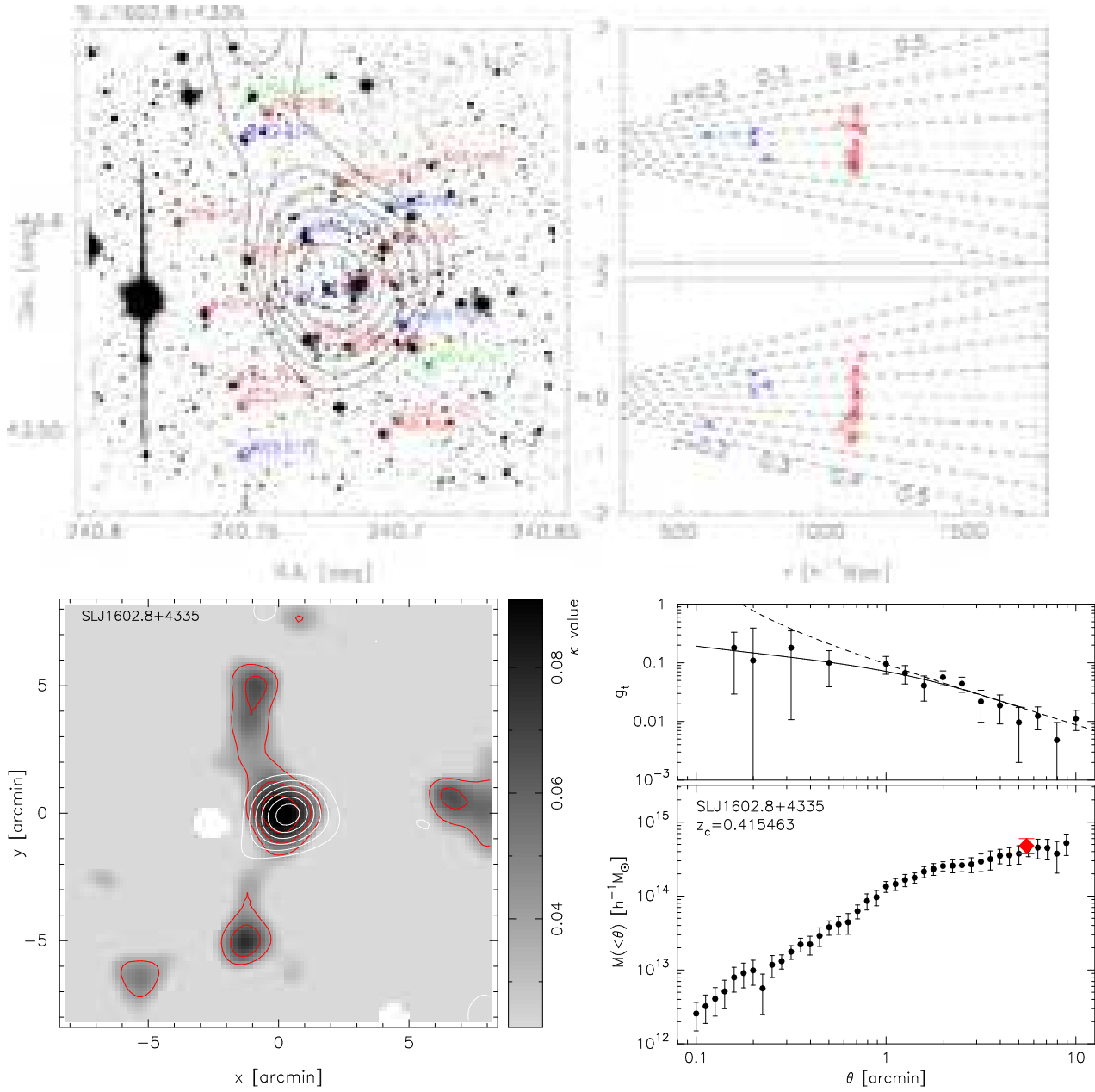


Fig. 38. Same as Figure 8 but for SL J1602.8+4335.

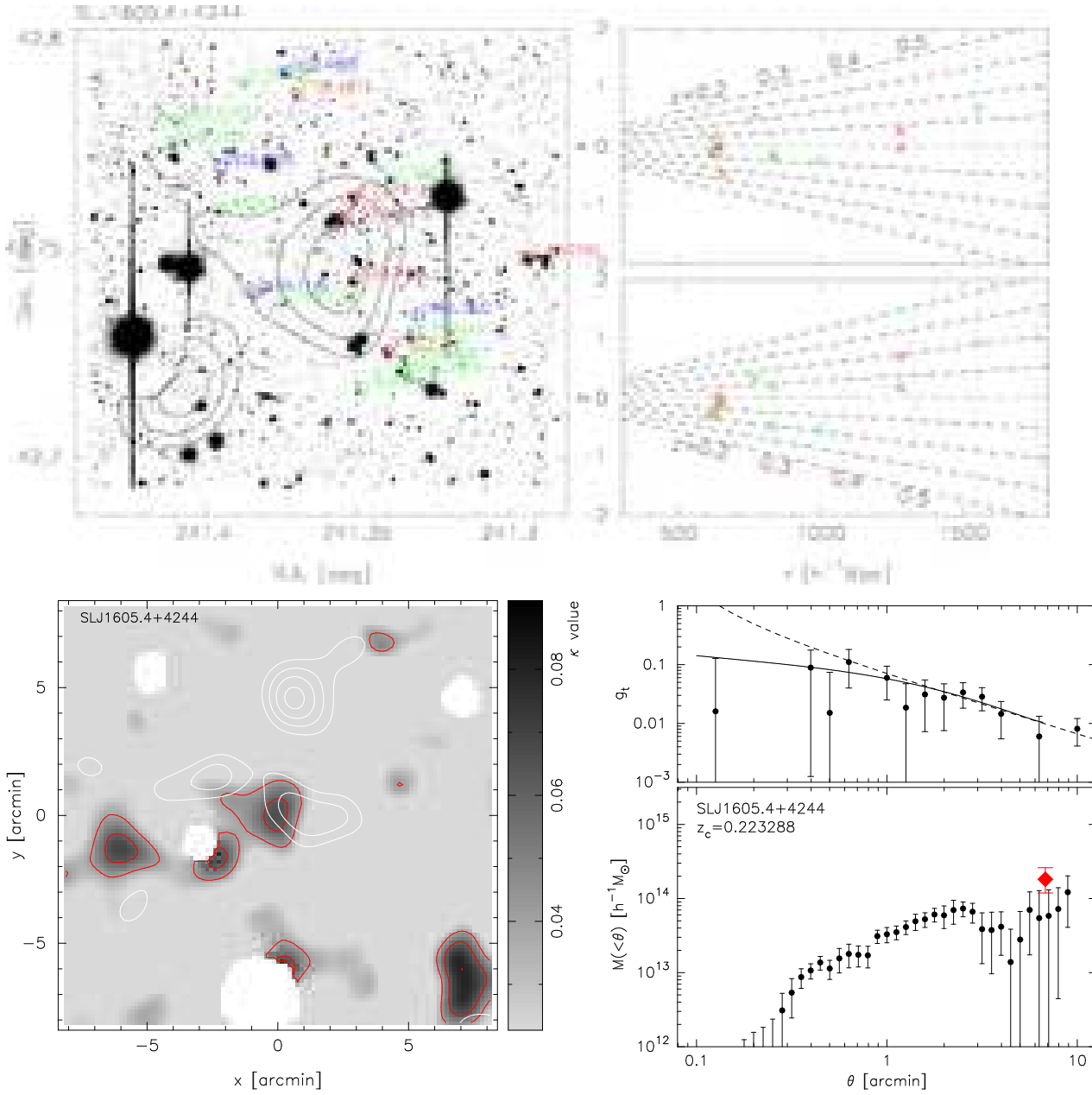


Fig. 39. Same as Figure 8 but for SL J1605.4+4244.

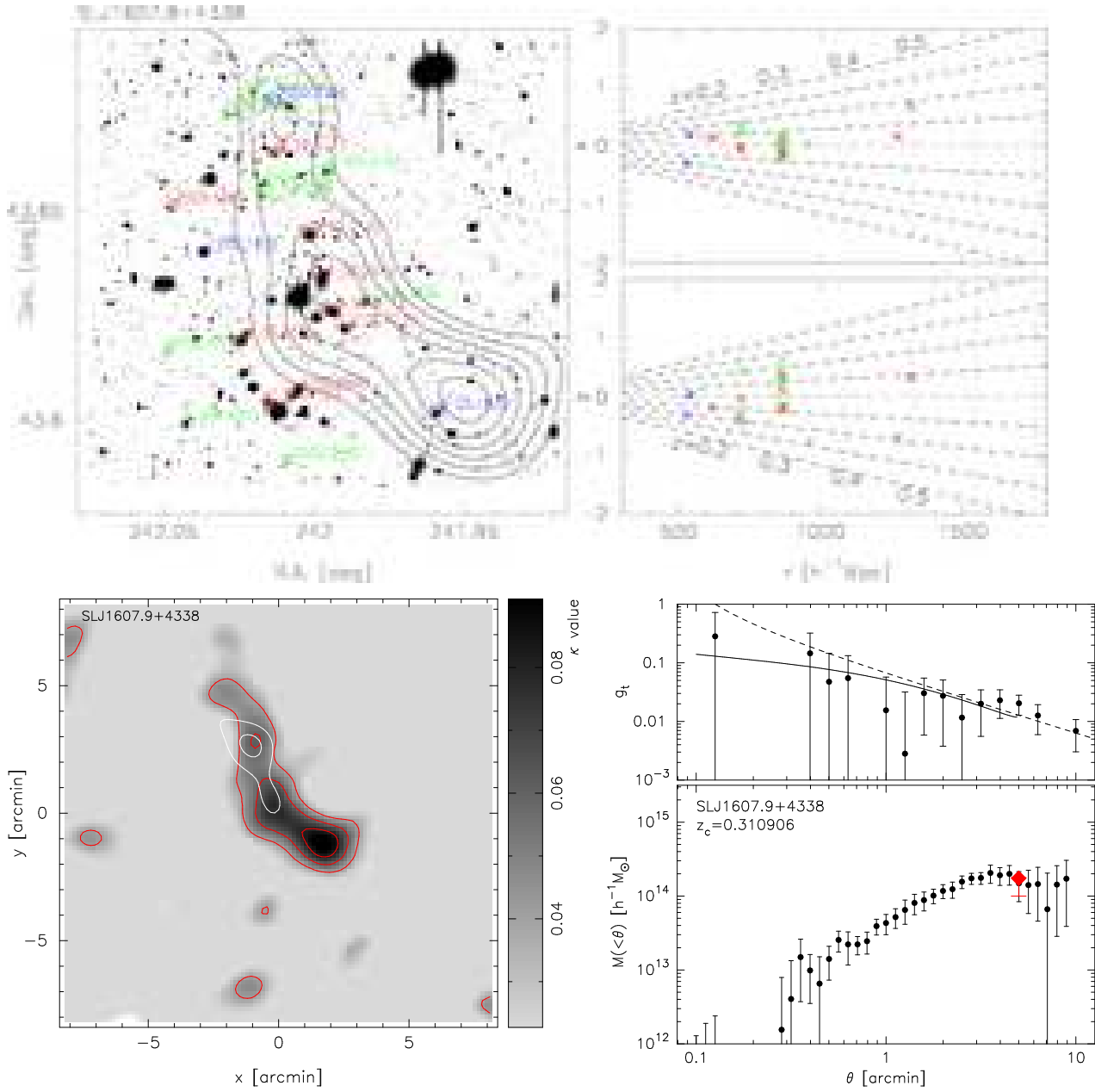


Fig. 40. Same as Figure 8 but for SL J1607.9+4338.

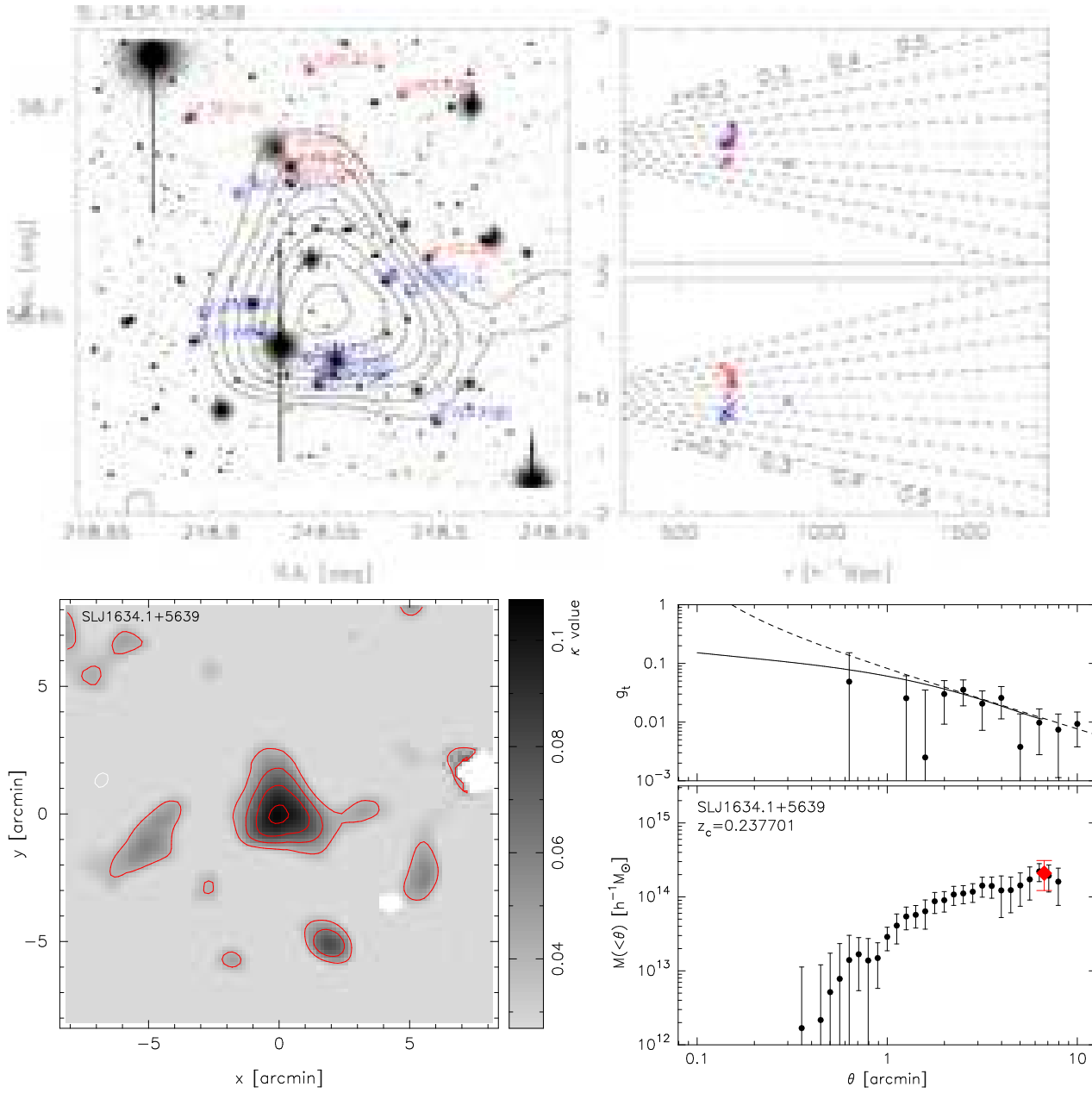


Fig. 41. Same as Figure 8 but for SL J1634.1+5639.

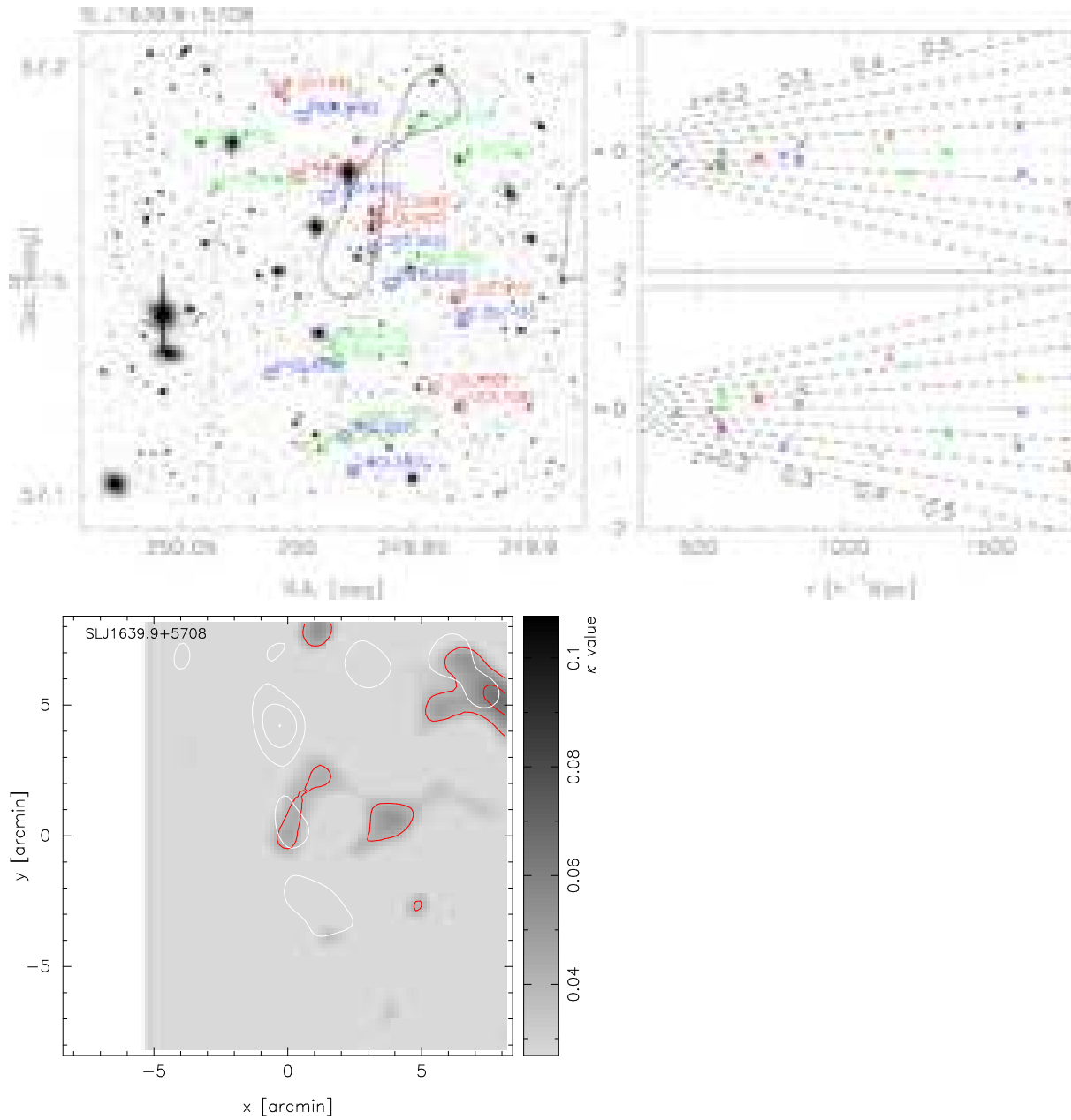


Fig. 42. Same as Figure 8 but for SL J1639.9+5708.

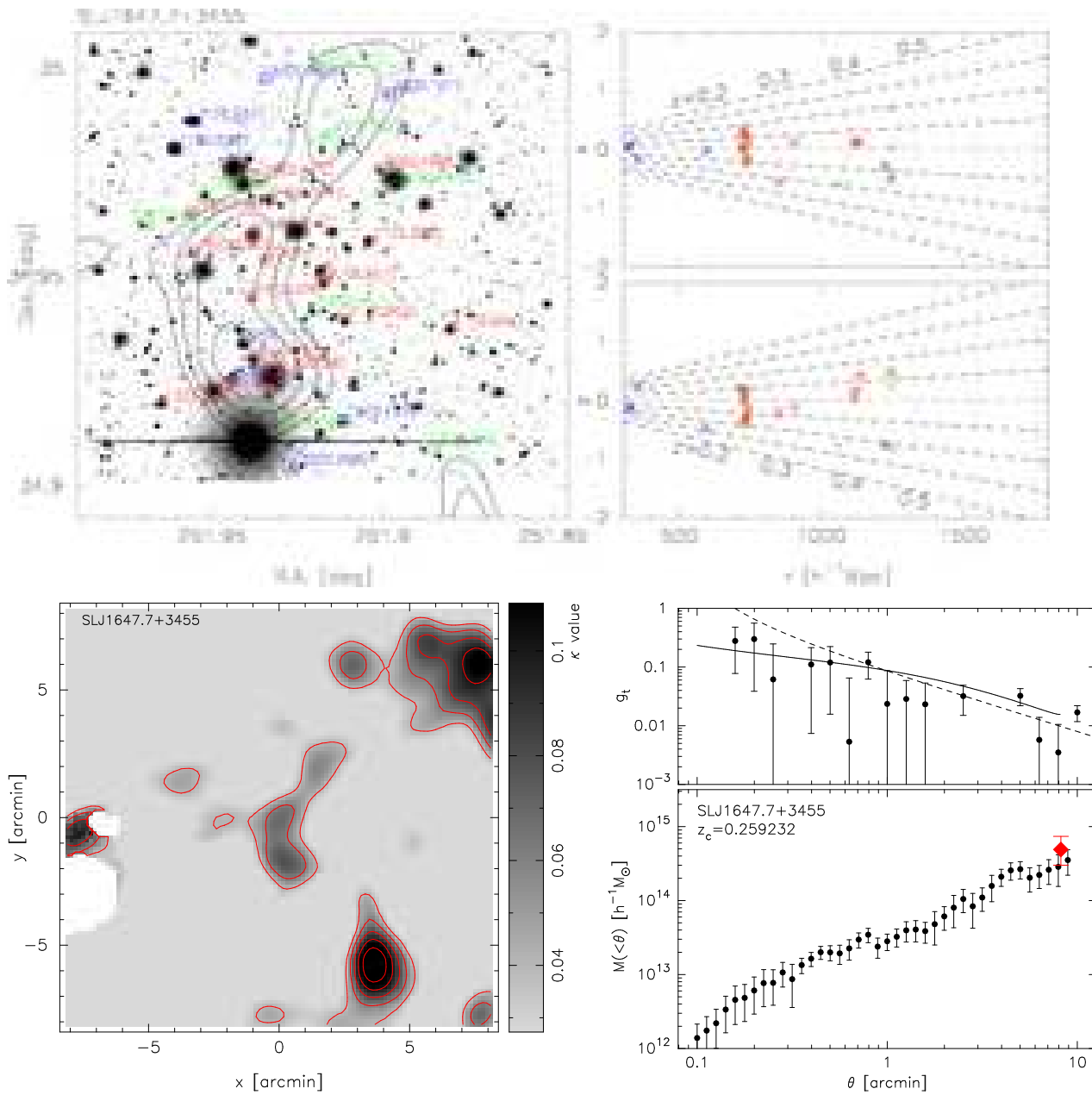


Fig. 43. Same as Figure 8 but for SL J1647.7+3455.

Appendix 3. Properties of previously studied clusters

When studying cluster scaling relations in §6, we included two cluster candidates from our weak lensing survey that had already been spectroscopically verified and whose velocity dispersions were previously known. Data from the literature were exposed to the same selection criteria used to make our clean sample (see §6.1). Observations of clusters SL J0221.7–0345 and SL J0228.4–0425 by Willis et al. (2005, where they are named XLSSC 006 and XLSSC 012) both satisfy our conditions.

These two clusters were originally identified via their X-ray emission. Later spectroscopic observations by Willis et al. (2005) revealed galaxy velocity dispersions for SL J0221.7–0345 of $\sigma_v = 821_{-74}^{+92}$ km/s (computed from 39 galaxy redshifts) and for SL J0228.4–042 of 694_{-91}^{+204} km/s (from 13 galaxy redshifts).

In P1, the two clusters are listed as XMM-LSS-00 and XMM-LSS-21. We measured the weak lensing properties of these clusters using the method described in §5, and summarize our results in Table 4. Weak lensing mass maps, galaxy density maps, tangential shear profiles and aperture mass profiles are presented in Figures 44 and 45.

Table 4. Summary of weak lensing analyses: (a) the amplitude of the tangential shear profile at 1 arcmin, when fitted with an *SIS* model (see §5.4.2). (b) the best-fit *SIS* velocity dispersion parameter. (c) the virial mass estimated by fitting the radial shear profile with an NFW model. (d) the M_{200} computed assuming the NFW profile. (e) the M_{500} computed assuming the NFW profile. (f) the virial radius computed from the NFW mass using the relation eq (13).

Name	XMM-LSS ID	z_c	$\gamma_{\text{sis}}^{(a)}$	$\sigma_{\text{SIS}}^{(b)}$ [km/s]	$M_{\text{NFW}}^{(c)}$	$M_{200}^{(d)}$	$M_{500}^{(e)}$	$r_{\text{vir}}^{(f)}$
						$[\times 10^{14} h^{-1} M_{\odot}]$		[comoving Mpc h^{-1}]
SL J0221.7–0345	XLSSC 006	0.429	0.079	926^{+406}_{-438}	$5.01^{+1.37}_{-1.39}$	$4.35^{+1.19}_{-1.21}$	$2.97^{+0.81}_{-0.82}$	1.7
SL J0228.4–0425	XLSSC 012	0.433	0.065	839^{+449}_{-448}	$3.24^{+1.46}_{-1.19}$	$2.82^{+1.27}_{-1.04}$	$1.95^{+0.88}_{-0.72}$	1.6

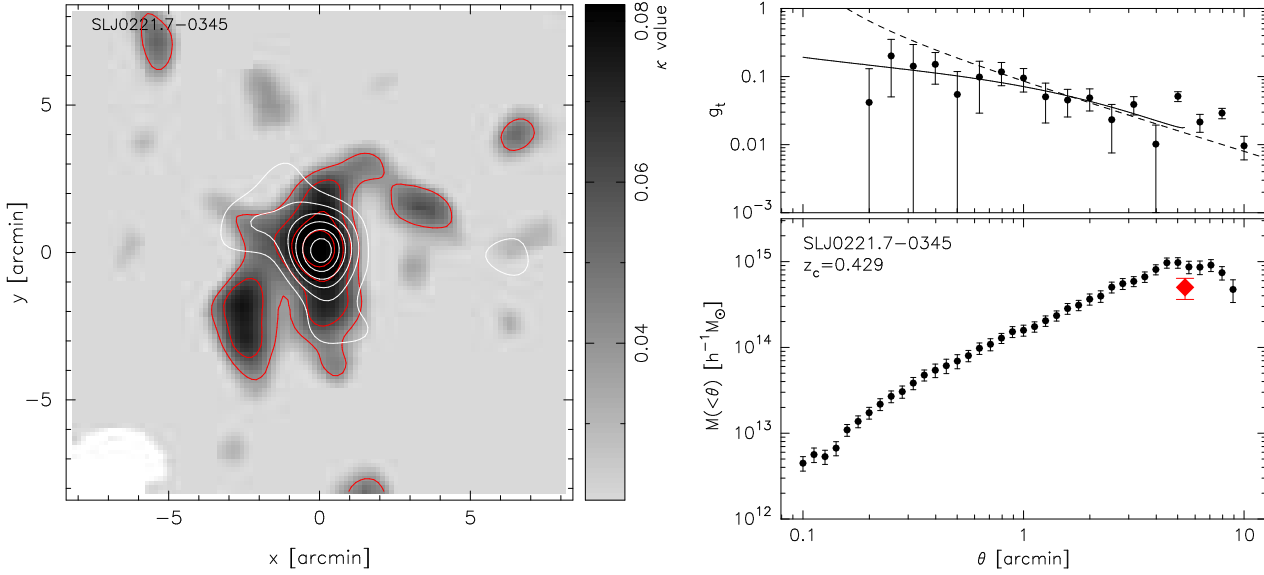


Fig. 44. Same as the bottom two panels of Figure 8 but for SL J0221.7–0345.

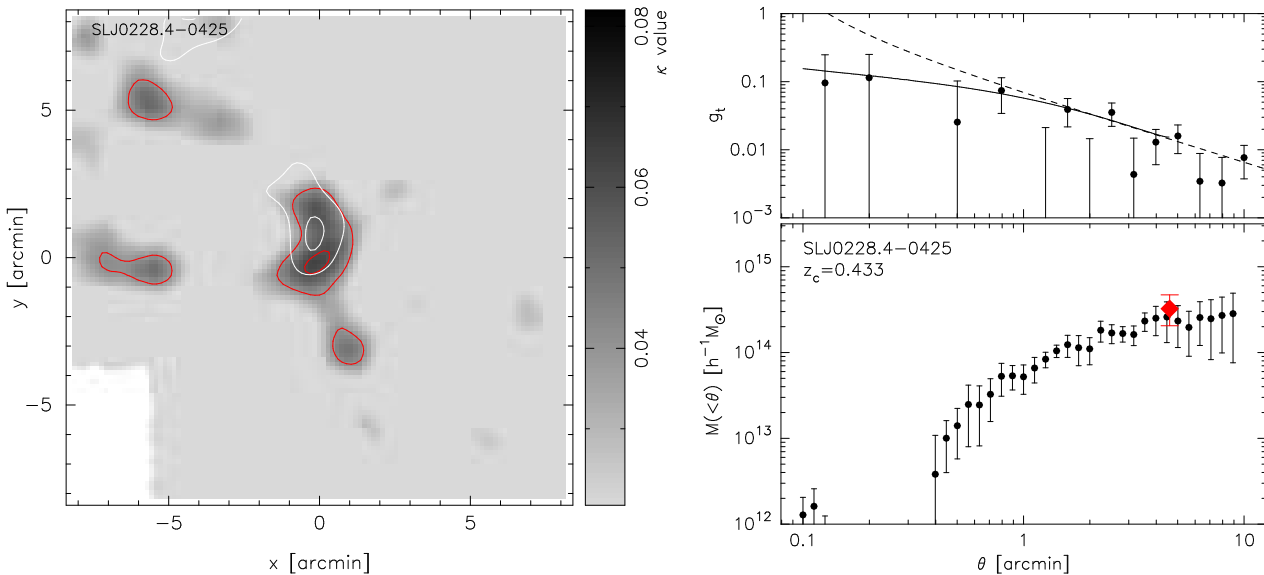


Fig. 45. Same as the bottom two panels of Figure 8 but for SL J0228.4–0425.